



Università di Pisa

Facoltà di Ingegneria

Corso di Laurea Specialistica in Ingegneria Biomedica

Tecniche Elettrotomografiche per la Caratterizzazione di Tessuti Biologici

Il candidato:

Caltagirone Laura

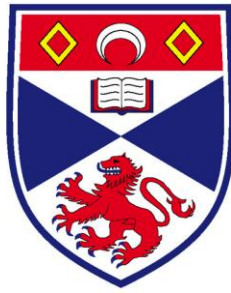
Primo relatore:

Menciassi Arianna

Secondo relatore:

Giardini Mario E.

Anno Accademico 2010-2011



University of St Andrews, Scotland.

This work has been carried out in collaboration with the School of Medicine of the University of St Andrews, Scotland, UK.

Supervisor:
Giardini Mario E.

Academic Year 2010-2011

*The warrior of the light believes. Just like children believe.
Because he believes in miracles, miracles begin to happen.
Because he is sure that his thought can change his life,
his life begins to change.
Because he is sure that he will find love, this love appears.
From time to time he is disappointed. Sometimes he gets hurt.
And then he hears comments like: "that fellow's so naive!"
But the warrior knows that it is all worthwhile.
For each defeat he counts two victories in his favor.
All those who believe know this.*

Acknowledgements

First and foremost I would like sincerely thank my advisor Mario Ettore Giardini for tactfully providing direction throughout my Thesis, for giving unique solutions in the laboratory, for helping hand throughout the entire project, for believing in my work and for giving an introduction to the world of research.

I would like also to express my gratitude to St. Andrews University in Scotland, and in particular the School of Medicine, for providing financial support and facilities. There I could find a very appropriate place to study. Thanks to Arianna Menciassi for directing me to the right people for preparing the Thesis. Then great tanks go to the Biophotonics team, for your humor and smiles.

I wish to thank my parents for bringing me up in an environment that appreciated studies and research.

A special thanks is due to my friend Nicola Melville, who has celebrated with me my joy in success of these wonderful experience, and Franceschini Ferruccio for helping me in the translation of this Thesis and for you friendship.

Finally, enormous thanks to Marcoandrea for his support throughout my Master's study. Everything is easier and delightful with you. My life is completely changed with you and you are the reason for where and who I am.

Abstract

Electrical impedance tomography (EIT) is an imaging modality wherein the spatial map of conductivity and permittivity inside a medium is obtained from a set of surface electrical measurements. Electrodes are brought into contact with the surface of the object being imaged and a set of currents are applied and the corresponding voltages are measured. These voltages and currents are then used to estimate the electrical properties of the object using an image reconstruction algorithm which relies on an accurate model of the electrical interaction. The process of property estimation, called inverse problem, is highly nonlinear, ill-conditioned, and ill-posed. Reconstruction of the electrical properties distribution is an under-determined problem requiring a regularization method.

EIT has been researched extensively in the medical field, as well as in other technological areas, such as industrial process control, chemical engineering and geotechnical research. The technique has become an independent, fully-featured stream in the biomedical engineering field, and has high clinical potential as an investigation tool. The objective of this Thesis was to develop a device for EIT imaging, which could be convenient, noninvasive, easily programmable, portable and relatively inexpensive.

In this direction a simple EIT system and its hardware and software parts have been developed. Two 16-electrodes probes in circular and planar geometry were built for treating two and three-dimensional samples. Probes and a circuit board, comprehending a serial programmable interface and a switch based multiplexer, have been built and connected to a Lock-in amplifier, used as excitation source and acquisition system. As the object of EIT is a human body part, the current must be limited within the range regulated by Medical Electrical Safety Regulations in order to ensure safety the system was therefore designed to apply low AC currents (12 to 22 μA) to the samples. Matlab code for electrode switching, acquisition and reconstruction were developed. The effects of noise and of systematic error coming from the channels crosstalk was analysed.

Preliminary studies on a model system consisting of a saline solution have been performed in order to estimate the electric behavior of a physiological sample, for system calibration and in order to evaluate the performance of the acquisition system.

The data processing was accomplished by utilizing the EIDORS toolkit, an open-source toolkit developed for the solution of EIT inverse-problem reconstruction. The procedure for obtaining

the reconstructed electrical properties distribution as an image of the domain under study, relies on a finite element model for and a regularized inverse solver to obtain a unique and stable inverse solution. Both 2D and 3D specializations of EIDORS to our image reconstruction from EIT data have been realized.

A series of simulations has been conducted to evaluate the performance of the chosen algorithm when using our electrode configurations, taking into consideration of simulated voltages, contrast, spatial resolution, position dependency, and the presence of artifacts.

Subsequently, experiments with the EIT system on a 2D isotropic case of a saline solution, both alone and associated with various conductive and insulating objects, on a 3D anisotropic case of a tissue section, and an on in vivo experiment on human skin have been conducted.

Sources of difficulties in EIT image reconstruction, mainly due to the fact that the ill-posedness of the EIT reconstruction problem renders the solution sensitive to measurement errors and noise, have been explored.

Experiments have indicated that the EIT system can reconstruct resistive and capacitive images of good contrast, with adequate robustness towards experimental fluctuations.

Contents

Abstract	5
Contents	7
1. Introduction to EIT	
1.1. Background	9
1.2. Electrical Impedance Tomography as an Imaging Modality	12
1.2.1. Clinical Applications	15
1.3. EIT Theory	17
1.3.1 Different Modalities for Electric Measurement of Impedance in EIT	23
1.4. The Inverse Problem	26
1.5. Algorithms for Ill-posed Problem	30
1.5.1 Mathematical Model of the Physical System	31
1.5.2 Discretization and Finite Element Formulation	36
1.5.3 Forward Computation	41
1.5.4 Calculation of the Jacobian Matrix	43
1.5.5 Inverse Regularized Solution	46
2. The EIT System	
2.1. EIT system: Block Diagram	49
2.2. Hardware	52
2.2.1. Parasitic effects	60
2.2.2. Acquisition Strategy	69
2.3. Software	74
2.4. PCB Calibration	78
2.5. Forward Problem Simulation	80
2.6. Homogeneous Image Reconstruction: Saline Solution	83
3. Inhomogeneous Reconstructions of Various Objects	
3.1. Image of Conductive and Insulating Objects	86
3.2 Results	101
4. Biological Sample Imaging	
4.1. The Complex Admittivity Case	103
4.2. Biological Sample: Tissue Section	105
4.3. Human Sample: Skin	114
4.3.1 3D Imaging with Planar Electrode Array: Numerical Simulation	115
4.3.2 Skin Imaging	120

5.	Conclusions	128
6.	Future Work	131

References	133
------------	-----

APPENDIX:

<i>A. Printed Components</i>	
A.1. EIT System Components	143
A.2. Circular Electrode Array	158
A.3. Planar Electrode Array	160
<i>B. Data Acquisition Matlab Codes</i>	
B.1. Impedance Measurement Code	161
B.2. Calibration Code	165
B.3. Saline Solution Measurement Code	
B.3.1 Acquisition of 16 Data for the comprehension of the reliability of the Software in solving the forward problem	167
B.3.2 Acquisition of 256 Data for the comprehension of the reliability of the Software in recreating images	171
B.4. Acquisition Code	174
<i>C. Electrical Impedance Tomography EIDORS Codes</i>	
C.1. Simulations	
C.1.1. Forward Solving	180
C.1.2. Conductive, Insulating Objects	182
C.1.3. 3D Reconstruction of layers	183
C.2. Reconstructions	
C.2.1. Saline Solution Reconstruction	185
C.2.2. 2D Protocol: Reconstruction of Various Object	187
C.2.3. 3D Protocol: Reconstruction of a Tissue Section	189
C.2.4. 3D Protocol: Reconstruction of the Skin	191

Chapter 1

1.Introduction EIT

1.1 Background

Estimating the conductivity inside a volume from electrical measurements on its surface is an imaging modality known as Electrical Impedance Tomography (EIT).

EIT belongs to a family of electromagnetic images modalities along with electrical capacitance tomography (ECT) [13] [14], electromagnetic tomography (EMT) [15], and magnetic induction tomography (MIT) [16].

The basic idea of EIT is to reconstruct the internal electrical conductivity distribution of the medium by measuring the electrical potential on its boundaries, where an array of electrodes is attached, while this is subjected to a sequence of low-frequency current patterns.

A typical EIT system is a compact set of equipment mainly consisting of a data acquisition unit comprising a current source, the electrodes and all the necessary drivers and amplifiers, a computer with the impedance reconstruction and visualization code on board.

EIT has quite long history starting from the interest in measuring electrical properties of tissues, but using electrical current to “probe” the tissue to reveal information about its integrity, density, cellularity rather than recording its inherent electrical characteristics. For example, as early as 1901, King applied electrical current to patients with hypothyroidism, describing the disease as a low impedance state [10], and over the next two decades electrical impedance measurements were performed on blood and other body fluids to help characterize them in health and in disease. In 1926, it was demonstrated that electrical impedance could be used to detect a breast tumor [7] and in the 1940 impedance measurements were introduced for the study of blood flow, impedance plethysmography [8]. Around this time impedance methods were also applied to nerve. In the following decade, Kenneth and Robert Cole, also helped researchers interpret impedance measurements in biological tissues by introducing simple circuit representations of

the body introducing the “Cole-Cole plots”, that continue to be used to this day. In 1967, Geddes and Baker reported the specific resistance of biological tissues including body fluids, blood, cardiac muscle, skeletal muscle, lung, kidney, liver, spleen, pancreas, nerve tissue, fat, and bone, nearly covering all the main organs within human body [20]. It has also been shown that electrical properties of malignant tissues are significantly different from those of normal and benign tissues. Surowiec et al. have reported that the electrical resistance of malignant tumors decreases by a factor of 20 to 40 with respect to normal or benign tissues [21].

Henderson and Webster are credited with producing the first medical image based on impedance on 1978 [9], they created the first impedance imaging system, the Impedance Camera to study the pulmonary edema. They used a two-dimensional matrix of 100 electrodes on one side of the thorax and a single large electrode on the other to produce a transmission image of the tissue. The instrument makes 100 spatially specific admittance measurements per frame at rates up to 32 frames per second. They applied a 100KHz AC voltage signal to a large electrode on the chest, and measured the current through an array of 100 small electrodes on the opposite side using a single channel. However, the assumption they made was not valid because they assumed electric currents traveled in straight lines, which is not true. This work was probably the first attempt at electrical impedance imaging.

Since then, many studies have been focused on the area of electrical impedance imaging, and many feasible approaches have been proposed including electrical impedance tomography (EIT), magnetic resonance electrical impedance tomography (MREIT) (fig. 1), and magnetic induction tomography (MIT).

A tomographic impedance image involving a reconstruction algorithm was realized in 1982 by Barber and Brown [11] [12] (Sheffield group). They used 16 electrodes around the thorax and a back-projection method of image reconstruction, obtaining the first published tomographic images.

During the last twenty years there have been many research programs and great number of publications in medical areas, and recently, significant advances have occurred in EIT. For instance the group of Cherepenin et al. has published a 256 electrode system that provides a 3-D image of breast [5].

The technique of Electrical Impedance Tomography, which is focused on image reconstruction, has also garnered considerable engineering interest and remains an intense area of research. In

fact a 3D reconstruction engine developed for the EIT and Diffuse Optical Tomography Reconstruction Software (EIDORS) project [2].

In the past EIT was explored to become a generalized imaging modality. Though presenting lower signal to noise ratio [3] and lower spatial resolution [4] than other imaging modalities, EIT offers important strengths, such as high-speed data collection and soft tissue contrast which cannot be obtained from other imaging techniques. It has the potential for substantial impact on a number of clinical questions being a relatively low-cost technique [1].



Figure 1: 3T MRI system used for the MREIT measurements (<http://www.nbmdi.com/products/>).

1.2 Electrical Impedance Tomography as an Imaging Modality

In Electric Impedance Tomography electric currents are injected into a body with unknown electrical properties through a set of contact electrodes at the boundary of the body (fig.1.1.a), and the resulting voltages are measured on the same electrodes. The objective is to reconstruct unknown electric impedance distribution within the domain. This impedance distribution is obtained by an estimation algorithm, which relies on an accurate model of the electrical interaction, based on these boundary data. The impedance distribution is represented by an image (fig.1.1.b) and constitutes the solution of the inverse problem, as explained in chapter 1.5.

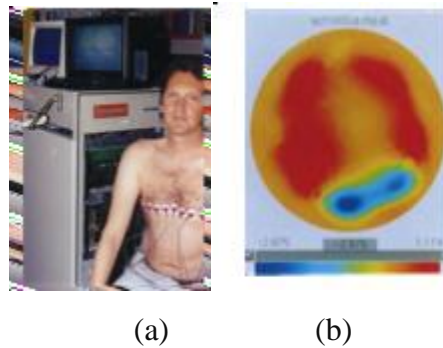


Figure 1.1: Electrical Impedance Tomography

(a) The EIT system developed by M.Cheney, D.Isaacson, J. C. Newell, 2000. It consists on 32 electrodes encircling the chest of a subject. (b) One ‘perfusion’ image obtained.

Impedance is known as electric conductivity and permittivity in complex case. It represents the electric properties of the body under study, since the electric conductivity is a measure of the ease with which a material conducts electricity and the electric permittivity is a measure of how readily the charges within a material separate under an imposed electric field. Both of these properties have seen much interest in medical applications for many years, because different tissues, or even the same tissue in different physiological states, have different conductivities and permittivities.

The process of property estimation is highly nonlinear, ill-conditioned and ill-posed [6] and there are three principal difficulties in image reconstruction for EIT:

B. the relationship between the permittivity/conductivity distribution and electrical voltages is nonlinear [17] and the electric field is distorted by the material present.

C. the number of independent measurements is limited, leading to an underdetermined problem.

D. the inverse problem is ill-posed and ill-conditioned, making the solution sensitive to measurements errors and noise [18].

These are important factors limiting the quality of the image obtained.

EIT is an ill-posed inverse problem means that large changes in impedance at the interior of the object may result in only small changes to the electrical measurements on its surface, and thus the EIT reconstruction is not stable to data perturbation or model errors [19]. To detect small size impedance variations within the object, effectively providing good spatial resolution, we need to estimate a large number of conductivity or permittivity parameters in the inverse problem, which further reduces the stability of the solution algorithm. Therefore, there is a trade-off, in the general case, between spatial resolution and stability. The fact that the electrical properties depend nonlinearly on the measured quantities makes this trade-off even more difficult.

The ill-posedness of the problem makes it unlikely that EIT images, even with many electrodes, can achieve resolution comparable to that of computed tomography (CT) or magnetic resonance imaging (MRI) images.

We can explain better this concept: ‘Soft-field’ modalities such as EIT, are intrinsically different compared to ‘Hard-field’ techniques like X-rays computed tomography, widely established in high resolution imaging. In an CT scanning process, parallel beams of X-rays are guided into the body under test from a suitable source while some detectors measure the attenuated beams as these emerge from the body. Since the procedure is repeated, rotating both sources and detectors around the body under test, in sequence, images of the attenuation coefficient

distribution inside the body are developed using analytic algorithms. This appears to be extremely efficient for this particular reconstruction problem in terms of its computational speed and the spatial solution of the image. This is mainly because the X-rays absorption at any point inside the body is completely independent from any other point. This is in fact a linear problem which leads to sparse and well-conditioned sensitivity matrices and very large data sets.

On the other hand, in EIT, being the current distribution inside the body function of the spatial distribution of the electrical properties, an electrostatic representation is most appropriate, describing the field throughout the body using the Laplacian equation [5]. As the field is modified throughout the body, the measured potential values at a given boundary location under a given excitation geometry is a nonlinear function of the distribution of the electrical parameters.

The relatively poor spatial resolution of the reconstructed images in impedance tomography is often quoted as its major disadvantage, compared with other already established tomographic scanners. To this respect, it must be clarified that the motivation for EIT is somewhat different from that of a conventional imaging modality. Despite its limited resolution, its task is to provide a portable and efficient imaging tool optimized for speed and contrast. In an abstract way, the reconstructed image can be seen as a source of information aiming to answer clinically-relevant questions about the interior electrical properties of a particular volume, rather than providing accurate morphological information. Depending on the particular application and resolution specifications, EIT can sometimes provide the optimum cost-effective solution.

EIT has many advantages over other medical imaging techniques. It is a non-invasive, and it does not expose the patient to X-rays or any other radioactive materials. It is a safe for long term monitoring. In addition EIT, combined with other medical imaging techniques can provide increased diagnostic accuracy. For example, if X-rays can only detect breast tumor that have an X-ray absorption that differs significantly from that of the normal breast tissue, EIT is based on the contrast in electrical properties of the tissue and can be used to find or distinguish tumors that are undetectable or indistinguishable by mammography [22].

1.2.1 Clinical Applications

Electrical Impedance Tomography, as said, is a new type of technology still under heavy development in recent years.

Two different modalities of images can be obtained as a result of the inverse problem solution and reconstruction: The absolute and differential ones.

Absolute imaging attempts to quantify the actual value of conductivity or permittivity inside an object. For such techniques, it is assumed that the properties of object do not change during the measurement process, so sometimes is also called static imaging. The technique is often used for characterizing biological tissue [48] [54] [55].

Instead, the aim of differential imaging, also known as dynamic imaging, is to reconstruct a change in conductivity rather than an absolute value, it reflects the change in the distribution of conductivity over the cross section. Dynamic EIT is of interest in studying physiological processes which modify the electrical conductivity of the body.

This technique has been used for imaging temporal phenomena in medical applications, such as impedance changes during respiration [23] [49]. This Thesis is especially concerned with absolute impedance imaging.

Other possible clinical applications of EIT include monitoring cardiac [25] and brain function [58] (fig. 1.3), detection and quantification of intraperitoneal fluid [26], detection and characterization of tumors [27] [56] [57], detection acute cerebral stroke [30], monitoring cancer ablation procedures and hypertermia [28] [29] [31] (fig.1.2), monitoring the freezing extent in cryosurgery [47], monitoring the change in conductivity of the tissues during the process of electroporabilization in electroporation [59], studying the emptying of the stomach [32] [50], studying pelvic fluid accumulation as a possible cause of pelvic pain [33], quantify severity of premenstrual syndrome by determining the amount of intracellular versus extracellular fluid [34], determining the boundary between dead and leaving tissue [35], and building forward models for bioelectric field inverse problems such as Electro/Magneto Encephalography (E/MEG) [36] [37], and Electro/Magneto Cardiography (E/MCG).

A variety of non clinical applications of EIT is also possible. These include imaging multi-phase fluid flow [38] [39], determining the location of minerals deposits in the earth [40][41], tracing

the spread of contaminants in the earth [42] [43] [44], non-destructive evaluation of machines parts [45], and control of industrial processes such as curing and cooking [46].

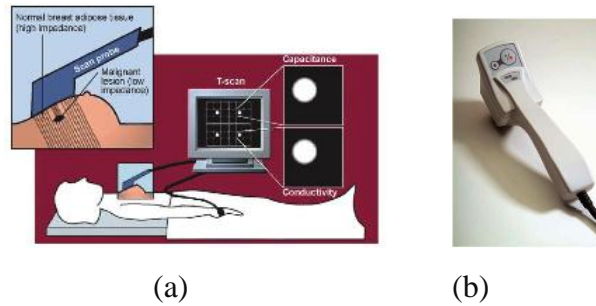


Figure 1.2: The EIT group in Moscow produced 3-D tomographic images of in vivo breast tissue from women with different hormonal status using a circular grid of 256 electrodes, 2010.
(a) Shows a patient under examination. (b) The EIT system (<http://www.nbmdi.com/products/>).

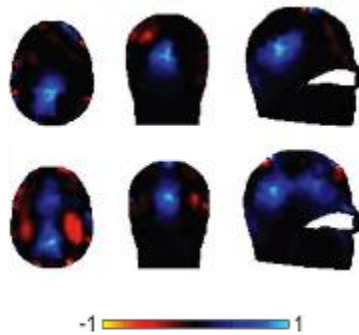


Figure 1.3: The UCL group (Departments of Medical Physics, University College London and Clinical Neurophysiology 2010, University College Hospital, London, UK) performed a number of measurements from human volunteers who were subject to visual, motor, and somatosensory stimuli to assess the applicability of EIT to the problem of imaging functional activity in the human brain.

1.3 EIT Theory

Electrical impedance methods are based on measurement of the electrical impedance, i.e., the modulus of the full complex resistance, of the human body or tissue.

All impedance methods relay upon the basic principle that if an alternating current is applied to a substance, energy will be dissipated as it travels through it, thus producing a measurable voltage. Moreover, the timing of the oscillations in the measured voltage will be out of phase with those of applied current.

The figure 1.4 helps to illustrate how the impedance measurements work. An alternating electrical current of known frequency, amplitude and timing, (i.e., the waveform crosses the x-axis at a specific time) is applied to a tissue. As the electrical current travels through the tissue, due to the tissue's inherent resistance, it loses energy, thus reducing the amplitude. Moreover, the timing of the resultant voltage alternations is slightly delayed, with it is no longer crossing the x-axis at the expected time, due to the substance's inherent capacitive and inductive characteristics.

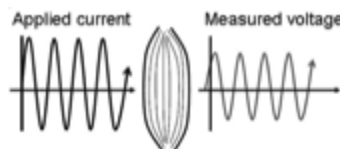


Figure 1.4: Basic concept of electrical impedance testing.

Electrical current of a known frequency, amplitude is injected into a tissue. The tissue impacts the applied electrical current, reducing the measured voltage's amplitude, secondary to the tissue's resistance and slightly altering its timing, secondary to the tissue's capacitance. The changes in electrical current flow reflect the properties of the tissue and thus can reveal information about tissue health or pathology.

Impedance can be described mathematically by Ohm's Law, which states that, for pure resistive circuits, without capacitors and inductors:

$$V = R I \quad (1.3.1)$$

where V , represents voltage, R , the resistance and I , the current.

For the complex representation of Kirchoff's laws [18], such elements are included and the equation becomes:

$$V = Z I \quad (1.3.2)$$

where Z represents the complex impedance of the circuit, a combination of its inherent resistance (R) and its reactance (iX), where X is a purely imaginary component. There are two types of reactance: the capacitive reactance (iX_C) and the inductive reactance (iX_L). Z is a vector, expressed as a complex number, composed of its resistance and two forms of reactance in combination:

$$Z = \sqrt{R^2 + (iX_C - iX_L)^2} \quad (1.3.3)$$

Fortunately, in medical applications this equation can be simplified by ignoring the iX_L term, since the inductance is believed to play a minimal role in standard bioimpedance measurements and the iX_C term can be simply written as iX .

Whereas the above equation can be applied to direct current circuits, it is most applicable to circuits utilizing alternating current, since in direct current circuits the current will simply stop following across the capacitor once it is fully charged; however, in alternating current circuits, current will flow indefinitely since it is constantly shifting direction.

We can also calculate the phase angle ϑ via standard trigonometric relationships by the formula:

$$\vartheta = \arctan (iX / R) \quad (1.3.4)$$

Thus, when discussing bioimpedance measurements in biological tissues, we should consider always all the components of the measured voltages mainly the phase angle which reflects to behavior of the sample we are studying. That was why, in this thesis, we used a Lock-in amplifier as measurement system and in every data acquisition file we measured all the voltage components.

In the literature two different electrode setups are used to measure the electric properties of biological materials: the two-electrode method and the four-electrode method.

In principle it could be supposed that tissue impedance could be measured by a couple of electrodes attached to the surface of the sample under study (two-electrode approach). Both of electrodes are used to inject the current and to measure the voltage drop (fig.1.5 a). The voltage in this case is measured across the entire circuit (fig.1.5 b). However the electrode-electrolyte impedances are in series with the sample impedance, and, therefore the measured impedance is the sum of the three impedances ($Z_x + Z_{e1} + Z_{e2}$). Unfortunately these parasitic impedances are sufficiently large to disturb the measurements, especially at low frequencies.

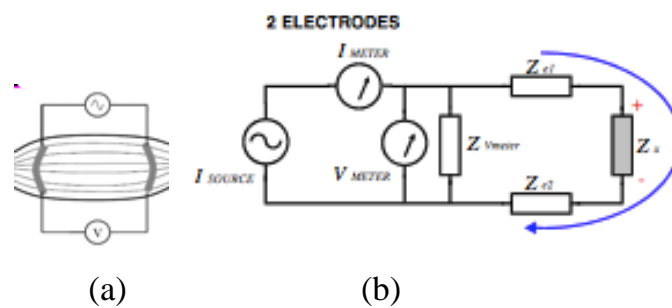


Figure 1.5: two-electrode method

(a) In the two-electrode approach, current is injected at the same location where the intervening voltage is measured.

(b) Equivalent Circuit.

Because of that, generally, two pairs of electrodes are used (four-electrode approach): the outer (current) electrodes, and the inner (voltage) electrodes. The current from the source passes through the sample. Voltage electrodes of known separation are placed in the sample between the current electrodes (fig.1-6 a b).

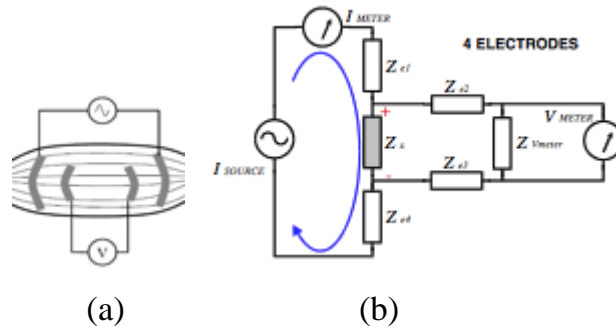


Figure 1.6: four-electrode method.

(a) In the four-electrode approach, current is injected separately. (b) Equivalent Circuit.

In EIT the conventional way of obtaining impedance measurement of an imaging domain, that could be an object as an biological sample or a part of human body, is to surround it with a certain number of source and probing electrodes as schematically shown in fig. 1.7. There are a number of variation of EIT system that depend on whether one injects current and measures voltages, and on whether one uses the same or different electrodes for this purpose, but most bioimpedance applications use the tetrapolar approach, since, it can help isolate an area of interest and being I and V independent, the polarization on the current electrodes has no influence on the voltage difference between the voltage electrodes.

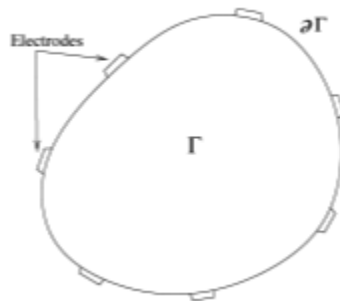


Figure 1.7: Schematic diagram of an EIT system.

In choosing the features of the system it is fundamental to consider the number of electrodes with respect to the resolution one can obtain. It has been shown in [91] that the resolution of an EIT system improves if one uses electrodes that fill as much as of the outermost surface as possible, that because it has been shows that the signal-noise ratio is approximately proportional to the square root of the fraction of the available circumference covered with electrodes [92] and this suggest using large electrodes.

The theory behind electrical impedance tomography is that by applying a constant current across a material, the voltage distribution resulting on the surface will reflect the internal impedance distribution. However, intuitively one will understand that multiple impedance distributions can produce the same voltage distribution at the surface. Therefore the system is stimulated in multiple manners to constrain the possible impedance distributions. Figure 1.7 shows a simple EIT diagram with 16 electrodes around the perimeter of a circular medium. In this setup the current, I , is applied across a pair of electrodes on opposite sides of the core while the voltage distribution, V_i , is measured between each set of neighboring electrodes. After the voltage around the entire perimeter has been measured, the current drive electrodes are rotated to the neighboring electrode, such that they remain opposite, and the voltage at all electrodes is measured once again. This process continues until 256 sets of voltage measurements are obtained.

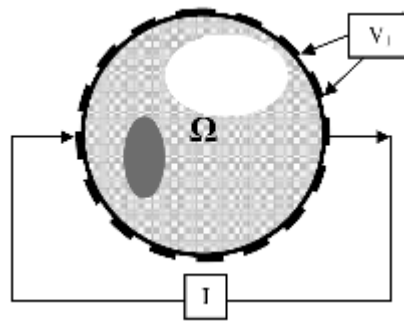


Figure 1.7: The EIT system based on tetrapolar approach with 16 electrodes.

The governing equation for the voltage field produced by placing a current across a material is shown below in Equation 1.3.5.

$$\nabla \cdot (\sigma + i \omega \varepsilon) \nabla u = 0 \quad (1.3.5)$$

Where σ and ε are the electric conductivity and permittivity of the medium, u is the electric potential, ω is the frequency. The sum of conductivity and permittivity is the complex admittivity of the medium, the impedance.

The EIT inverse problem is simply a system stimulation problem. The stimulation and resulting effect (injected current i and measured voltage V) are known, but the internal physical system is unknown (impedance distribution). The difficulty in solving this problem lies in the nonlinearity that arises in impedance itself, because the potential distribution is a function of the impedance it-self, and we cannot easily solve equation 1.3.5 for impedance [63].

For solving the EIT problem, it is important to consider the distribution of the electrodes and the fact that they cover a part of the surface under study. That because the presence of highly conductive electrode material on the surface of the body provides an effective short circuit for the applied current, which may reduce the current density at the interior of the body. We need therefore to mathematically model their presence. A sequence of electrode models was first introduced by Cheng et al. in [92]. These models in order of increasing fidelity (and complexity of the problem), are generally known as the continuum, gap, shunt and complete models.

The continuum model assumes the current density on the entire outer surface as known, but it is a poor model for real experiments because we do not know the entire current density, but in practice, we only know the currents that are sent down wires attached to electrodes, which in turn are attached to the body. The gap electrode model is a refinement of the continuum model which accounts for the discreteness of the electrodes. Electrodes are mathematically represented as a set of disjoint subdomains of the boundary. The current density is assumed to be nonzero and constant under an electrode, and zero in the gaps between electrodes. The shunt model accounts that metal electrodes provide a low-resistance path for the current. Modeling in addition the

contact impedance between the electrode and the body results in the complete model, that is superior to the previous models because it predicts the measured data more accurately [93].

1.3.1 Different Modalities for Electric Measurement of Impedance in EIT

An EIT system belongs to the class of the Pair drive instruments.

Pair drive instruments have a single current source and sequentially apply electrical currents to the body using a pair of electrodes. Voltage differences resulting from the stimulus are then measured between pairs of the remaining electrodes.

The way in which the driving pair is switched and the voltage measurements are collected in this type of instrument varies. Some of the most common configurations in medical applications use the adjacent, the cross and opposite methods.

Brown et al. suggested a method whereby the system sequentially applies electrical currents to the body using a pair of adjacent electrodes [1]. While current is applied to the body, voltages between adjacent non-current-carrying electrodes are measured. This procedure is repeated, applying current between each pair of adjacent electrodes to obtain a voltage data set.

Fig. 1.6 illustrates the application of this method for a circular volume conductor with 16 equally spaced electrodes. The current is first applied through electrodes 1 and 2 (see Fig. 1.8 a). One then measures the voltage using electrode pairs 3-4, 4-5, ..., 15-16. From these 13 voltage measurements the first four measurements are illustrated in Fig. 1.6 a. All these 13 measurements are independent. The next set of 13 voltage measurements is obtained by applying the current through electrodes 2 and 3, as shown in Fig. 1.8 b. This method, because the current is driven mostly in the outer region of the object, is very sensitive to conductivity contrasts near the boundary and almost insensitive to central contrasts, making the ill-posedness of the inverse problem even worse [65].

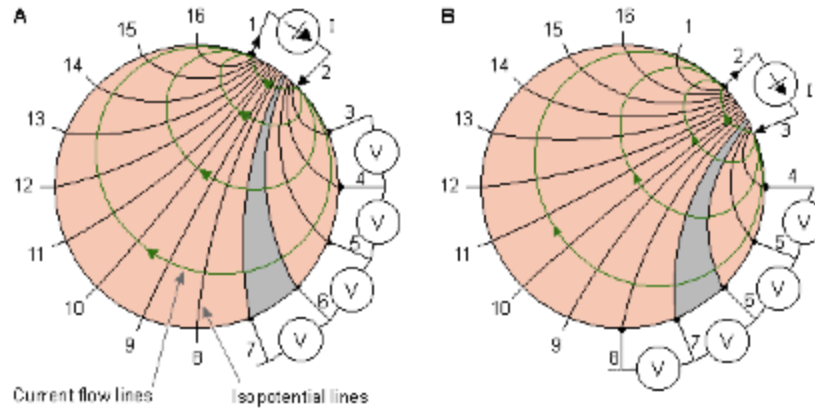


Figure 1.8: Adjacent method of impedance data collection illustrated for a circular volume conductor and 16 equally spaced electrodes.

(A) The first four voltage measurements for the set of 13 measurements are shown. (B) Another set of 13 measurements is obtained by changing the current feeding electrodes.

A more uniform current distribution is obtained when the current is injected between a pair of electrodes which are more separated from each other. Hua et al. suggested such a method called the cross method [64].

In the cross method, first one chooses two adjacent electrodes for current and voltage reference electrodes (for instance 16 and 1 in Fig. 1.9 a, respectively). The current is injected through electrode 2, and the voltages is measured for all other 13 electrodes with the aforementioned electrode 1 as the reference (the first four voltage measurements are again shown in Fig. 1.9 a). The current is then applied through electrode 4, and the voltage is again measured for all other 13 electrodes with electrode 1 as the reference, as shown in Fig. 1.9 b. One repeats this procedure using electrodes 6, 8, . . . 14; the entire procedure thus includes $7 \times 13 = 91$ measurements.

The measurement sequence is then repeated using electrodes 3 and 2 as current and voltage reference electrodes, respectively (see Fig. 1.9 c). Applying current first to electrode 5, one then measures the voltage successively for all other 13 electrodes with electrode 2 as a reference. This procedure is repeated again by applying current to electrode 7 (see Fig. 1.9 d). Applying current to electrodes 9, 11, ..., 1 and measuring the voltage for all other 13 electrodes with the afore-

mentioned electrode 2 as a reference, one makes 91 measurements. The cross method does not have as good a sensitivity in the periphery as the adjacent method, but has better sensitivity over the entire region [65].

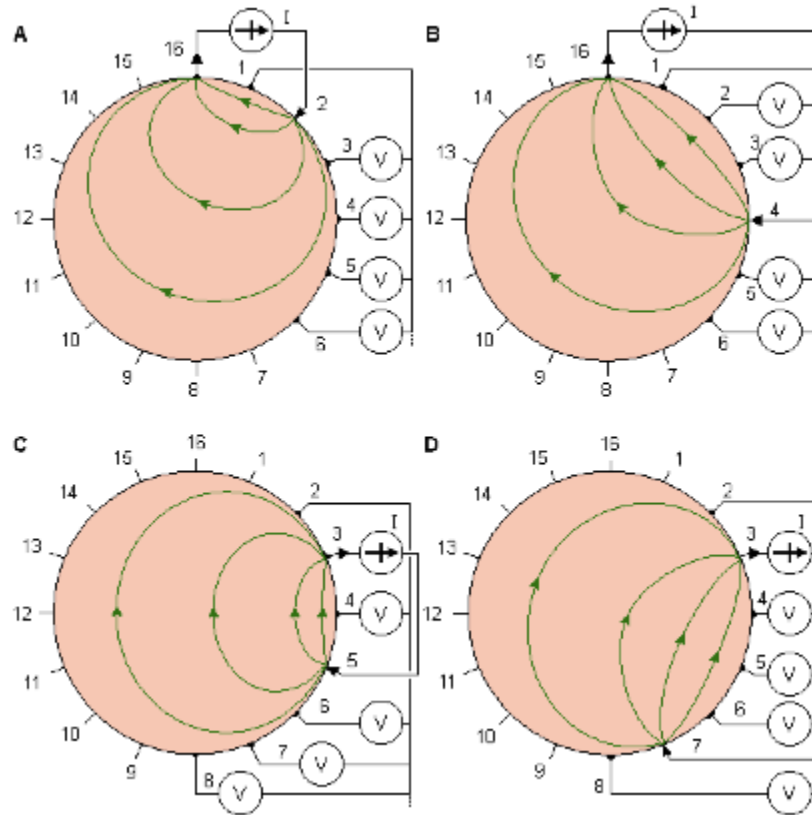


Figure 1.9: Cross method of impedance data collection.

(a), (b), (c), (d): The four different steps of this procedure.

As an alternative, Hua et al. introduced another method called the opposite method [64]. Fig. 1.10 illustrates the application of this method for a circular volume conductor with 16 equally spaced electrodes. In this method one injects current through two diametrically opposed electrodes (electrodes 16 and 8 in Fig. 1.10 a), and uses the electrode adjacent to the current-

injecting electrode as the voltage reference. The next set of 13 voltage measurements is obtained by selecting electrodes 1 and 9 for current electrodes (see Fig. 1.10 b). The current distribution in this method is more uniform and, therefore, has a better distribution of the sensitivity than the cross method [65].

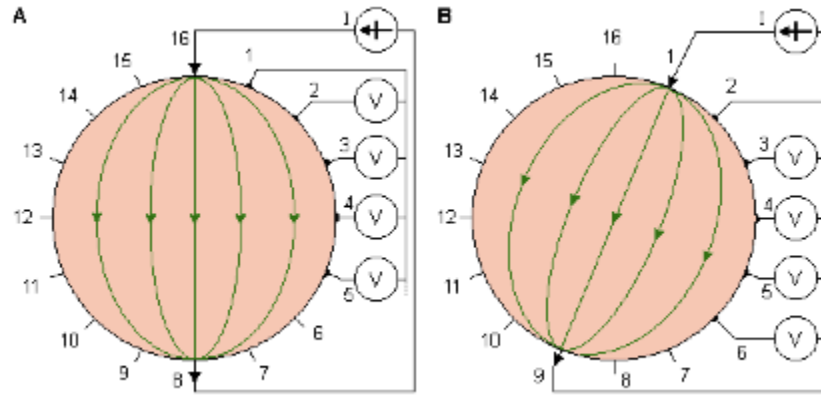


Figure 1.10: Opposite method of impedance data collection.

(a),(b) : The two different steps of this procedure.

1.4 The Inverse Problem

The inverse, or reconstruction, problem is to obtain an approximation to the conductivity/permittivity map in the interior from the boundary measurements. The inverse, or reconstruction, problem is to obtain an approximation to the conductivity/permittivity map in the interior from the boundary measurements. In 1932, Hadamard attempted to describe the generic properties of such problem which arise from physical and natural phenomena [35]. In these, a given set of observations is always uniquely mapped to a given set of admissible rational

solution. Thus, according to Hadamard, in a well-posed problem for any set of rational observation

- (a) A solution consistent with the observations exists.
- (b) The solution is unique.
- (c) The solution depends continuously on the observations.

In Hadamard's meaning, problems failing this criteria could have never arisen from a physical system, and somehow these would have been misinterpreted and posed incorrectly, hence the name ill-posed. Despite this, the inverse admittivity problem is undoubtedly ill-posed, because a small change in conductivity/permittivity next to a physically conductive area will have a smaller effect on the boundary voltages. The relationship between the admittivity changes and the corresponding differential boundary voltages is also not linear, and although some naturally imposed constraints may somehow suggest, though not guarantee, the validity of the first two criteria, it certainly fails the third one, because even small perturbations in the measurements can lead to wild oscillations in the solution.

In order to solve the inverse problem a consideration should be done: In principle, measuring both the amplitude and the phase angle of the boundary voltages can result in images of the electrical conductivity and permittivity distributions in the interior volume. Despite this, the fact that electrostatic fields are ideally required, alternating current patterns are often preferred in order to avoid polarization effects. In the frequency range lower than 100 KHz, the magnetization component of the current is negligible and the phase angles are maintained relatively small, thus usually the real part of the voltages is a few hundred times greater than the imaginary. In absence of phase angle readings in the data, only the conductivity (or equivalently the resistivity) distribution can be reconstructed. Said that, if the difference between the conductivity of an object and its surroundings is small, this nonlinear problem can be approximated to a linear one in the form:

$$V = J G \quad (1.4.1)$$

where $V \in R^{m \times l}$ is the measurement vector of the boundary voltages, $J \in R^{m \times n}$ is the sensitivity matrix or Jacobian and $G \in R^{n \times l}$ is the vector representing the impedance distribution, m is the number of the independent measurements, and n is the number of the conductivities in the area of interest.

To obtain the conductivity map inside the volume equation (1.4.2) must be inverted for

$$G = J^{-1} V \quad (1.4.2)$$

Equation (1.4.1) and (1.4.2) show the forward and inverse processes of the image reconstruction, respectively.

Obviously, to reconstruct an EIT image from the voltage measurements, (1.4.1) has to be solved. However there are several difficulties associated with the inverse of the sensitivity matrix J : being generally not square, it has no direct inverse and a pseudoinverse of the Jacobian is required; being ill-posed and since there are fewer independent measurements than unknown conductivity values, many alternative images are possible; being ill-conditioned, i.e., its condition number of the sensitivity matrix, defined as the ratio of largest singular value of the matrix to its smallest one, is typically very large, result in magnification both of measurement and numerical errors in the reconstructed image.

When approaching an ill-posed problem, the tendency is to replace it with one of which is somewhat different but ‘less ill-posed’. Ill-posed problems ‘suffer’ from an inherent shortage of information, therefore instead to attempt to solve the original problem one often opts to solve a similar one which is less demanding or one for which more information is available. This transformation can be achieved in a variety of ways, with regularization amongst the most popular ones. Regularization is essentially a means for providing to the inverse problem some prior information about the solution, and in this sense it can be viewed as a constraint preserving the existence and the uniqueness but also the stability of the solution. From another perspective, regularization can be interpreted as a means to trade-off the influence of measurements on the solution against its compliance with the prior assumptions.

The most majority of existing algorithms for image reconstruction in EIT follow these fundamental steps:

- a) Find the Solution for the Forward Problem. A forward solver capable of predicting the voltages on electrodes, at least as accurately as the measured data, for a given conductivity distribution is essential for EIT reconstruction.
- b) Calculate of the sensitivity matrix, which is the Jacobian of the discrete forward operator. The forward solver is called to compute the voltages on the electrodes and the internal electric potential is required to assemble the Jacobian matrix for the inversion [90].
- c) Invert of the sensitivity matrix. The voltages measurements are then converted to permittivity image by solving a regularized inverse model typically formulated on a finite-element mesh.
- d) Reconstruct of the image.

Many reconstruction algorithms have been proposed by a number of research groups. These approaches fall into several different categories. I outline several of the different approaches and then in 1.4.1 section describe in more detail the methods I used to make the images that accompany this Thesis.

The diagram in figure 1.11 gives a brief overview on the types of the already available reconstruction algorithms for the EIT problem. These are generally divided in probabilistic-statistical methods (Kipio, Kolehmainen, Somersalo, Vauhkonen) [81] [82] [83] [84], deterministic methods based on linearization (Allers, Barber and Brown, Blue, Calderón, Cheney, Goble, Isaacson, Newell) [66] [67] [68] [69] [70] [71] [72] [73], and deterministic nonlinear inversion methods (Berryman, Webster, Wexler, Lionheart, Vauhkonen, Borsic, Arridge) [74] [75] [76] [77] [78] [79] [80].

The linearized algorithms, suitable for solving the linearized inverse problem, are subdivided in direct methods that use a single regularized step, such as Tikhonov regularization [85] and one-step Newton methods [48] [86] [87] [88], and iterative methods which regularize by iteration, such as the conjugate gradients algorithm [89]. The nonlinear algorithms on the other hand, capable of reconstructing high-contrast inhomogeneities by tackling the nonlinear inverse problem, are mostly iterative, typically Newton-type with a linear regularized step.

The images in this Thesis were made with a one-step Newton method (NOSER) that is close to an approximate linearization and it has been preferred to iterative methods for its lower computational time. This I discuss in more detail below in paragraph 1.5.

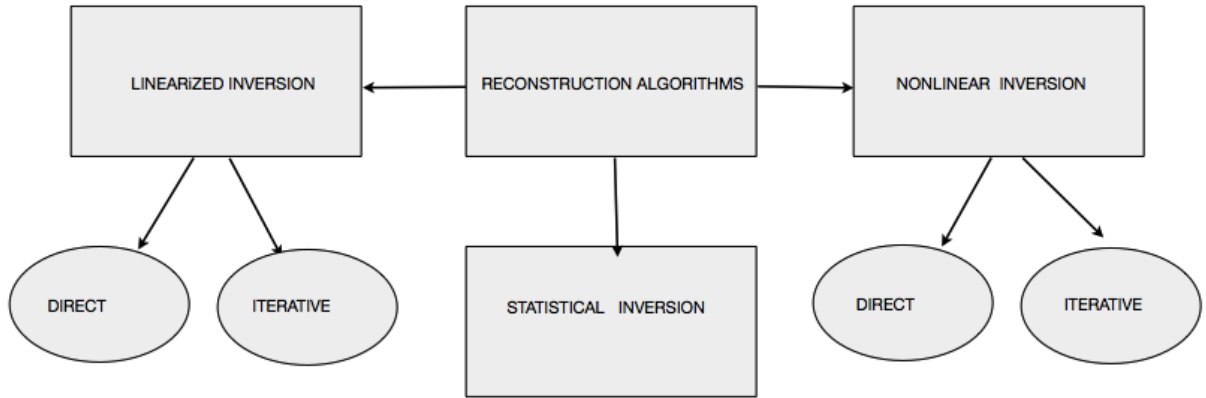


Figure 1.11: Reconstruction algorithms for EIT.

1.5 Algorithms for the Ill-posed Problem

For solving the EIT problem I used EIDORS, that is a freely available software officially released under GNU General Public license by Vauhkonen [94] at the second half of 2000, as a complete package for two dimensional EIT problems. Being most medical problems fundamentally three dimensional, in 2002 Polydorides and Lionheart released a free toolkit of Matlab routines which can be employed to solve the forward and inverse EIT problems in three dimensions. In order to tackle the nonlinear and ill-posed problems, EIDORS employs the Finite Element Method (FEM) to solve the forward calculation. The finite element solver included in the toolkit uses the complete electrode model to compute boundary problems involving models with first-order triangular and tetrahedral elements. Simple files with primitive commands define the geometry of the desired domains comprising vertices (nodes) and simplices (vertices). These are imported into ready-available mesh generators, such as NETGEN [127]. In order to solve the inverse problem, EIDORS employs regularized Newton's methods and the result is a set of

impedance values, which correspond to the measurements by the electrodes. Below I describe the mathematical model for EIT. The model involves some of the theory that underlies the design of the EIT system utilized for this Thesis, and then I focus on discretization and finite element formulation, the forward computation, the calculation of the Jacobian matrix and, finally, on the algorithm used to make the images accompanying this Thesis.

1.5.1 Mathematical Model of the Physical System

In order to model the physical system, an accurate model of volume is imperative. This must respect the dimensions, the boundary geometry and the structural characteristics of the physical volume. In addition, the boundary electrodes must be accurately modeled.

The mathematical model comes from the Laplacian equation derived from Maxwell's equations from electro-magnetics. In the following equation E is the electrical field in the interior of the volume, B the magnetic field, ρ the charge density, j the current density, v the outward unit normal vector, c the speed of light and ϵ_0 the dielectric permittivity *in vacuo*. For a conductive isotropic volume Ω enclosed by boundary $\delta\Omega$, Maxwell's equation state that the flux E through a closed surface equals the total charge density inside divided by ϵ_0 .

$$\nabla \cdot E = \frac{\rho}{\epsilon_0} \quad (1.5.1)$$

In addition, the linear integral of E around a loop is equal to the negative rate of change the flux of B through the loop, yielding

$$\nabla \times B = -\frac{\partial B}{\partial t} \quad (1.5.2)$$

the flux B through a closed surface is equal to zero,

$$\nabla \cdot B = 0 \quad (1.5.3)$$

and the integral of B around a loop is equal to the current flowing through the loop plus the rate of change of the flux of E through the loop divided by a constant c^2 , yielding

$$\nabla \times B = \frac{j}{\epsilon_0} + \frac{\partial E}{\partial t} \quad (1.5.4)$$

In EIT the excitation conditions are quasi-static as the driving patterns are time-harmonic AC signals at a low frequency ω . However, if the measurements for each pattern are thought to be collected instantaneously, then static conditions can be assumed. In effect, the magnetization components can be safely neglected, hence

$$\frac{\partial B}{\partial t} \approx 0 \quad \text{and} \quad \frac{\partial E}{\partial t} \approx 0 \quad (1.5.5)$$

Using these, equation (1.5.2) becomes

$$\nabla \times E = 0 \quad (1.5.6)$$

From vector calculus theory, when the curl of the vector E is equal to zero, then there exists a scalar u whose gradient is equal to that vector, in particular

$$E = -\nabla u \quad (1.5.7)$$

When ‘static’ current patterns are injected, under the assumptions (1.5.5), equation (1.5.4) becomes

$$\nabla \times B = \frac{j}{\epsilon_0} \quad (1.5.8)$$

In these conditions the current density j can be assumed to be time invariant. If I_n^d is the n 'th current pattern driven into volume, from a boundary electrode surface s then

$$I_n^d = \int_s j \cdot v \, ds \quad (1.5.9)$$

From the charge conservation law, if S is the surface of $\delta\Omega$

$$\int_s j \, dS = - \frac{d}{dt} (Q_\Omega) \quad (1.5.10)$$

the charge in the interior of the volume Q_Ω can be expressed as a volume integral of the charge density as

$$Q_\Omega = \int_\Omega \rho \, dV \quad (1.5.11)$$

Combining (1.4.12), (1.4.10), and (1.4.11) yields

$$\nabla \cdot j = - \frac{\partial \rho}{\partial t} \quad (1.5.12)$$

which is basically another expression for the charge conservation theorem, according to which the flux of the current flowing through a closed surface is equal to the negative rate of change of charge density in the interior. Since there are no current sources in the interior of the volume and E does not change with time, the right hand side of the equation (1.5.) can be set to zero

$$\nabla \cdot j = 0 \quad (1.5.13)$$

In the linear isotropic medium the current density and the electric field are related by the approximation

$$j \approx \gamma E \approx (\sigma + i \omega \epsilon) E \quad (1.5.14)$$

where σ is the electric conductivity, ε the electrical permittivity and γ the complex admittivity of the medium. Substituting (1.5.14) into (1.5.13) leads to

$$\nabla \cdot \gamma E = 0 \quad (1.5.15)$$

which combined with (1.5.7) yields the Laplacian partial differential equation

$$\nabla \cdot \gamma(-\nabla u) = 0 \quad (1.5.16)$$

$$\nabla \cdot (\gamma \nabla u) = 0 \quad (1.5.17)$$

This nonlinear partial differential equation representing the electrodynamics of EIT is known as Governing Equation of EIT and has an infinite number of solutions. Boundary conditions required to restrict these solutions can be applied to specify the value of certain parameters on the surface. These may be either the potential at the surface (Dirichlet conditions) and/or the current density crossing the boundary (Neumann conditions).

The mixed Dirichlet and Neumann boundary conditions accompanying the Laplacian equation (1.5.17) are formally known as the complete electrode model (CEM), which, as said, is superior to the previously used continuum, shunt and gap models because of its better resemblance to the physical system, encapsulating the contact impedance of the electrodes. If Γ_1 is the subset of the surface of the volume underneath the electrodes, then the associated current density is

$$\gamma \frac{\partial u}{\partial \nu} = j \quad \text{on } \Gamma_1 \quad (1.5.18)$$

while for the rest of the surface $\Gamma_2 = \partial\Omega \setminus \Gamma_1$,

$$\gamma \frac{\partial u}{\partial \nu} = 0 \quad \text{on } \Gamma_2 \quad (1.5.19)$$

In addition, for each of the electrodes the integral of the current density over the whole electrode surface s is equal to the total amount of current I_l flowing to or from that electrode,

$$\int_{E_l} \gamma \frac{\partial u}{\partial \nu} dS = I_l \quad l= 1, \dots, L \quad (1.5.20)$$

where L is the number of the electrodes in the system (Neumann Boundary Condition). Finally, the value of potential V_l measured on the l 'th electrode is equal to the sum of the potential on the boundary surface underneath that electrode and the potential drop across the electrode's contact impedance z_l (Ω/m^2) (Dirichlet Boundary Condition)

$$u + z_l \gamma \frac{\partial u}{\partial \nu} = V_l \quad l= 1, \dots, L \quad (1.5.21)$$

The model has been shown to have a unique solution when the charge conservation theorem

$$\int_{\delta\Omega} j = 0 \Leftrightarrow \sum_{l=1}^L V_l = 0 \quad (1.5.22)$$

is considered, and a choice of ground is made,

$$\int_{\delta\Omega} u = 0 \Leftrightarrow \sum_{l=1}^L V_l = 0 \quad (1.5.23)$$

1.5.2 Discretization and Finite Element Formulation

When the problem is solved numerically, the model of the physical system must be discretized, requiring an approximate formulation of the problem. The accuracy of the approximation is strongly dependent on the smoothness of the analytical solution to the Laplacian equation (1.5.17), which in turn depends on the smoothness in the measurements. Piecewise assumptions about the regularity of the forward solution (potential) and the input data (admittivity) can be formulated considering classes of discrete functions with specific integrability properties. Usually the transformation from the continuum domains and integral operator functions to the discrete domains and matrix operators is achieved by some numerical integral approximation methods such as the Galerkin methods [95]. In the discretization process it is essential that both the solution and the data are taken to be functions over some spaces. Despite using only finite sets of parameters, infinite dimensional spaces are preferred as they reflect the fact that behavior resemblance between the physical-continuous system and its discrete model becomes higher as the number of parameters increased. In EIT, infinite dimensional Hilbert spaces are often used to represent admittivity distributions and boundary measurements.

In this Thesis, In this Thesis, for the finite approximations of the forward problem, the Galerkin three dimensional formulation is used [60]. In this, the admissible measurements and the solutions are considered to belong to the Hilbert spaces, and the forward nonlinear operator is formalized as

$$F : \gamma|_{\Omega} \rightarrow V|_{\delta\Omega} \quad (1.5.24)$$

hence given a model, the forward operator F can also thought of as a Neumann-Dirichlet operator associated with γ .

The finite element formulation for EIT, first discretizes the medium under analysis into a finite number of elements collectively called a finite element mesh. Within each element the nodal values are approximated by shape functions (interpolation functions).

Before showing how the Galerkin approach develops into the EIT forward solver, the weak-variational form of the problem must be derived first. If u_h is the required weak solution to the

problem, or better defined as a finite dimensional approximation for the weak solution and Φ_i are some piecewise linear basis functions with limited support such that

$$\Phi_i(x, y, z) = \begin{cases} 1, & \text{on vertex } i \\ 0, & \text{otherwise.} \end{cases} \quad (1.5.25)$$

then

$$\sum_{i=1}^n U_i \Phi_i = 0 \quad (1.5.26)$$

where U_i is the value of the potential at vertex i and n the number of vertices in the model. From (1.5.26) it is clear that u_h is a linear combination of the functions Φ_i weighted by the U_i vector. Based on equation (1.5.26), the array of FEM parameters U must be evaluated such that

$$\sum_{i=1}^n (U_i \iiint_{\Omega} \gamma (\nabla \Phi_i \cdot \nabla \Phi_j) dx dy dz) = 0 \quad j=1, \dots, n \quad (1.5.27)$$

For FEM derivations the discrete conductivity distribution vector γ is taken as

$$\gamma = \sum_{i=1}^k \gamma_i \varphi_i \quad (1.5.28)$$

where

$$\varphi_i(x, y, z) = \begin{cases} 1, & \text{on element } i \\ 0, & \text{otherwise.} \end{cases} \quad (1.5.29)$$

are piecewise constant functions or, better, the nodal basis functions of the finite element mesh.

Combining the Laplacian (1.5.17) with equation (1.5.26) leads to

$$\iiint_{\Omega} \gamma \cdot \nabla \Phi_i \cdot \nabla u_h dx dy dz = 0 \quad i=1, \dots, n \quad (1.5.30)$$

and then applying Green's second identity on (1.5.30) yields

$$\iiint_{\Omega} \gamma \cdot \nabla \Phi_i \cdot \nabla u_h \, dx \, dy \, dz = \iint_{\delta\Omega} \gamma \, \Phi_i \nabla u_h \, ds \quad i=1, \dots, n \quad (1.5.31)$$

where

$$\nabla u_h = \frac{\partial u_h}{\partial v} \quad (1.5.32)$$

and s is a boundary surface measure.

According to the Galerkin method, equation (1.5.31) must be applied to each of the elements in the model. For the needs of the derivation, a finite element model with k first-order tetrahedral elements, n vertices and L boundary electrodes is assumed. For an element underneath the electrode l , let Ω_E be the volume of the element and $\delta\Omega_E$ its triangular face shared with the electrode. Equation (1.5.31) for the particular element becomes,

$$\iiint_{\Omega_E} \gamma \left(\frac{\partial \Phi_i}{\partial x} \frac{\partial u_h}{\partial x} + \frac{\partial \Phi_i}{\partial y} \frac{\partial u_h}{\partial y} + \frac{\partial \Phi_i}{\partial z} \frac{\partial u_h}{\partial z} \right) dx \, dy \, dz = \iint_{\delta\Omega_E} \gamma \, \Phi_i \frac{\partial u_h}{\partial v} \, ds \quad (1.5.33)$$

for $i=1, \dots, 4$ and plugging in the boundary condition (1.5.20) yields,

$$\iiint_{\Omega_E} \gamma \left(\frac{\partial \Phi_i}{\partial x} \frac{\partial u_h}{\partial x} + \frac{\partial \Phi_i}{\partial y} \frac{\partial u_h}{\partial y} + \frac{\partial \Phi_i}{\partial z} \frac{\partial u_h}{\partial z} \right) dx \, dy \, dz = \iint_{\delta\Omega_E} \Phi_i \frac{1}{z_l} (V_l - u_h) \, ds \quad (1.5.34)$$

where z_l is the contact impedance of the electrode l and V_l the potential measured on it.

Substituting u_h from (1.5.26) leads to

$$\iiint_{\Omega_E} \gamma \left(\frac{\partial \Phi_i}{\partial x} \frac{U_j \partial \Phi_j}{\partial x} + \frac{\partial \Phi_i}{\partial y} \frac{U_j \partial \Phi_j}{\partial y} + \frac{\partial \Phi_i}{\partial z} \frac{U_j \partial \Phi_j}{\partial z} \right) dx \, dy \, dz = \iint_{\delta\Omega_E} \Phi_i \frac{1}{z_l} (U_j \partial \Phi_j - V_l) \, ds \quad (1.5.35)$$

with $i, j=1, \dots, n$.

Generalizing equation (1.5.35) for the n 'th element, the global conductance matrix A is assembled by evaluating the following entries for each of the elements. These entries formalized

as local matrices A_m , A_z and A_v arise from the various factors of (1.5.35) and depend on the actual location of the element. The local matrices are

$$A_m(i, j) = \iiint_{\Omega_E} \gamma \left(\frac{\partial \Phi_i}{\partial x} \frac{\partial \Phi_j}{\partial x} + \frac{\partial \Phi_i}{\partial y} \frac{\partial \Phi_j}{\partial y} + \frac{\partial \Phi_i}{\partial z} \frac{\partial \Phi_j}{\partial z} \right) dx dy dz \quad i, j = n_1, \dots, n_4 \quad (1.5.36)$$

$$A_z(i, j) = \iint_{\delta\Omega_E} \Phi_i \frac{1}{z_l} \Phi_j ds \quad i, j = n_1, \dots, n_4 \quad (1.5.37)$$

$$A_v(i, j) = \iint_{\delta\Omega_E} -\frac{1}{z_l} \Phi_i ds \quad i, j = n_1, \dots, n_4 \quad (1.5.38)$$

$$A_d(i, j) = \begin{cases} \left(\frac{1}{z_l}\right)_l |E_l| & \text{for } i = j \\ 0 & \text{otherwise.} \end{cases} \quad i, j = 1, \dots, L \quad (1.5.39)$$

where n_1, \dots, n_4 are the four vertices in each element and E_l is of the face of the electrode.

For the exact derivation of the local matrices, I suggest referring to [95]. For a finite set of current patterns, the forward problem is formulated as a system of linear equations

$$\begin{pmatrix} A_m + A_z & A_v \\ A_v^T & A_d \end{pmatrix} \begin{pmatrix} U \\ V_l \end{pmatrix} = \begin{pmatrix} 0 \\ I^d \end{pmatrix} \quad (1.5.40)$$

where is U the nodal potential distribution and V_l the potential values on the boundary electrodes. Before the system (1.5.40) can be solved, the additional conditions (1.5.41) (1.5.42) must be imposed in order to preserve the existence and uniqueness of the forward solution [93]. If I is the value of current injected by l 'th electrode, then for a set of k driving current patterns

$$I^d = (I_1^d \quad I_2^d \quad \dots \quad I_k^d) \quad (1.5.41)$$

and on I^d the conservation of the charge theorem imposes

$$\int_{\delta\Omega} j = \sum_{i=1}^k I_j^d = 0 \quad (1.5.42)$$

Given a finite element model with known admittivity distribution and a set of current patterns, the potential at the vertices of the model and the boundary electrodes can be calculated from equation (1.5.40). This process is referred as the forward computation. Expressing (1.5.40) in a more condensed form, the forward problems becomes

$$A u = b \quad (1.5.43)$$

with $u = (U \ I^d)$ and $b = (0 \ I^d)^T$ having an algebraic solution

$$u = A^{-1} b \quad (1.5.44)$$

In contrast to the inverse problem, this is a well-posed, easy to solve problem because the coefficients matrix A

- is very sparse due to the limited support in the elements of the model
- is square and full-rank, therefore the solution is unique
- is symmetric and so is its inverse, enabling the decomposition of A in smaller factors whose inverse is easier to compute
- is well-conditioned for inversion, thus a stable solution exists.

1.5.3 Forward Computation

In general, the forward problem can be solved either directly or iteratively. It has been noted that, being a finite approximation weakly depending on the quality and smoothness of the model, the forward problem should be solved iteratively, as EIDORS does. Consequently, trying to solve the problem ‘ exactly ‘ has no impact on the quality of the outcome, as it bears no significance in trying to ‘ reproduce ‘ the data more accurately than they can actually be measured. The problem must be solved to a tolerance compatible with the quality of the actual measurements.

One of the most suitable iterative schemes for the forward problem is the linear preconditioned conjugate gradients (PCG) iteration. This iterative algorithm generates a sequence of solutions which minimize the least square residual

$$\operatorname{argmin} \frac{1}{2} \|A u - b\|_2^2 \quad (1.5.45)$$

and it requires the matrix A to be positive-definite in order for the iteration to be able to converge. The algorithm is classified under low-storage numerical techniques, because it avoids the computation of large components which are computationally expensive to store and handle. The properties and special characteristics of the linear PCG iteration are well established and documented in [96] [97] [98] [99] [100].

If M is a proper preconditioner, the modified forward problem becomes

$$M^{-1} A u = M^{-1} b \quad (1.5.46)$$

which has solution identical to the original problem, where, however, only this time the convergence depends on the properties of the $M^{-1} A$ matrix than A alone. The matrix M must be positive-definite and well-conditioned, so that its inverse can be easily computed. The preconditioner is selected in a way that

$$M^{-1} A \approx I \quad (1.5.47)$$

where I is the identity matrix. Setting an initial estimate of the potential distribution u_0 , the resulting residual vector r_0 and an initial (steepest descent) search direction $p_0 = A r_0$, the PCG iteration is described in figure 1.12.

```

while  $\|r_i\|_2 < \varepsilon$  do
   $z_i = M^{-1}r_i$ 
  if  $i > 0$ 
     $\beta_i = r_i^* z_i / r_{i-1}^* z_{i-1}$ 
     $p_i = z_i + \beta_i p_{i-1}$ 
  end
   $\alpha_i = r_i^* z_i / p_i^* A p_i$ 
   $u_{i+1} = u_i + \alpha_i p_i$ 
   $r_{i+1} = r_i - \alpha_i A p_i$ 
   $i \leftarrow i + 1$ 
end

```

Figure 1.12: The preconditioned CG iteration. The scalar parameter denotes the tolerance

Usually the first search direction is along the steepest descent, while the iterative solution is obtained by stepping distance α_i towards the current direction p_i . The characteristic properties of the CG iteration can be summarized considering two successive iterations i, j . In these the residuals are M-orthogonal or M-conjugate,

$$r_j^T M r_i = 0 \quad (1.5.48)$$

the residual of the one iteration and the direction vector of the other are M-conjugate

$$r_j^T M p_i = 0 \quad (1.5.49)$$

and the directions are A-conjugate

$$p_j^T A p_i = 0 \quad (1.5.50)$$

1.5.4 Calculation of the Jacobian Matrix

When the admittivity is purely real, then any given set of low-frequency current patterns give rise to a purely real set of potential measurements at the boundary. Calculating the Jacobian J_{γ_p} for a distribution γ_p , if $F(\gamma_p)$ are the boundary measurements in response to γ_p , then the real discrete linearized forward problem is

$$J_{\gamma_p} (\gamma - \gamma_p) = V - F(\gamma_p) \quad (1.5.51)$$

Where γ is the perturbed admittivity distribution and V the boundary measurements with respect to γ . By definition, the Jacobian is the discrete derivative of the nonlinear function which maps the perturbations of the solution to perturbation on the boundary data.

$$DF : \Delta \gamma|_{\Omega} \rightarrow \Delta V|_{\partial\Omega} \quad (1.5.52)$$

Denoting

$$V(I^d) = (V(I_1^d) \ V(I_2^d) \ ... \ V(I_k^d)) \quad (1.5.53)$$

the vector of the boundary measurements corresponding to k driving current patterns, the Jacobian matrix J has the form

$$J = \begin{bmatrix} \frac{\partial V(I_1^d)}{\partial \gamma_1} & \dots & \frac{\partial V(I_1^d)}{\partial \gamma_k} \\ \vdots & \ddots & \vdots \\ \frac{\partial V(I_k^d)}{\partial \gamma_1} & \dots & \frac{\partial V(I_k^d)}{\partial \gamma_k} \end{bmatrix} \quad (1.5.54)$$

where k is the number of degrees of freedom in the model. The Jacobian is a linear, compact and positive operator on infinite Hilbert spaces. Furthermore, being a compact operator it has a discontinuous inverse, causing J^{-1} to be unstable against variations in the data, effectively violating Hadamard's third criterion for well-posedness.

For two-dimensional models the Jacobian is calculated using its definition (1.5.54). In this procedure, each of the elements is in turn perturbed by a small amount $\delta\gamma$ and then, solving the forward problem, the perturbation δV caused on the boundary measurement is calculated.

However, when the finite element models are three-dimensional with a large number of degrees of freedom, this method is extremely inefficient and is normally avoided. Following an adjoint problem formulation, the Jacobian can be calculated quite efficiently as the dot product of the current and measurement fields (these hypothetical fields can be calculated when the measurement patterns are considered to be current patterns) with the integrals of the gradients of the shape functions over each element [101] [86]. From the weak form of the Laplacian, as obtained by Green's second identity, then

$$\iiint_{\Omega} \gamma \nabla u \cdot \nabla w \, dx \, dy \, dz = \iint_{\partial\Omega} w \gamma \frac{\partial u}{\partial \nu} \, ds \quad (1.5.55)$$

In particular for $w = u$ the power conservation formula becomes

$$\iiint_{\Omega} \gamma |\nabla u|^2 \, dx \, dy \, dz = \iint_{\partial\Omega} u \gamma \frac{\partial u}{\partial \nu} \, ds = \sum_{l=1}^L \iint_{E_l} \left(V_l - z_l \gamma \frac{\partial u}{\partial \nu} \right) \gamma \frac{\partial u}{\partial \nu} \, ds \quad (1.5.56)$$

hence

$$\iiint_{\Omega} \gamma |\nabla u|^2 dx dy dz + \sum_{l=1}^L \iint_{E_l} \left(\gamma \frac{\partial u}{\partial v} \right)^2 z_l ds = \sum_{l=1}^L V_l I_l \quad (1.5.57)$$

This simply states that the power input is dissipated either in the domain Ω or by the contact impedance layer under the electrodes. Taking perturbations $\gamma \rightarrow \gamma + \delta\gamma$ and $u \rightarrow u + \delta u$, with the current in each electrode I_l held constant, and ignoring second order terms yields

$$\begin{aligned} & \iiint_{\Omega} \delta\gamma |\nabla u|^2 dx dy dz + 2 \iiint_{\Omega} \gamma \nabla u \cdot \nabla \delta u dx dy dz + \\ & + 2 \sum_{l=1}^L \iint_{E_l} z_l \left(\gamma \frac{\partial u}{\partial v} \right) \delta \left(\gamma \frac{\partial u}{\partial v} \right) ds = \sum_{l=1}^L \delta V_l I_l \end{aligned} \quad (1.5.58)$$

On the l 'th electrode E_l ,

$$\delta \left(\gamma \frac{\partial u}{\partial v} \right) = \frac{1}{z_l} (\delta V_l - \delta u) \quad (1.5.59)$$

Combining (1.5.59) with the weak formulation (1.5.55) using $w = \delta u$ yields

$$\begin{aligned} & \iiint_{\Omega} \delta\gamma |\nabla u|^2 dx dy dz + 2 \iint_{\delta\Omega} \delta u \gamma \frac{\partial u}{\partial v} ds - \\ & - 2 \sum_{l=1}^L z_l \iint_{E_l} \frac{\partial u}{\partial v} \left(\gamma \frac{\partial u}{\partial v} \right) ds + 2 \sum_{l=1}^L \delta V_l \iint_{E_l} \left(\gamma \frac{\partial u}{\partial v} \right) ds = \sum_{l=1}^L \delta V_l I_l \end{aligned} \quad (1.5.60)$$

Noting that the second and third terms on the left hand side cancel, and the fourth is simply $2 \sum_{l=1}^L \delta V_l I_l$ then

$$\sum_{l=1}^L \delta V_l I_l = - \iiint_{\Omega} \delta\gamma |\nabla u|^2 dx dy dz \quad (1.5.61)$$

Equation (1.5.61) gives the total change in power. To get the change in voltage on a particular measuring electrode m when a current pattern I^d is driven into the volume, the associated ‘ measurement pattern potential ’ $u(I^m)$ must be calculated. Note the distinction between the current potential ’ $u(I^d)$ and the measurement potential ’ $u(I^m)$.

Applying the power perturbation formula (1.5.61) to $u(I^d) + u(I^m)$ and $u(I^d) - u(I^m)$ then subtracting gives the familiar formula

$$\delta V^{(d,m)} = - \iiint_{\Omega} \delta \gamma \nabla u(I^d) \nabla u(I^m) dx dy dz \quad (1.5.62)$$

where $V^{(d,m)}$ is the m ’th measurement under the d ’th current pattern. To calculate the Jacobian matrix one must choose a discretization of the conductivity. This can be taken either as piecewise constant, linear or even nonlinear on simplices on any other chosen polyhedral domain. Taking $\delta \gamma$ to be the characteristic function of the k ’th simplex, then for a fixed current pattern

$$J_{(d,m,k)} = \frac{\partial \delta V^{(d,m)}}{\partial \gamma_k} = - \iiint_{\Omega} \delta \gamma \nabla u(I^d) \nabla u(I^m) dx dy dz \quad (1.5.63)$$

From equation (1.5.63) the similarity in the definitions of the Jacobian and the global conductance matrix is obvious, as they both involve the integrals of the inner products of the gradients of the shape functions over each element. Every row of the Jacobian matrix corresponds to the sensitivity distribution inside the model with regards to the particular measurement and the current pattern.

1.5.5 Inverse Regularized Solution

In order to solve the inverse problem, I choose a direct method, which calculates an ‘exact’ regularized inverse of the Jacobian which is subsequently used to obtain the regularized solution in a single step.

In this Thesis, I focused on a static image modality in which a difference conductivity map between an homogeneous background and an inhomogeneous conductivity is reconstructed.

In static imaging starting from a known and usually homogeneous distribution x_p , a set of measurements V_p are gathered. In sequence, a perturbation δx occurs causing a new $x \neq x_p$ and consequently a $V \neq V_p$. Calculating J , the Jacobian based on x_p , the discrete form of the linearized forward problem used in static imaging becomes

$$J\delta x = \delta V \Leftrightarrow J(x - x_p) = V_p - V \quad (1.5.64)$$

in which only V is physically collected from the boundary of the volume and V_p is obtained by forward calculations,

$$J(x - x_p) = F(x_p) - V \quad (1.5.65)$$

In order to overcome the ill-conditioning of J i choose the algorithm known as NOSER, standing for Newton's One-Step Error Reconstructor because it reconstructs the conductivity distribution within the object by taking one step of Newton's method for solving nonlinear equation [108].

The advantage of using a one-step algorithm is that the Jacobian matrix for the uniform case can be calculated ahead and stored.

It uses the best conductivity approximation from the measured data as an initial guess and, consequently, many of the calculations involved in the reconstruction are analytical and the conductivity update is obtained by inverting the modified Hessian matrix or regularization matrix, that is taken to be the diagonal $diag(J^T J)$ guaranteeing positive definiteness of the Hessian [108].

One can solve (1.5.65) using the following regularized inverse,

$$x = x_p + (J^T W J + \lambda diag(J^T J))^{-1} J^T W (V - F(x_p)) \quad (1.5.66)$$

where $diag(J^T J)$ is a regularization matrix R , λ is a scalar regularization hyperparameter that controls the amount of regularization used to achieve a good reconstruction, and W models the

system noise. Since the noise is uncorrelated, one assumes that all measurements have equal noise variance, thus W becoming a multiple of the identity matrix.

A difficulty with experimental and clinical EIT reconstruction algorithms is the requirement to select the scalar hyperparameter. The most common method of hyperparameter selection is heuristic selection; researchers inspect reconstructions for a range of hyperparameter values and select the best one [102].

In [86], Cheney et al. give a full description of the algorithm in two-dimensions and in [103] Goble et al. extend it to three-dimensions.

This algorithm is included in the EIDORS package as developed by Andy Adler in [104].

Chapter 2

2. EIT system

2.1 EIT System Block Diagram

An *in vivo* impedance imaging system must consist firstly on an array of electrodes in a particular configuration which depends on a specific application, a data collection system which applies and records electrical potential, and secondly of an image reconstruction algorithm. Since the reconstructed image quality in impedance tomography greatly depends on electronic behavior of the EIT-instrumentation and the measurement accuracy, which is influenced by the phantom geometry, three main areas of development must be comprised in an EIT system as shown in figure 2: the electrode configuration and connection, data acquisition and data processing.

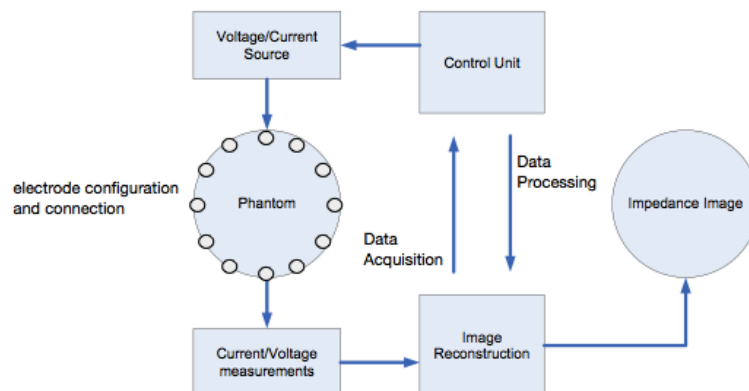


Figure 2: General Electrical Impedance Imaging system.

Our EIT system design is based on that of the Sheffield group of Baber and Brown [12], which produced the first published *in vivo* images in 1984. From that year up until now it represents the gold EIT system for medical applications as it is illustrated in figure 2.1. The block diagram shows 16 electrodes around the body and a multiplexing electronics to switch each driving pair electrodes and records potentials between pairs of electrodes.

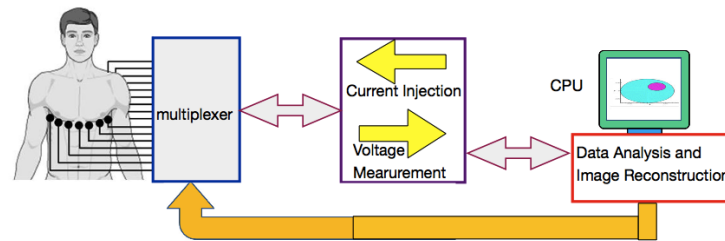


Figure 2.1: A medical EIT schematic, Sheffield group.

Our EIT system is completely shown in figure 2.2 and figure 2.3. It includes two parts, the hardware section and the image reconstruction software (EIDORS, available as a Matlab Toolbox). The hardware section contains five subparts: a computer with sufficient speed and memory to acquire the data, a matrix/multiplexer system to handle switching of the applied current and voltages, an electronic board switch matrix controller (the Vinculum V2D1P-64), the electrode array, the excitation source and the data collection system (the Lock-in amplifier Stanford Research Systems SR810, USA). Two simple serial communications on RS-232 allow the data exchange between PC and Vinculum for switching excitation and measurement pair, and between PC and Lock-in for acquiring data. The Lock-in amplifier plays an important role in the EIT system, since it is not only the data collection system, but also the excitation source (see fig.2.4).

More details about each component are well explained below.

The software section consists of reconstruction codes running on a PC with Windows 7 OS, Intel Pentium 4 processor (3.2 GHz), under the Matlab environment, integrated by the EIDORS toolbox.

This system was developed for use on experiment with phantom tank, filled with saline solution and different conductive objects (see chapter 3), with biological sample as a tissue section and to be representative of *in vivo* experiments on human tissues (all of the experiments are explained in chapter 4). Its results consist in an EIT image of the object where the EIT electrodes are placed.

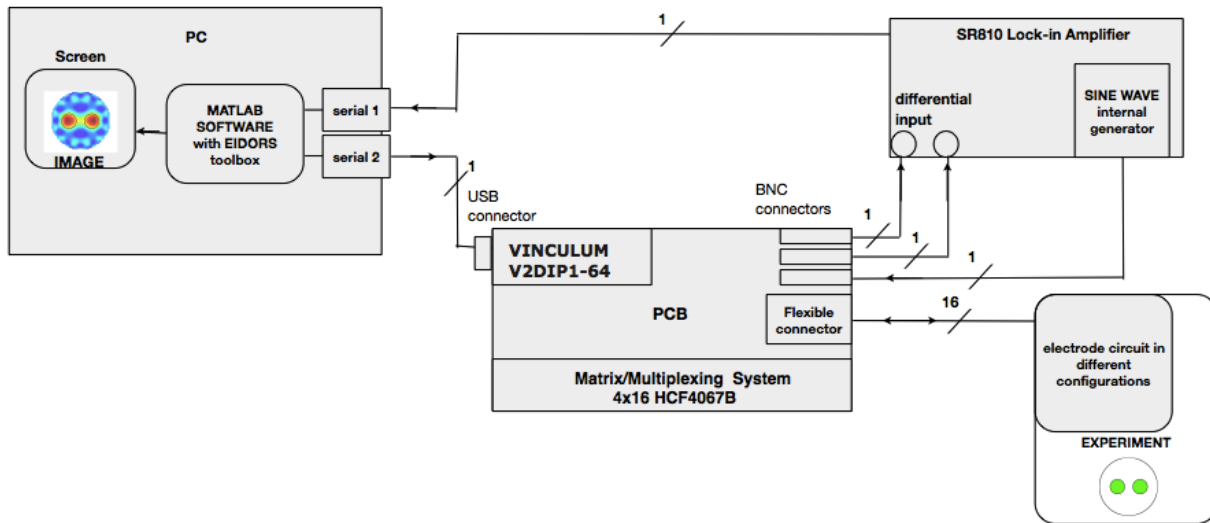


Figure 2.2: The structure of EIT system used.

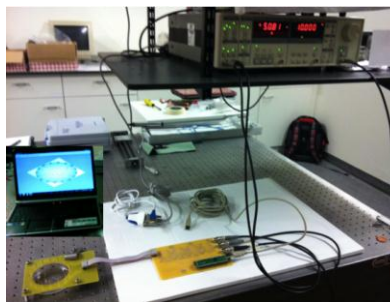


Figure 2.3: System in progress.

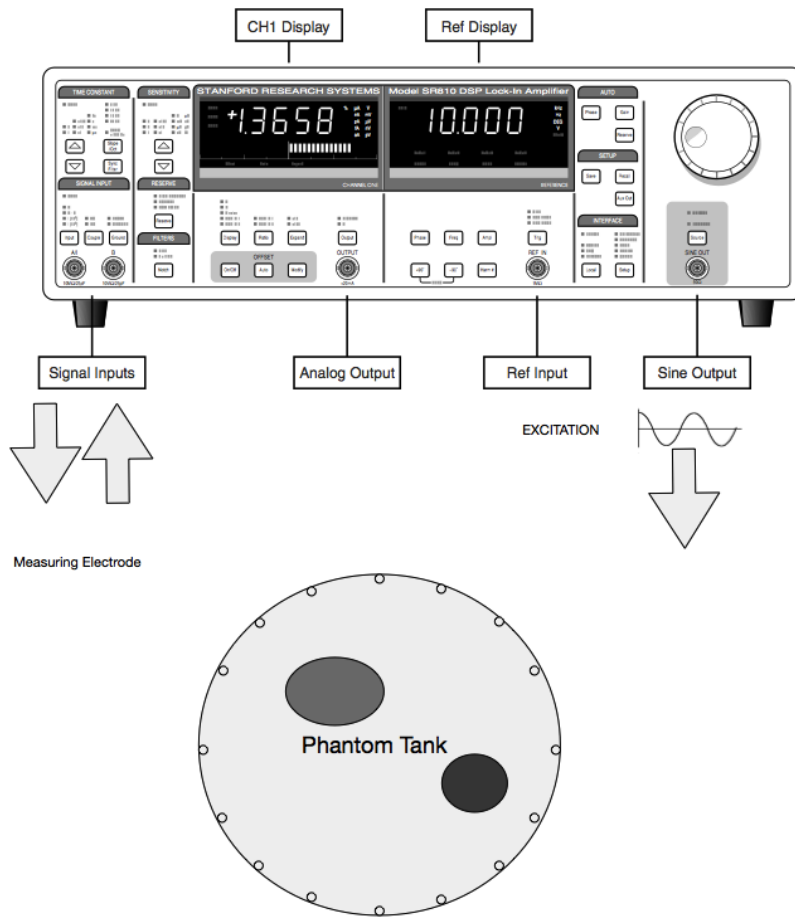


Figure 2.4: The Lock-in amplifier role in the measurement and excitation procedures.

It has two differential input each with input impedance $10\text{M}\Omega + 25\text{Pf}$, AC coupled and a sine-wave internal generator.

2.2 Hardware

The electrode connection is one of the greatest difficulties associated with EIT. In several laboratory scale experiments (Van Weereld et al. 2001, Polydorides 2002, and Molinari 2003) it has been found that accurate, consistent geometric connections are difficult to obtain. The electrode material is crucial to the behavior of the system, because each electrode in contact with

a saline solution develops an electrochemical interface. If the electrode material is reversible the chemical reaction can be reversed by reversing the electrical current. If the electrode material is irreversible this is referred to as a polarizable electrode: for examples silver-silver chloride electrodes are non-polarizable, gold and platinum electrodes are polarizable. The electrode design adopted for the experiments dealt with in this Thesis was a spring contact Be-Cu gold coated probes, figure 2.5a [105] with 1.05 mm diameter and contact impedance of 30 m Ω , thus allowing experiments with the phantom tank of centimetrical resolution, and a hard brass alloy wire, (figure 2.5b [113]) with 230 μ m diameter for experiments on human skin with micrometrical resolution. This design was selected due to the spring-loading feature that was useful in case of planarity loss. Furthermore these electrodes were easily soldered.

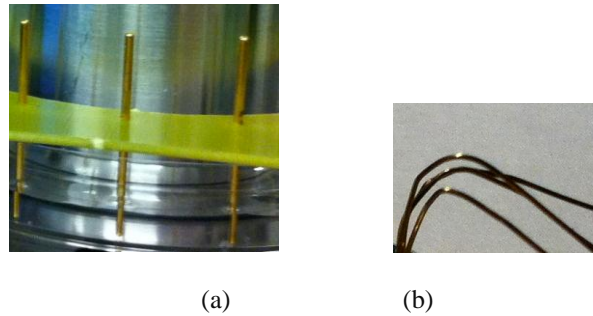


Figure 2.5: The structure of the electrodes.

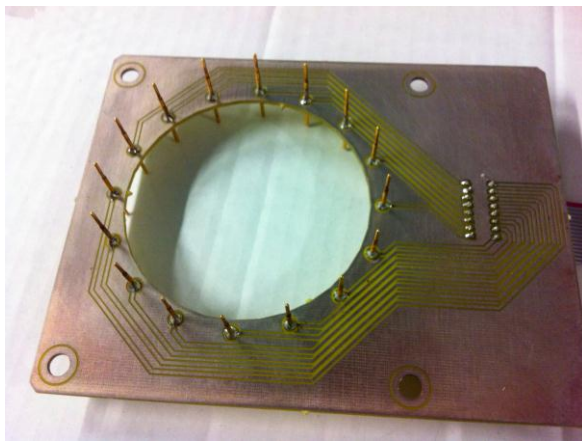
(a) Electrodes for the circular configuration, 105 mm diameter (b) Electrodes for the planar configuration, 230 μ m diameter.

The second aspect to take into consideration is the number and the electrodes configuration around the phantom tank or the tissue which one wishes to study.

In principle, with more electrodes, more independent measurements may be made and the reconstruction algorithm will be better constrained, resulting in higher confidence and resolution in the inferred conductivity distribution. However, the practical and electronic problems imposed by wiring is a great limitation. The adopted solution was to create a printed circuit in FR-4 (Flame Retardant woven glass reinforced epoxy resin), in which each electrode is soldered in

contact with its channel. This circuit design ensured consistent size and distribution of electrodes, while also creating a compact manageable system as compared to conventionally wired electrodes.

It has been studied [12] that finding the perfect electrode configuration is a difficult task because the total number of electrodes is restricted by the volume of the object and the size of the electrodes. I personally devised and implemented two different electrode configurations with 16 electrodes, considering the literature in order to obtain good images [22]. Firstly I created a configuration for two-dimensional applications. This was circular with the electrodes pressed on the phantom tank bottom and very close to its circumference (fig.2.6a, appendix A.1). It was a useful configuration for filling the tank with different conductive objects and saline solution, or with a tissue section of the same size of the tank. Secondly I thought about the best configuration for three dimensional experiments: for example scanning a human tissue as different layers in the skin. Many studies have been done so far for three dimensional applications and it is known that the best configuration would be an unique line of electrodes [117], but the software limitations imposed me to create a square matrix 4X4 of 16 electrodes close to each other 1mm from the center of the electrodes (figure 2.6b, appendix A.2). In this second configuration the electrodes distance was an important parameter for getting images of good resolution on 1mm of depth.



(a)



(b)

Figure 2.6: Printed Electrode Circuit.

- (a) Circular array configuration circuit in 1oz Cu, 1.6 mm thick, (b) Planar array configuration circuit in 1oz Cu, 1.6mm thick

The design was also simple enough to reduce or eliminate many problems, such as system leaks, short circuiting, and poor connections.

In this work, I adopted the tetrapolar method (four terminals) to measure the impedance. For each measurement, I needed two electrode pairs: the driving pair and the receiving pair. The driving electrode pair injects the current into the object and electrode pair measures the boundary voltage. The switch network with 4 multiplexer shown in figure 2.7 was divided into current switch and voltage switch. The current switch transmits the excitation current from current source to different driving pair. The voltage switch passes the measured voltage from every receiving pair to Lock-in amplifier where electrodes voltages are measured in differential way. The switch network was controlled by the Vinculum processor (FTDI, Glasgow, UK) integrated on the PCB (for details see appendix A.3).

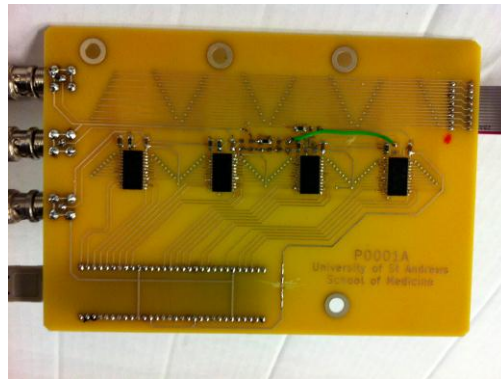


Figure 2.7: PCB, FR-4 1oz. Cu, Ag coated, 1.6 mm thick.

The switch matrix was arranged in a 4x16 (1-wire) configuration, meaning that 16 external channels are crossed with four internal channels, giving the ability to access 16 electrodes voltages from four input channels. 16 electrodes crossed with one current source, one ground, and two voltage measurement channels. I added the multiplexer datasheet [107], the Vinculum one in [109]. Three BNC connectors [110] allow the communication with two differential inputs and the sine-wave generator of the amplifier. A flexible connector [111] connects the PCB to the electrode circuit. I recommend to see appendix A.4 for a complete list of EIT components.

A sinusoid wave is produced by the Lock-in's signal generator at 10 KHz frequency.

A good current source has high output impedance and strong capability of noise rejection. The relationship between control voltage and output current should be linear. From those considerations I used a ballast resistance of 3.9 k Ω , which is substantially higher than the tissue impedance magnitude, to generate the current source for driving the driving pair.

I obtained the following measurement circuit shown in figure 2.8.

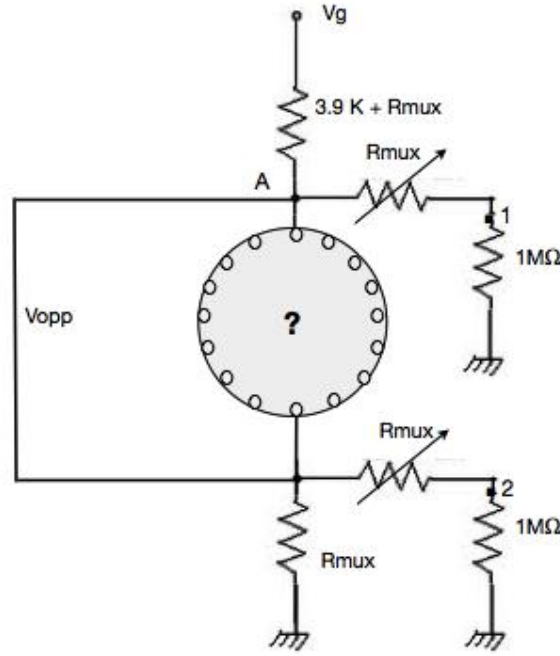


Figure 2.8: EIT Measurement circuit.

Where V_g is the control voltage obtained from the Lock-in amplifier. The R_{mux} represents the internal resistance of the multiplexers on the input and output lines. Those quantities are neglected on the output lines due to the high input impedance of the differential inputs A and B of the Lock-in amplifier. V_{opp} is the voltage between the opposite pair.

When a sample is not just a conductive object, but a real biological sample, its impedance will shift the phase of the current and will not change only its amplitude. The software needs

measurements and current values *in phase* with respect the internal reference of the Lock-in. One needs to calculate the module of the current from vectorial theory, as flows:

$$|I| = \frac{|V_g - V_{opp}|}{3.9 + 2 R_{mux}} \quad (2.2.1)$$

If d is the difference vector between V_g and V_{opp} , its form is

$$d = d_x \vec{i} + d_y \vec{j} \quad (2.2.2)$$

With d_x and d_y difference of the phase and quadrature components (X and Y) of V_g and V_{opp} :

$$d_x = X_{V_g} - X_{V_{opp}} \quad (2.2.3)$$

$$d_y = Y_{V_g} - Y_{V_{opp}} \quad (2.2.4)$$

Finally the numerator of 2.2.1 can be calculated as

$$|V_g - V_{opp}| = |d| = \sqrt{d_x^2 + d_y^2} \quad (2.2.5)$$

Observing than the phase of the voltage at the *node A*, which is the input node for the excitation of the sample, one can know the exact shift phase with respect the reference of the measurements V_{opp} taken between the input and output of the sample. Using that shift one needs to calculate the phase and quadrature components of the voltages required by the software for the reconstruction of the image.

The Stanford Research Systems (USA) SR810 Lock-In Amplifier is amongst the highest-performing lock-in amplifiers commercially available [112]. It uses digital signal processing (DSP) to replace the demodulators, output filters, and amplifiers found in conventional Lock-ins. Lock-in amplifiers use a technique known as phase-sensitive detection to single out the component of the signal at a specific reference frequency and phase. Noise signals, at frequencies other than the reference frequency, are rejected and do not affect the measurement. A Lock-in amplifier acts as a narrow band-pass filter around the reference signal frequency. The block diagram of lock-in amplifier is shown in figure 2.7.

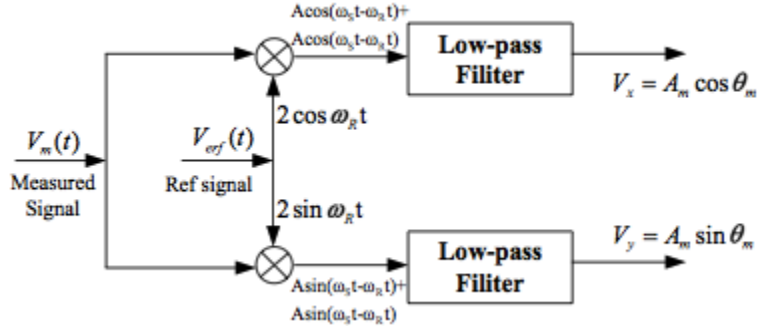


Figure 2.9: Block of Lock-in amplifier.

The internal oscillator behaves like a function generator (with variable sine output and a TTL sync) which is always phase-locked to the internal reference oscillator.

Lock-in amplifiers use a phase-locked loop (PLL) to generate the reference signal. An external reference signal is provided to the lock-in. The PLL in the lock-in amplifier locks the internal reference oscillator to this external reference, resulting in a reference sine wave with a fixed phase shift. A digital lock-in, such as the SR830, multiplies the signal with the reference sine waves digitally. It amplifies the signal and then multiplies it by the lock-in reference using a phase-sensitive detector or multiplier.

The amplified signal is converted to digital form using a 16-bit A/D converter sampling at 256 kHz. The A/D converter is preceded by a 102 kHz anti-aliasing filter to prevent higher frequency inputs from aliasing below 102 kHz.

The measured signal $V_m(t)$ and the reference signal $V_{ref}(t)$ are expressed as

$$V_m(t) = A \cos(\omega_m t + \theta_m) \quad (2.2.6)$$

$$V_{ref}(t) = 2 \cos(\omega_{ref} t) \quad (2.2.7)$$

The measured signal $V_m(t)$ is multiplied by reference signal $V_{ref}(t)$ and reference's quadrature, then the mixed signal is filtered by the low-pass filter. If the reference frequency ω_{ref} is equal to the measured frequency ω_m , the output signal V_X can be calculated as :

$$V_X = A \cos \theta_m \quad (2.2.8)$$

In the same way, the quadrature V_Y can be obtained as:

$$V_Y = A \sin \theta_m \quad (2.2.9)$$

According to these quantities, the amplitude and the phase of the signal V_m will be calculated:

$$A_m = \sqrt{V_X^2 + V_Y^2} \quad (2.2.10)$$

$$\theta_m = \tan^{-1} \frac{V_Y}{V_X} \quad (2.2.11)$$

The digital signal processor handles the task of output filtering. In particular, we have set low-pass time constants of 100 ms in every experiment.

In summary, I list below the specification for the EIT system:

Number of electrodes: 16

Drive frequency: 10 KHz

Excitation: 50-100 mV

Current through the sample: 12 – 14 μA

Data collection time: 30 min

Resolution: -circular array: 1.6 cm (reconstruction-dependent)
 -Planar array: 0.1 mm (reconstruction-dependent)

2.2.1 Parasitic Effects

In actual data acquisition process, the reliability of a single measurement is affected by noise. In most cases, the noise is caused by internal circuitry of the data acquisition system and is independent from the input signal. At the same time, as the most difference EIT images are reconstructed based on relative changes of boundary voltages, the smaller boundary voltages are, the more influence the noise will have on final images.

There is no doubt that stray capacitance is the major source of input error and that if both real and imaginary potential profiles are to be used then further reductions in these errors are necessary.

Four important considerations were made to improve the PCB system: since, in order to realize the advantages of using a four rather than a two electrode technique a well controlled current generator is required, I preferred a simple resistance rather than more complex sources; in addition the input impedance of the lock-in amplifier was sufficiently high to make electrode impedance insignificant. Rejection of common-mode interference (including DC) was obtained by a fully-differential measurement protocol. Before using the EIT system, preliminary experiments were necessary to understand the electric behavior of reference phantoms, such as a saline solution, with particular attention to electrode polarization, and the influence of amplitude and frequency excitation thereupon. Evaluating the electric behavior meant determining the electric impedance of the solution. I prepared for the experiments 15 ml of a saline solution (0.9% w/w NaCl) and I used it for filling a circular tank where there were 16 electrodes of the circular array configuration pressed on its bottom.

The impedance value was measured by employing the two-electrode method. In these experiments I measured the voltage between two opposite electrodes kept on the circumference of the phantom and connected to an alternating excitation and a Resistance R of $0.982\text{ K}\Omega$, the voltage that appears on both ends of the resistor R , and the input voltage on the first electrode (see fig.2.10 a).

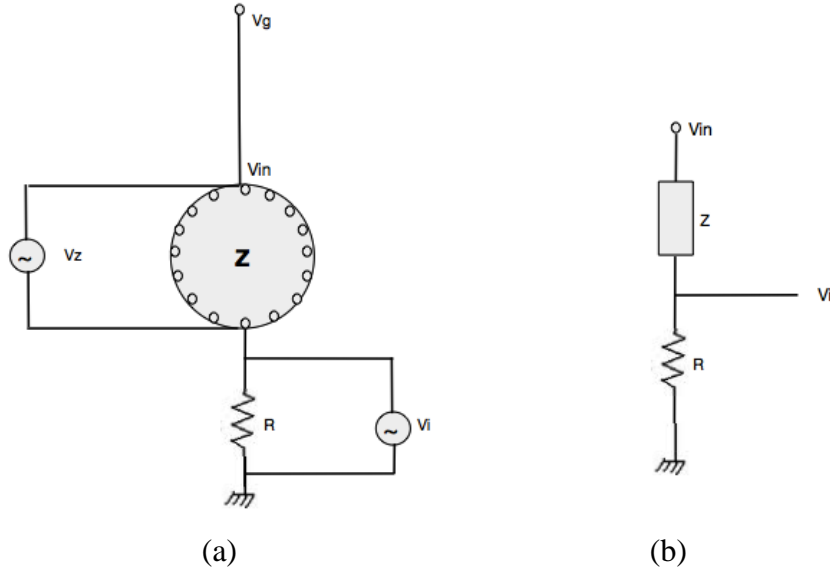


Figure 2.10: Preliminary experiment on a saline solution.

(a) Measurement system, (b) Equivalent circuit.

The equivalent circuit in figure 2.10 b was used for the impedance calculation. Considering that the resistor was connected in series to the phantom, one can solve the voltage divider as

$$V_i = V_{in} \frac{R}{R+z} \quad (2.2.12)$$

One can obtain the impedance knowing the in phase and quadrature components of V_i (V_{iF} and V_{iQ})

$$Re(z) + j Imm(z) = \frac{V_{in}R (V_{iF} - jV_{iQ})}{V_{iF}^2 + V_{iQ}^2} - R \quad (2.2.13)$$

Solving 2.2.13 one can calculate the real and the imaginary parts of the impedance as

$$Re(z) = \frac{R (V_{in}V_{iF} - (V_{iF}^2 + V_{iQ}^2))}{V_{iF}^2 + V_{iQ}^2} \Omega \quad (2.2.14)$$

$$Imm(z) = -\frac{RV_{in}V_{iQ}}{V_{iF}^2 + V_{iQ}^2} \Omega \quad (2.2.15)$$

These experiments were conducted with different V_g and frequency values reported in figure 2.11.

Amplitude	frequency
1V	100 KHz
800-600 mV	82-68-56 KHz
300 mV	47-39-33 KHz
200 mV	27-22 KHz
100-80mV	18-12-10 KHz
60-30mV	1 KHz
20mV	100-10 Hz

Figure 2.11: Excitation V_g : amplitude and frequency.

The acquisition code for the impedance measurement is listed in appendix B.1.

In figures below I plotted the real and imaginary components of the calculated impedance for each tabulated V_g , and the phase of the impedance evaluated as

$$Phase(z) = atang \left(\frac{Imm(z)}{Re(z)} \right) \quad (2.2.16)$$

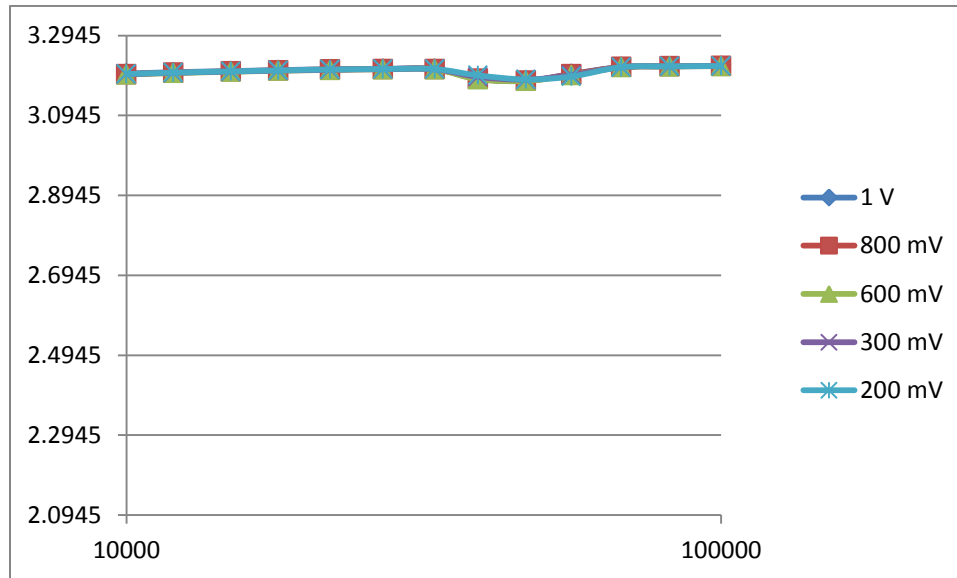


Figure 2.12: Logarithm of the Real component of impedance in frequency and for excitation V_g of 1 V, and 800-600-300-200 mV.

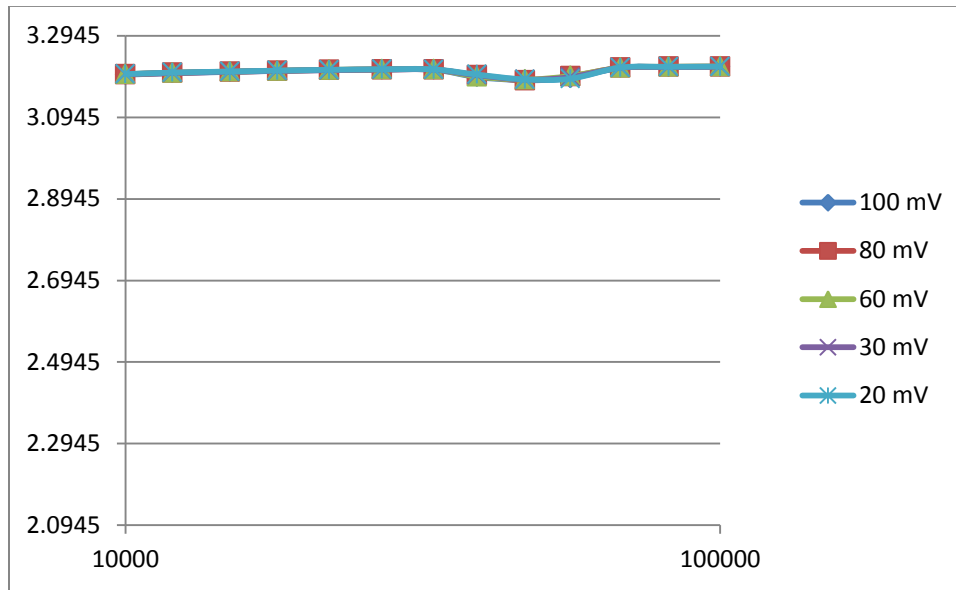


Figure 2.13: Logarithm of the Real component of impedance in frequency and for excitation V_g of 100-80-60-30-20 mV.

The logarithm of the real component of the impedance shows a constant behavior with the frequency and its values are comprised between 3.29 and 3.09 for each experiment, with an insignificant decrease at 47 KHz. That means the resistive part of the impedance is constant with the frequency and it is evaluated to be about 1.6 K Ω .

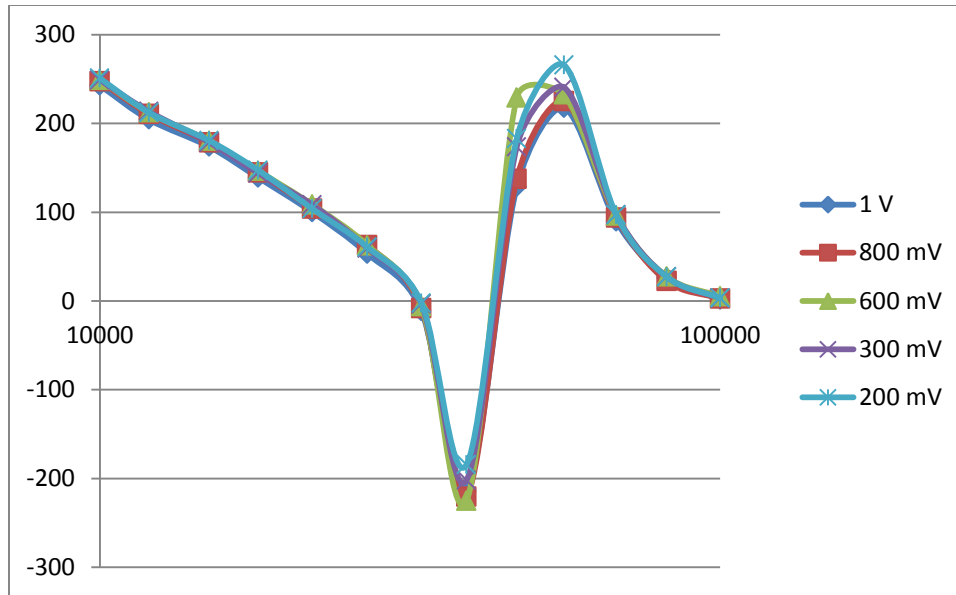


Figure 2.14: Imaginary component of impedance in frequency and for excitation V_g of 1 V, and 800-600-300-200 mV.

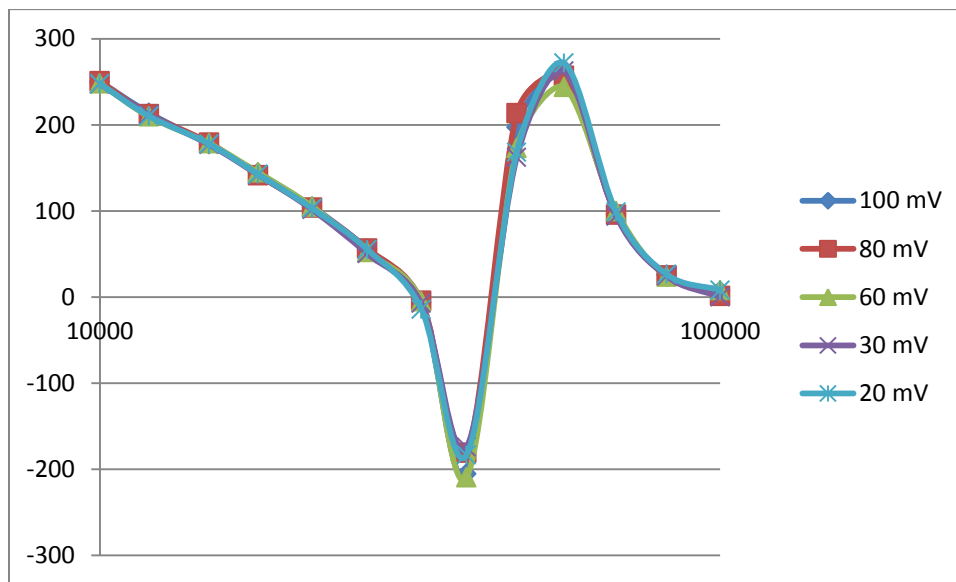


Figure 2.15: Imaginary component of impedance in frequency and for excitation V_g of 100-80-60-30-20 mV.

The imaginary part has predominantly a positive behavior with extreme values of resonance at 39 and 56 KHz and inversion of the graphic at 47 KHz. The phenomenon of resonance attributed to parasitic capacitance and inductance of the cables. I could presume a capacitive behavior of the impedance on the negative resonance of the graphic and an inductive behavior on the positive resonance.

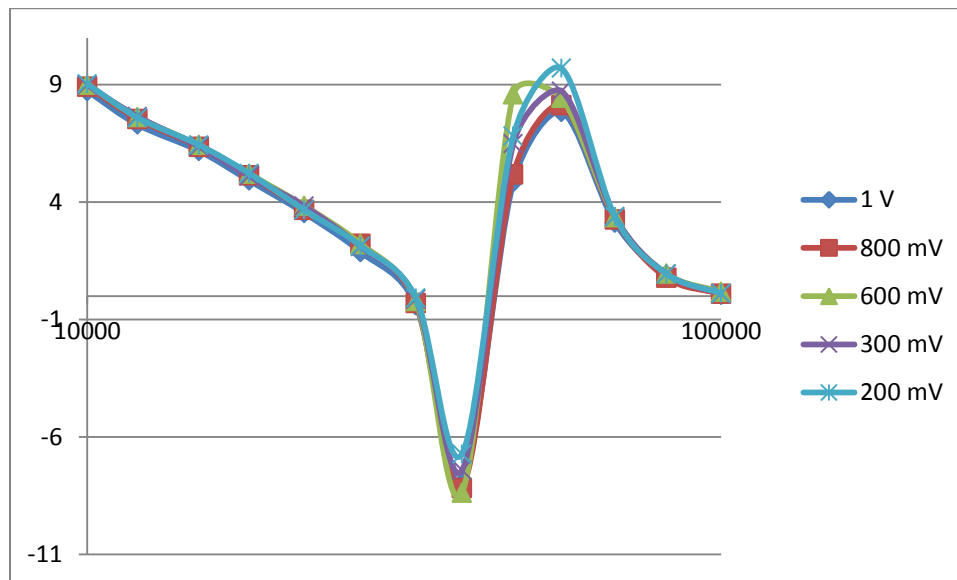


Figure 2.16: Phase of impedance in frequency and for excitation V_g of 1 V, and 800-600-300-200 mV.

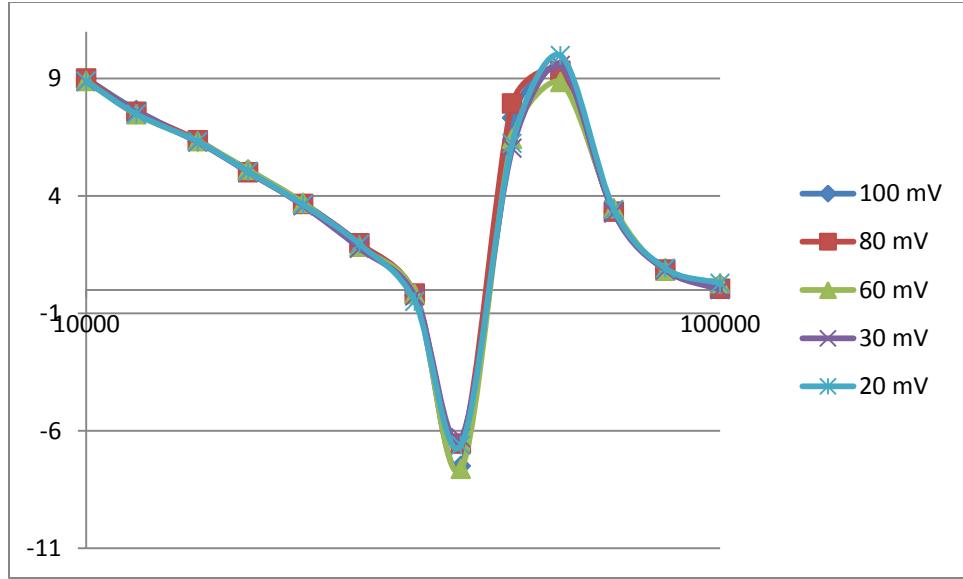


Figure 2.17: Phase of impedance in frequency and for excitation V_g of 100-80-60-30-20 mV.

Observing the behavior of the phase of the impedance with the frequency, one can notice that is the same of the imaginary part, but one can extract more information about the resonance: as supposed, the phase is negative over the frequency 39 KHz defining a prevailing capacitive component, and it is positive over 56 KHz defining an inductive component. Finally, the phase angle has different values with the frequency. They range between 9 degrees and -9 degrees, which is a value that falls within our tolerance, which means that voltage and electric current through the phantom are *in phase* and that is typical for a resistive sample, as it should be for a saline solution. Again the presence of different values comes from the parasitic effects of the cables, and neglecting it one can conclude that the solution is a resistive sample for each considered frequency.

Furthermore it was possible to evaluate the amplitude of the electric current passed through the phantom as

$$I = \frac{V_i}{R} \quad A \quad (2.2.17)$$

and easily comprehend in what frequency condition the polarization effect could introduce errors in the measurement (see fig.2.18 and 2.19).

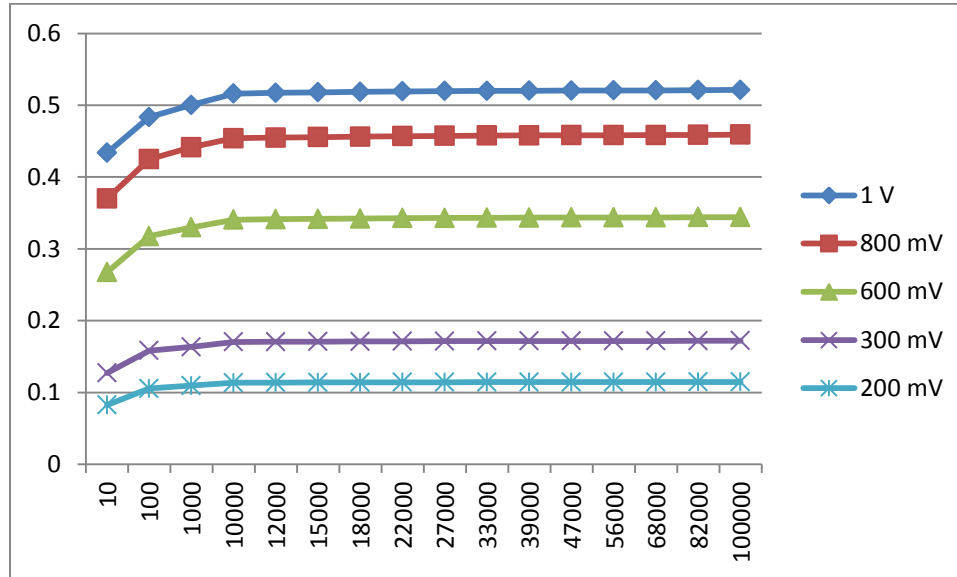


Figure 2.18: Electric current through the phantom in frequency and for excitation V_g of 1 V, and 800-600-300-200 mV.

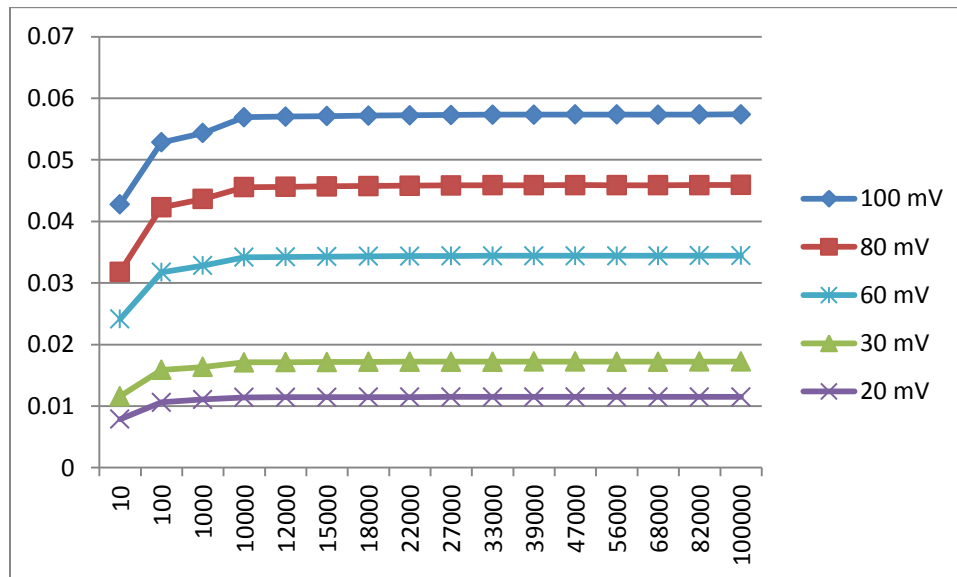


Figure 2.19: Electric current through the phantom in frequency and for excitation V_g of 100-80-60-30-20 mV.

These plots show how the electric current linearly changes with the imposed excitation. Its value is constant with the frequency for almost all measurements, but it rapidly decreases at low frequency due to electrode polarization. In fact it is known that ions over a low frequency condition can not move, but just migrate and stop on the electrodes surface. They become an obstacle for the electric current flow.

Those considerations allowed me to determine the right frequency for avoiding the polarization effects and for assuring a known electric current flow inside the phantom. Furthermore by eliminating the effects of the cable presence, one can obtain resistive component of the measurement for processing and elaborating images from those.

Furthermore a low-pass time constant of the Lock-in 100 ms, allowed stable measurements and repeatable results.

Different considerations were made after assembling the complete EIT system. Principally it was important to evaluate the accuracy of the acquired data.

Considering the distribution of the voltages at adjacent electrodes (figure 2.20), due to the opposite stimulation method, negative measurements are placed on the right side of the phantom and positive measurements are on the left one.

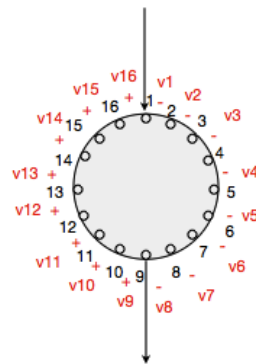


Figure 2.20: Voltage distribution with the first opposite stimulation. The voltages on the left of the phantom thank are negative, and those on the right are positive.

Ideally differential voltages measured on the excitation electrodes 1st and 9th, are equal to the sum of voltages distribution as follows:

$$V_1 - V_9 = \sum_{n=1}^8 v_n \quad (2.2.18)$$

$$V_9 - V_1 = \sum_{n=9}^{15} v_n \quad (2.2.19)$$

For each acquisition it was considered to verify the 2.2.18 and 2.2.19 conditions, acquiring the difference, successively named Vopposite and the difference, named Vopposite_inverse.

It was always found that conditions were not verified, instead it was present a systematic error amounting to 10%.

2.2.2 Acquisition Strategy

The EIT data collection system uses 16 electrodes which are addressed through four multiplexers. A sinusoid wave produced by the Lock-in's signal generator is fed to 2 multiplexers, which allow the current source to be applied to one pair of electrodes at time. The other 2 multiplexers are responsible for the differential acquisition on electrodes voltages.

The issue of data acquisition in EIT has been addressed by several researchers, but the optimum order and procedure in collecting data is not standardized. In this Thesis the exact order and procedure for the EIT system has been dictated by the reconstruction software.

In the literature [1] one can find that in adjacent, cross and opposite drive pattern, although adjacent voltage measurement method is used in every measurement mode, the ways how to set the acquisition strategy are different and they cause different measurements formats and special EIT system for different pattern. In this Thesis I used the opposite method, with voltage detection on all adjacent electrodes. The current electrodes were selected to be diametrically opposed to each other across the object under study to maximize the sensitivity of the EIT system to impedance imaging. For any driven pattern, 16 measurement can be obtained in each excitation, that is, boundary voltage between electrodes 16-1, 1-2, ..., 15-16. A numbering scheme was chosen for the electrode configurations used for the experiments, in order to obtaining a tetrapolar approach with external current electrodes and inside voltage electrodes. In

figure 2.21 a, b the electrode numeration for the circular and planar electrode array configurations and the sequence of measurements used to collect imaging data from 16 electrodes are shown.

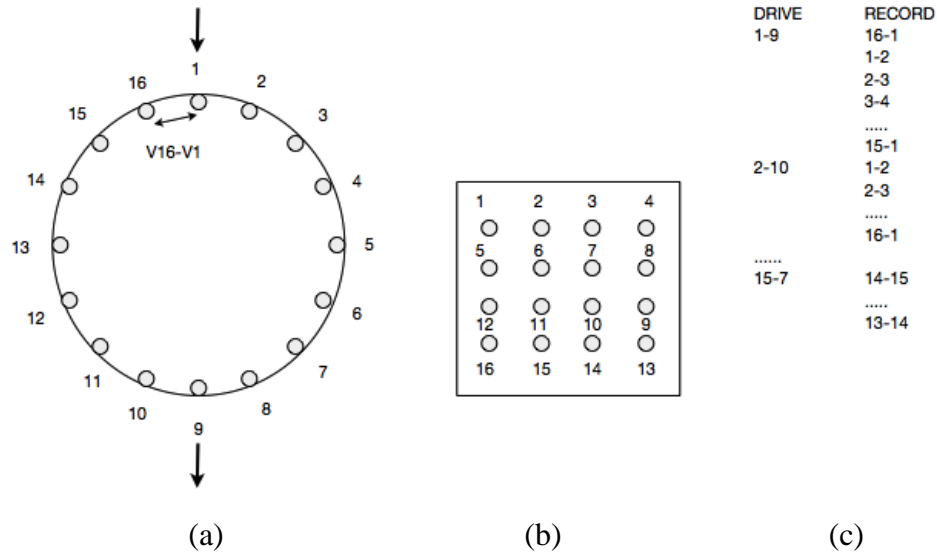


Figure 2.21: The excitation and measurement sequence in the EIT system.

(a) Electrode numeration in circular array, (b) Electrode numeration in planar array, (c) The data set used, it consists of 256 data.

The Acquisition code in appendix B.4 is a Matlab file for collecting 256 data with the sequence as described. In order to pilot the Vinculum for activating the multiplexer channels a 5-bits hexadecimal string is required, in which the first two bits are for the input and output excitation, the third and the fourth bits are for the differential voltages and the last bit is the terminator.

The code shown in figure 2.22 establishes a connection between the computer and the Vinculum with serial-port COM4, a connection between the computer and the Lock-in with serial-port COM3, uses a *while* condition for the acquisition and the storage of the dataset for the image (Vadjacent) and some other necessary data for finding eventual crosstalks (Vopposite and Vopposite_inverse) and to analyze the phase shift of the potential before and after gets in the

sample (VnodeA). Each measurement is acquired with its phase and quadrature component, phase and module.

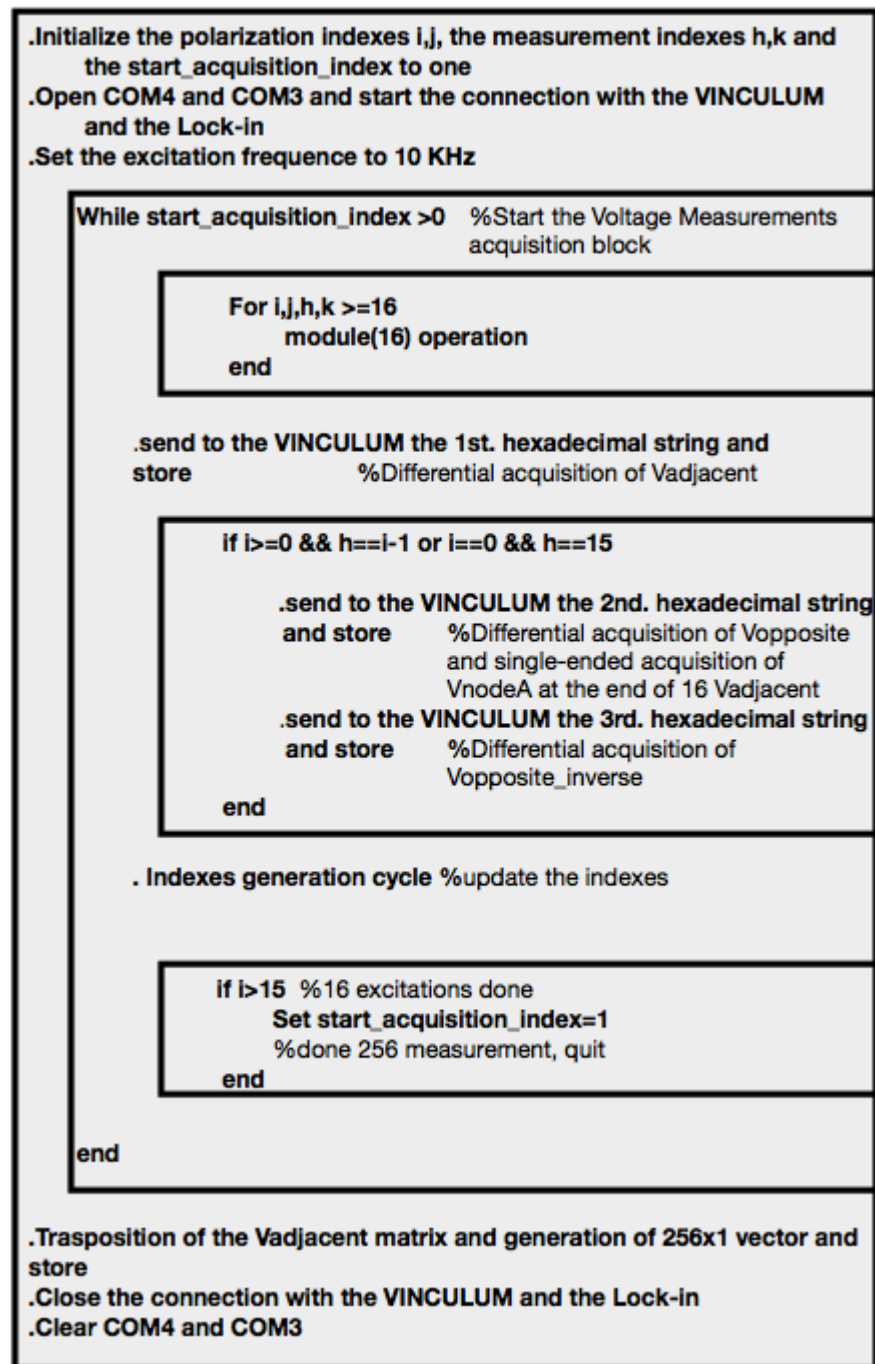


Figure 2.22: Simplified code structure of the Acquisition Code in appendix B.4. The code includes the frequency setting for sine wave generator, while its Amplitude is settled from the front panel of the amplifier. The measurement of VnodeA uses the same string of Vopposite . It is a single-ended measurement and requires typing the single-ended button from the Lock-in.

The right turning on of the channels is obtained with the indexes generation cycle inside the *while* condition (see fig.2.23), which is designed to update the hexadecimal number of the stimulation indexes i, j and measurement indexes h, k . In the block diagram, the yellow blocks shift the measurements channels obtaining the adjacent measurement acquisition, while the red one shifts the excitation channels obtaining the opposite excitation changing.

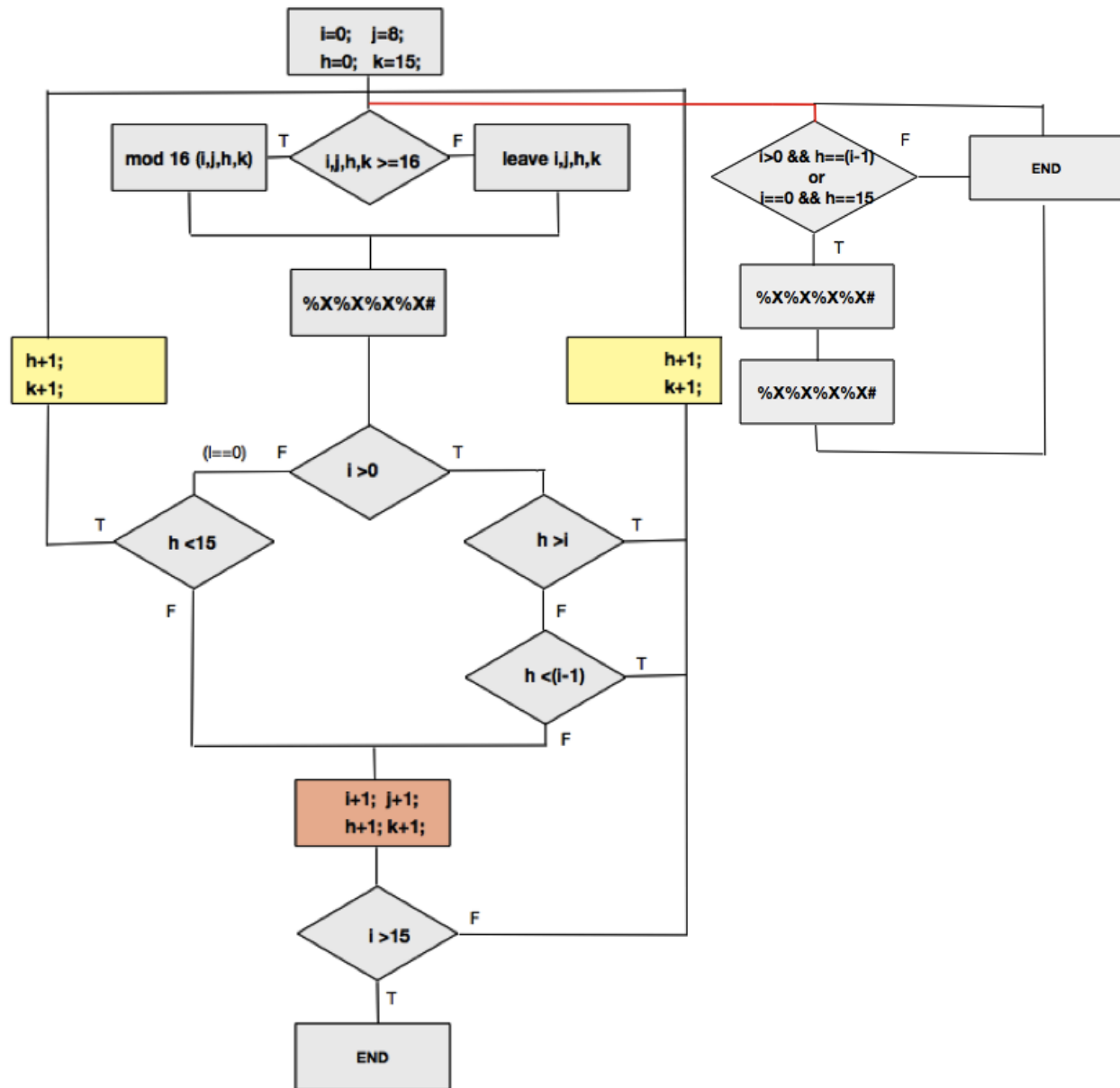


Figure 2.23: Indexes generation cycle. The red line underlines the subcycle for Vopposite, Vopposite_inverse and VnodeA acquisitions.

Finally, it is important to give the software the difference voltages acquired in the right format. EIDORS requires a unique vector of 256 data, in which for every excitation pair the first measurement must be the 16-1 pair. The strategy for obtaining the vector was acquiring as first data the electrodes pair before that in which the current gets in, store it as element of the diagonal of a 16X16 matrix. The obtained matrix has on the first column the 16-1 electrode pair. After a simple transposition one can to pill up the columns each under each other to obtain a unique vector (fig.2.24).

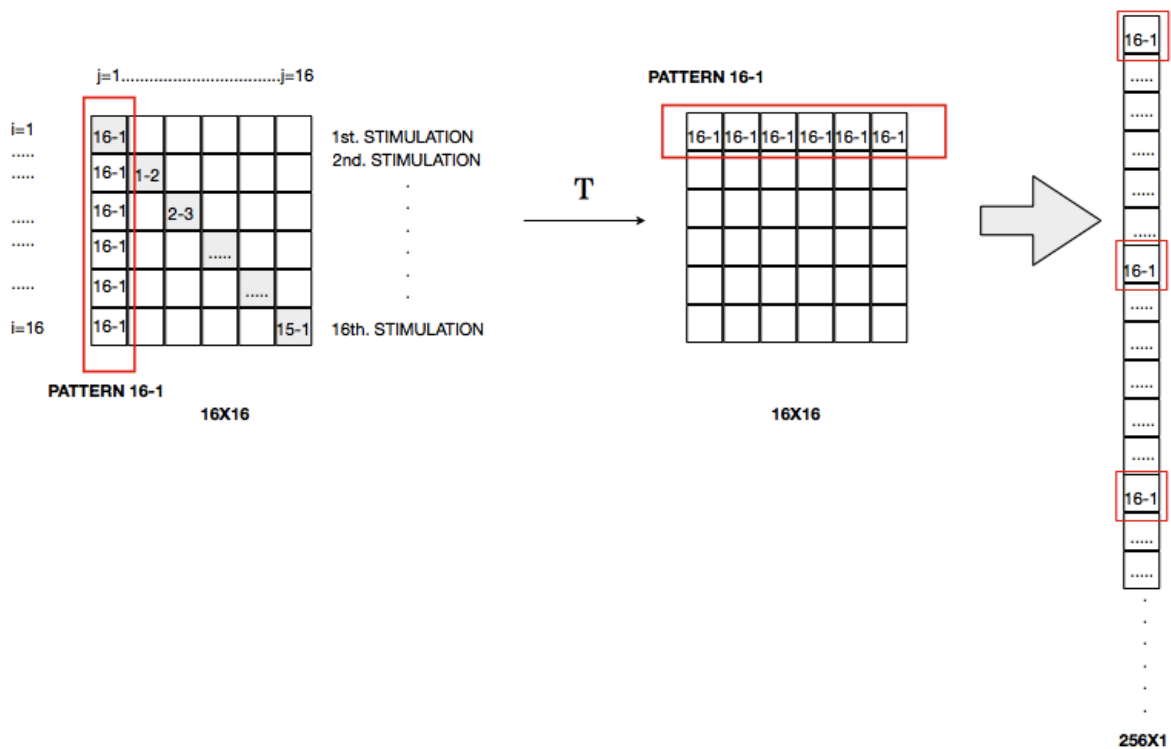


Figure 2.24: Generation of 256X1 vector for EIDORS processing.

2.3 Software

The data processing of this Thesis was accomplished using the EIDORS V.3.4 toolkit. The toolkit was chosen as it provides a framework for a solution to the challenges in solving an EIT inversion problem, which is very intensive computationally. The package is equipped with some mesh generators, several standardized EIT measurement protocol customizations, a graphical output, and supports two-dimensional and three-dimensional EIT systems.

I describe quickly the key features of this software taken from its manual [114]. The EIDORS software package works on four primary objects: data, image, forward model and inverse model. The most complex EIDORS object is the forward model, which is designed to represent, using a finite-element method (FEM), electrode positions and properties, and stimulation patterns, as well as the pointers to functions to describe the forward problem on this model. The forward model contains three function pointers to allow solution of the forward problem, solver, jacobian matrix. Each field contains the function name (as a string) or a function pointer to calculate these quantities. In each case, these quantities are solved using the utility functions 'fwd_solve', 'calc_jacobian'.

An EIDORS data object represents a frame of measurement or simulated data.

The inverse model object groups information necessary to allow reconstruction of images. I defined images in differential modality, which calculates an image based on the difference between two data objects. The provided functions are based on regularized image reconstruction algorithms and require an *image prior* and a choice of a convergence *hyperparameter*. The latter is specified in the hyperparameter field. The image prior used is the NOSER [reference] function for the calculation of the regularization parameter, defined as the diagonal. The EIDORS image object expresses the reconstructed or simulated conductivity values and its field 'elem_data' is the value of each of the image elements in the finite-element model (in the field 'fwd_model').

The complete Matlab programs utilizing the EIDORS functions are listed in appendix C.2, where every data processing code belongs to the category named 'Reconstructions', meaning those codes from which the image of the experiment is obtained.

Shown below in figure 2.25 is a simplified code structure for the data processing. The first step in solving for the internal conductivity distribution was to create a finite element model of the experiment. In order to obtain accurate reconstructed images it is important that information

regarding the geometry of the phantom or the human body part is included in the forward problem. A Finite Element Model (FEM) was designed based on the geometry acquired from EIT data using NETGEN [127] using the functions 'ng_mk_cyl_models' which needs of the height and radius of the domain, number of electrodes for planes (only 1 plane for the selected configuration) and radius of the electrodes, figure 2.26-2.27-2.28. With these finite element models and a set current it is possible reproduce the experiment. The opposite stimulation and the adjacent acquisition is simulated by the function 'mk_stim_pattern' together to the definition of the current. The forward problem is not solved, but just configured to obtain apposite matrixes in which one can store the voltage acquisitions. The next step was to load the real data and solve the inverse problem using the NOSER algorithm in both two and three dimensional cases. The inverse solver is recalled by the function 'inv_solve' together to the inverse model, and the two datasets needed in difference imaging.

Create Electrode Model	%Create simple 16 electrode finite element model with homogeneous conductivity (background)
Set Parameters for the Forward EIDORS object and Create the structures for real data	%The inverse problem needs a complete definition of the Forward field and the matrix for loading voltage measurements
Load real data	%Load real voltage measurements (two datasets)
Create Inverse Electrode Model	%the same of Electrode Model, but if the problem is two-dimensional this Model has less elements
Solve Inverse Problem	%Solve for conductivity distribution using the Inverse Electrode Model, two voltages measurement

Figure 2.25: Simplified code structure for Reconstruction codes in appendix C.2.

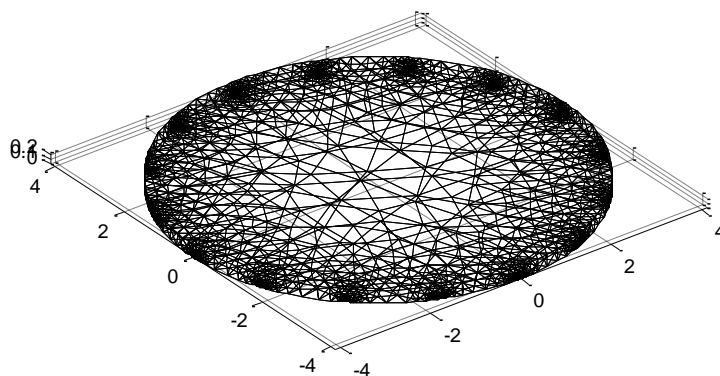


Figure 2.26: Finite Element Mesh and electrodes. Mesh with 8716 elements of the phantom (height 0.264 cm , radius 4.12 cm), from the EIDORS code in appendix C.2.2.

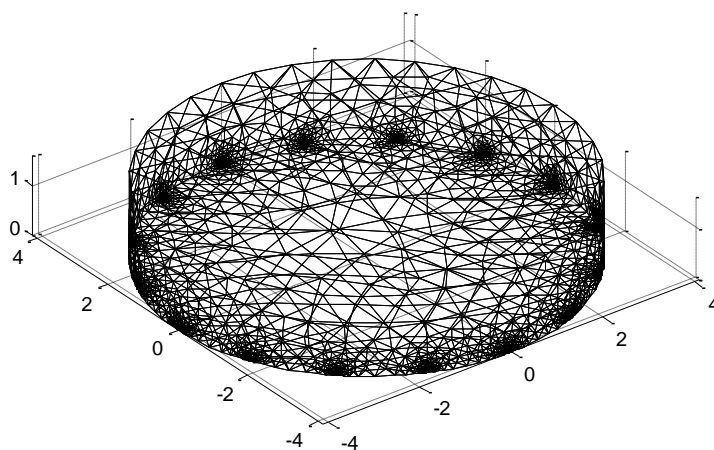


Figure 2.27: Finite Element Mesh and electrodes. Mesh with 9000 elements of a Tissue Section (height 1.6 cm, radius 4.12 cm), from the EIDORS code in appendix C.2.3.

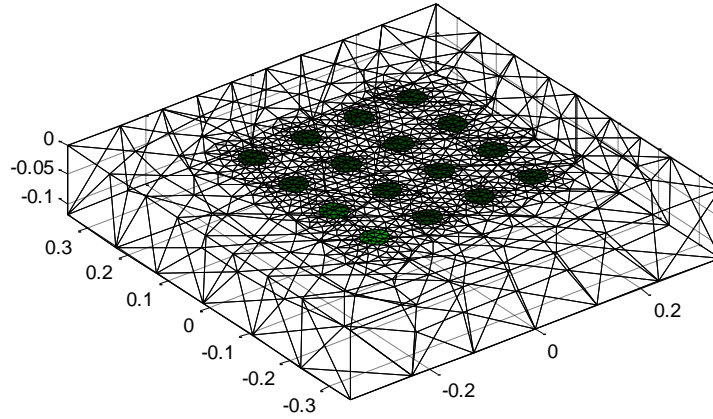


Figure 2.28: Simplified model of the skin as a rectangular parallelepiped. Mesh with 8044 elements of the Human Skin (height 1.2mm, wide 4mm), from the EIDORS code in appendix C.2.4.

It was also necessary to prepare any simulations to test the effective precision of the acquired voltages and the effective truthfulness of the reconstruction algorithm. In these simulations (appendix C.1) the forward solver is implemented on order to obtain the two datasets without and with inhomogeneous inclusions. Figure 2.29 shows the simplified code structure. The forward and the inverse problems were solved using the standard Polydorides methods described in chapter 1.

Create Electrode Model	%Create simple 16 electrode finite element model with homogeneous conductivity (background)
Solve Forward Problem	%Solve for simulated homogeneous voltages
Add inhomogeneity	%Add objects with different conductivity
Solve Forward Problem	%Solve for simulated inhomogeneous voltages
Create Inverse Electrode Model	%the same of Electrode Model, but if the problem is two-dimensional this Model has less elements
Solve Inverse Problem	%Solve for conductivity distribution using the Inverse Electrode Model, two simulated voltages (homogeneous and inhomogeneous)

Figure 2.29: Simplified code structure for Simulation codes in appendix C.1.

The final images reconstructed in EIDORS are shown later in apposite chapters regarding experiments with different objects and biological samples.

2.4 PCB Calibration

Observing the measurement circuit in figure2.8, the right knowledge of the R_{mux} involved in the measurement procedure and in the calculation of the current through the sample in equation 2.2.1 was necessary.

Fundamental step was to reconstruct the actual voltage applied to the circuit, shown as the node A in the measurement circuit, in order to solve the voltage divider shown in figure 2.30. In order to perform such determination, a short circuit of the measurement electrodes was performed using a saturated saline solution.

One can read the acquisition code for the experiment in appendix B.2. The Matlab code obtains only 16 adjacent differential voltages on excitation electrodes.

Solving the equation for R_{mux} brought the results of 0.132 K Ω for each multiplexers assuming that the amplitude of was 50 mV at 10 KHz of frequency. The electric current calculated by equation 2.2.1 was 12.008.

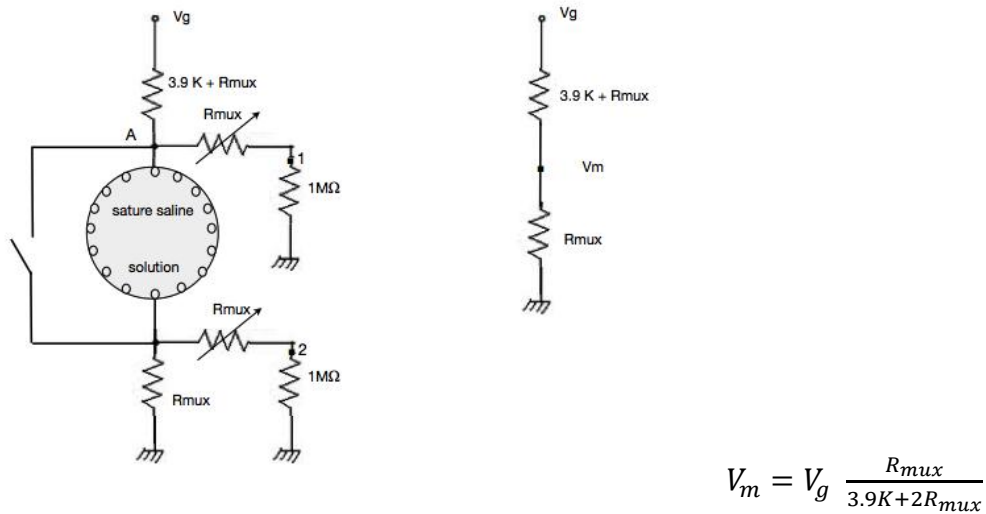


Figure 2.30: Measurement circuit in short-circuit and equivalent circuit and the equation for measured tension.

Finally to understand if the EIT system was initially able to measure a simple resistor of 0.982 K Ω I did an experiment with electrodes in series with the resistor. I obtained a stable measurement on each channels (fig.2.31), using the same data acquisition code of the short-circuit experiment.

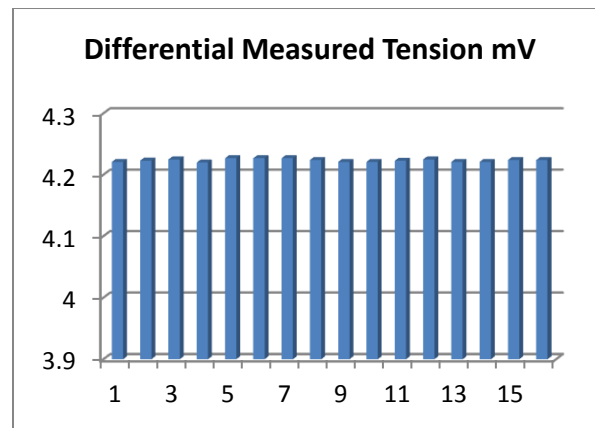


Figure 2.31: Measured tensions on 16 electrodes in series with the resistance.

Despite the stability of the measurement, it has been seen that the accuracy is low, reading 4.22 mV instead of 11.24 mV ideally calculated. These errors were induced by the crosstalks.

2.5 Forward Problem Simulation

Forward Problem is the basis of EIT and it is essentially to be solved to calculate the boundary potential for estimating the conductivity update in inverse Problem. In this thesis by studying the forward problem I could be able to detect the reliability of EIDORS in solving the boundary voltage distribution, simulating an experiment with saline solution of known conductivity as sample. The goal was to assure that the order of magnitude of the simulated and real voltages were acceptably close.

I conducted the real experiment using a plastic tank filled up with 0.9% saline solution and the circular array of electrodes kept to the bottom of the tank. The conductivity of saline solution was 14.4 mS/cm. The sinusoidal tension V_g coming from the sine wave lock-in generator was 50 mV and the electric current on stimulation electrodes was valued as the V_g / impedance of electrodes ratio. The impedance of electrode was 30 m Ω and the electric current calculated was 1.6 mA. I performed the voltages acquisitions by hand, moving the probes on electrodes in adjacent way according with the acquisition code in appendix B.3.1. I recorded only the first 16 adjacent voltages because I thought it was sufficient measuring only a cycle of boundary tensions, since their value should have been constant in each measurement cycle.

Meanwhile I performed a code for a simulation of the experiment to obtain simulated values to compare with the measured ones. In this direction the EIT-forward problem was solved in file code in appendix C.1.1. The forward solver, using Finite Element Method (FEM), discretizes the medium under analysis into a finite number of elements as that shown in figure 2.2.6. For reproducing the real experiment the forward problem is solved with injected electric current and homogeneous conductivity of the medium of 14.44 mS/cm. Then the forward solver is used to solve the governing equation for calculating the surface potential. It gives 256 simulated boundary tension totally plotted below in figure 2.32.

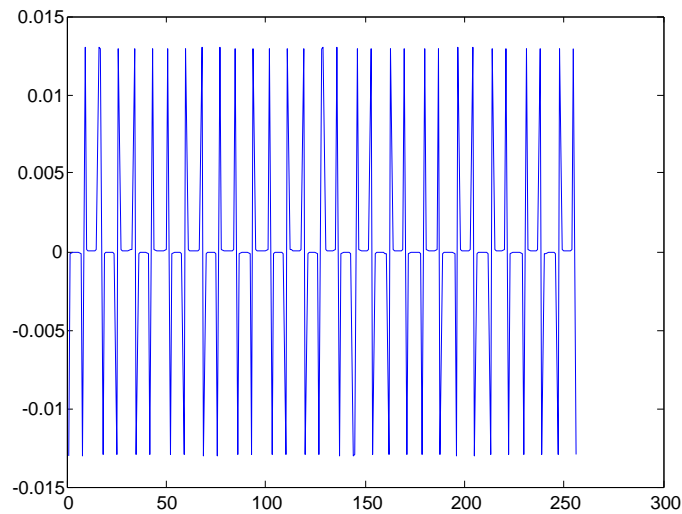


Figure 2.32: Simulated boundary voltages generated by file code in appendix B.3.1.

As one can see the graphic is quasi-periodic and the values repeats themselves in each cycle of 16 data.

For a better comprehension of these 256 simulated value and this previous graphic, I analyzed only the first 16 data of them, plotted in figure 2.33, since they are the first cycle of measurement when stimulation is applied on the first couple of electrode 1 and 9, and then they were compared with the measured data, plotted in figure 2.34.

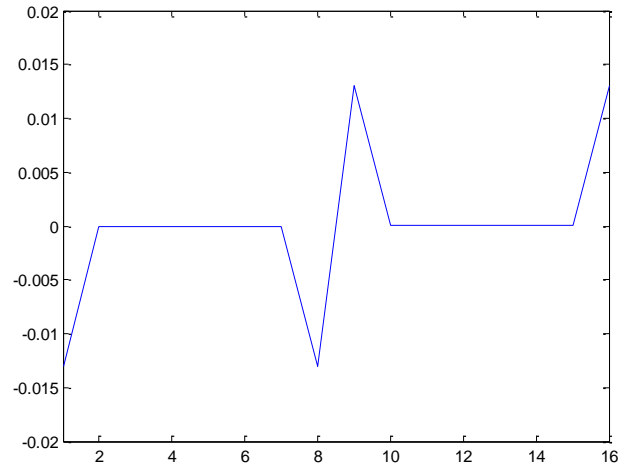


Figure 2.33: First 16 boundary voltages generated by code in appendix C.1.1.

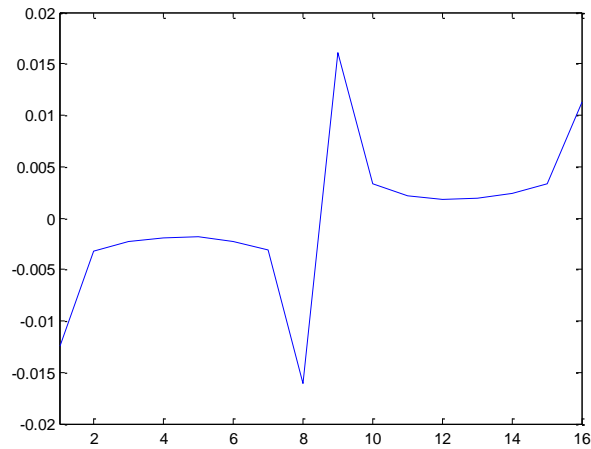


Figure 2.34: Measured voltages acquired by code in appendix B.3.1.

These graphics go in a very similar way with the measurements and the deviation between the potential data generated through the forward solver and that provide by real measurement procedure was only 0.08% to 0.20%. The deviation was mainly due to the measurements taken inside the electrodes excitation 1 and 9. In fact from measurements 2 to 7 and 10-15 the forward solver produces differential voltages of zero value, as if the excitation applied between electrodes

1 and 9 was ideally distributed in straight way with direction from 1 to 9, generating boundary differential voltages only on electrodes adjacent to those of excitation.

Finally, the deviation was so negligible that the software was accepted as accurate for our EIT application.

2.6 Homogeneous Image Reconstruction: Saline Solution

Fundamental step was to understand the ability of EIDORS in solving the inverse problem and obtaining the conductivity map. In principle I wanted to test the software, before using it in more complex experiments with different conductivity objects for obtaining contrast images, in a homogeneous conductivity experiment. I tested for the first time the algorithm chosen for solving the inverse problem in code listed in appendix C.1.1. The code was devised to fill the inverse solver's fields with an inverse model, and two sets of data. It implements the forward solver for calculating the boundary simulated voltages, the first data set used, as treated on previous paragraph (FEM with 8716 elements, 256 simulated differential tensions shown in figure 2.35).

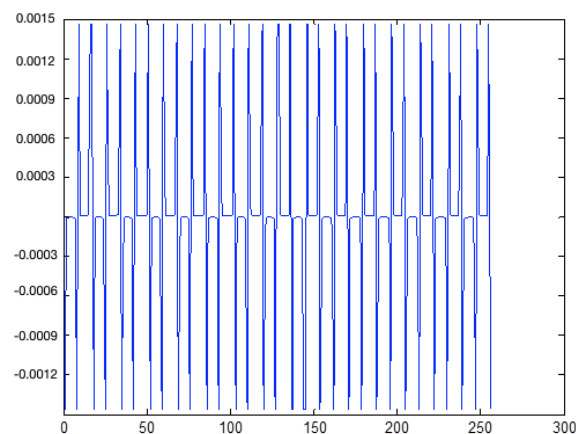


Figure 2.35: Simulated differential voltages.

I used real data acquired according with the file in appendix B.4 as second data set. This file was simpler than that generally used for acquiring a complete dataset, already explained in paragraph 2.3, figure 2.25. In fact the file did not acquire $V_{opposite}$ and $V_{opposite_inverse}$ for evaluating the crosstalks presence Also the V_{nodeA} were not acquired. These simplifications were justified by the resistive behavior of the saline solution already studied in paragraph 2.2.1. I knew that, since the impedance was approximately real, any difference in phase angle should has been inducted on the electric current passing through the phantom with respect the voltage applied to the sample. That was why the file acquired only the V_X component and the electric current for the software was calculated as $V_g / (3.9 + R_{mux})$. Setting a V_g on the Lock-in of 50 mV with 10 KHz of frequency I obtained $12.008 \mu A$. The experiment was conducted on a saline solution 0.9% with conductivity 14.44 mS/cm which filled up the tank.

The acquisition code performed the opposite stimulation and the adjacent measurements, and I obtained the real dataset in figure 2.36.

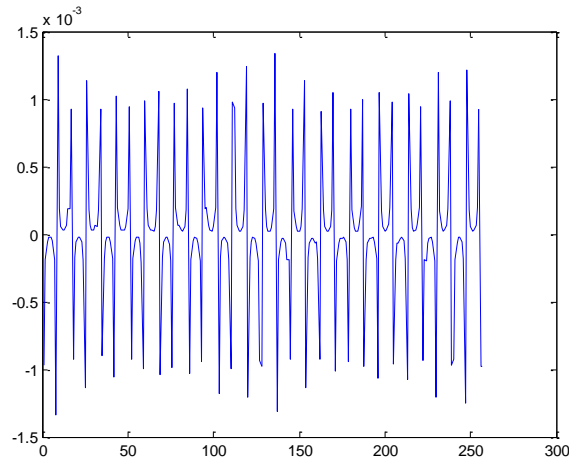


Figure 2.36: Real voltages.

As one can notice noise is visible with respect the ideal case of simulated data.

The inverse model was a simplified two dimensional mesh, scaled for the dimension of the tank.

Then the inverse solver was implemented for “difference” imaging.

The solution of the inverse solver produced the following image.

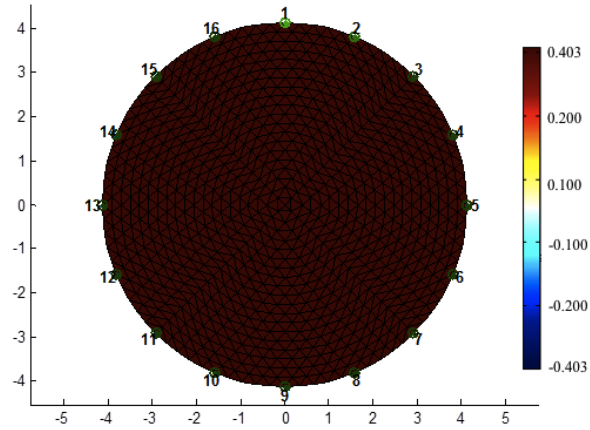


Figure 2.37: Inverse solution homogeneous conductivity map. The tank contains the electrodes of the circular array numerated 1 to 16.

The image is the tank of real dimensions discretized in 8716 brown colored elements. The color indicates the difference in conductivity evaluated by the inverse solver to which is associated the maximum value of 0.403 mS/cm of the colorbar. The conductivity map was evaluated to be of 14.8423 mS/cm for each element inside the tank with respect the saline solution's real conductivity value. I could notice that the reconstruction of the map reproduces the real homogenous conductivity map, since the maximum difference between reconstructed points was only 0.403 mS/cm. This first inverse solution and imaging implementation suggested that EIDORS was capable of EIT imaging.

Chapter 3

3. Inhomogeneous Reconstructions of Various Objects

3.1 Images of Conductive and Insulating Objects

Electrical Impedance Tomography is defined as a new imaging technique which enables visualization of spatial distribution of electrical properties inside conductive object. Its aim is to visualize the internal electrical properties in an image. In this chapter, I evaluate the performance of the proposed EIT system, as described in the previous chapter, using the images of 13 experiments obtained with reference objects of known electrical properties. Obviously, in real life medical experiments the measured domain would be irregular shaped and the electrical properties of anomalies would not be so far from those of the surrounding tissues. However, due to the difficulty in preparing the phantom, I chose high conductivity and insulating objects, which represented the isotropic conductivity case, since the electrical properties were invariant in each direction. These objects are the first and easier way used for testing EIT systems which can be found in the literature [45]. Images obtained from objects with extreme electrical properties and homogeneous medium with different electrical properties, in theory produce a good contrast. Since the forward and the inverse solver could solve and produce accurate results in terms of simulated boundary voltages and image reconstruction in treating medium with homogeneous conductivity, as a saline solution (I remind experiment in 2.5 and 2.6 paragraphs, chapter 2), two numerical simulations for image reconstructions were performed on a circular domain of 8.24 cm in diameter with material properties of 17.7 and 0.5mS/cm, i.e. material with higher and lower electrical properties with respect the background. The homogeneous conductivity of the background was settled as the conductivity value of a saline solution 0.4 %, which was 7.7 mS/cm. In the literature [83] a particular kind of reference phantom in fact is described, in which the background consists of a liquid conductive medium that can be imaged by an EIT system using surface electrodes. The conductive medium usually consists in a conductive gel or a saline

solution inside which are inserted targets, whose electric property contrasts with that of the medium.

Our EIT system with circular electrode array has been simulated. The simulations were conducted to compare the obtained boundary voltages with the measured ones and to understand the algorithm ability in discriminating different electric properties inside the tank.

The image reconstruction EIDORS file of the simulations in appendix C.1.2 consisted in two parts. A forward model with the inclusion was used to predict the homogeneous and inhomogeneous boundary voltages for the particular internal admittivity distribution and the current inject protocol. I named homogenous voltages (*vsimh* in the EIDORS code) the solution of the forward solver for the constant conductivity of the background, and inhomogeneous voltages (*vsiminh* in the EIDORS code) the solution for the background and the circular different conductivity together. The electric current was of $12.008\mu A$. The second part of the reconstruction process was the inverse solution. Information from the forward model was used in the inverse solution to produce an approximate internal impedance distribution. Being the reconstruction implemented with a three dimensional mesh, the same in figure 2.26 (chapter 2), the reconstruction time was 3 minutes. The results of the simulations will be explained below to be compared with corresponding results from real experiments.

For these, the EIT system was tested using a tank of cm 8.24 in diameter filled with 30 ml of saline solution 0.4% and 13 objects with different property placed inside, subsequently imaged by EIT. The tank was filled about 0.264 cm in height. The ring with 16 electrodes was inserted inside the solution around the volume of interest and an excitation of 50 mV at 10 KHz was applied to 16 electrodes any time and the system recorded all the voltages from adjacent electrodes, according with the file acquisition file code (appendix B.4). Particularly, the acquisition code was used twice for each experiment: the first time was to acquire the boundary voltages (*vh*) when the tank was filled only with saline solution; the second time corresponded to the acquisition of saline solution plus an object (*vi*). By a first observation on the data acquired in each experiment it was found that the variation in phase angle between the electric current trough the phantom and the voltages applied on electrodes stimulation was null, so I processed only the *in phase* component of the boundary voltages. The measured voltages were then used as input for an EIT algorithm capable of performing the image reconstruction.

The EIDORS code in appendix C.2.2 was implemented in order to load the measured data v_h and v_i and to record them in the apposite field as forward solution. Their processing entails the selection of the regularization parameters or *hyperparameter values*. Those were tuned manually for best visual reconstruction quality in each reconstruction. For the inverse solution I used a finer mesh of 1600 tetrahedral elements as opposed to a three dimensional real mesh, in order to solve the problem as a two dimensional case, since there were no variations in electrical properties with height, and to decrease the computational time , which settled at 3 seconds. The obtained images yield conductivity information and not permittivity, since I processed only the *in phase* components.

For each experiment I show the reconstructed image with the corresponding plot of boundary voltages from homogeneous and inhomogeneous data acquisitions.

The parameters that were used to compare all the reconstructed images were the localization accuracy, the resolution and the image quality in terms of contrast. I analyzed the congruency of these acquisitions and reconstructions comparing them with the results of two main simulations: the first was a simulation of a conductive inclusion inside the background; in the second one the inclusion had lower conductivity than the background.

In the first experiment a metal conductor of diameter 5 cm was used as an inclusion which was located at the center of the tank as shown in figure 3.a. Figure 3.b shows instead the mesh of the simulated experiment with the conductive inclusion inside the tank at 2 o'clock.

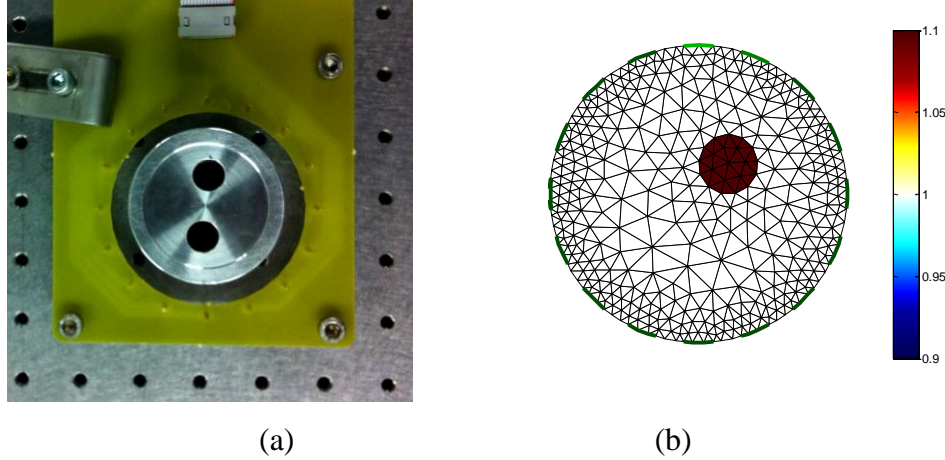


Figure 3: The real experiment and the simulation.

- a) A photograph of the measurement setup for the 1st experiment. Test profile with tank of saline solution 0.4 % and a metal conductor 5cm in diameter. b) Simulation: two dimensional mesh of the tank with the saline solution (7.7 mS/cm) and the conductive inclusion (17.7 mS/cm).

Even if the simulation did not effectively reproduce the real experiment, I though could be useful in comparing boundary voltages and reconstructions in ideal conditions. As one can notice the in figure 3.1 b first row, the simulation produced the same plot of the voltages of the 256 measurements of the previous forward experiment, according with chosen scan modality. Its forward solutions were inhomogeneous simulated voltages (blue line) lesser in module than the homogeneous ones (green line). Then image was reconstructed from simulated data sets (second row of figure 3.1 b) and the circular object shown in figure 3.1 b was clearly identifiable on the image (the white area is the background and the blue is the object with higher conductivity value). I remind that this and the following images do not represent absolute conductivity values, but the difference between saline solution and object conductivity being the object conductivity lesser than the background, in difference imaging it is indicated with the color corresponding to lower values of the color code.

The simulation was the first test of inhomogeneous reconstruction and it was found that the software was able to discriminate different conductivity values, but the reconstruction was not so accurate around the object since the light-blue area is reconstruction artifact due to the inverse solver. In fact, as explained in Chapter 1, the inverse problem is ill-posed: the acquired data is

not sufficient, the number of nodes is higher than the number of voltages, and the solution is not unique. Even if a regularization is applied to add extra information, resulting images are non-smoothed and with artifacts.

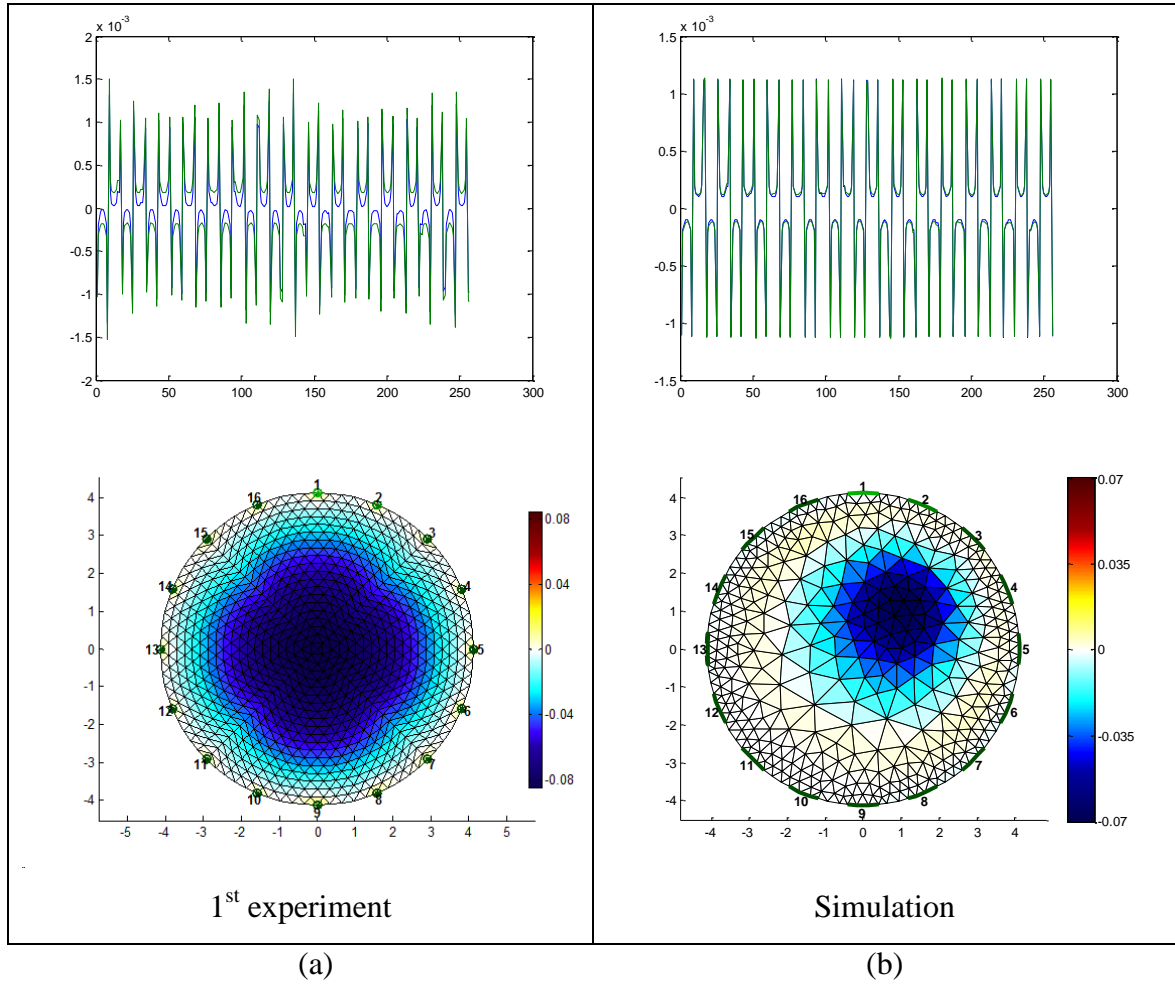


Figure 3.1: Comparing boundary voltages and reconstructions results between the 1st experiment and the simulation. a) Real experiment results: in the top row is shown the plot of 256 acquired data. v_h , is the green line, v_i the blue one. In the bottom row is represented reconstructed image using acquired data and *hyperparameter* value 0.005. b) Simulation results: in the top row, plot of 256 simulated data. V_{simh} is the green line, v_{simih} is the blue one. In the bottom row, reconstructed image using simulated data and *hyperparameter* value 0.03.

The first comparison between experiment and simulation concerns the acquired data in the real experiment (v_h , v_i) and the simulated data of the simulation code ($vsimh$, $vsiminh$). From the experiment I acquired voltages, whose plot in the first row of figure 3.1a is similar to the simulation one in terms of pattern of measurement, with a certain level of noise. The plot is not visually perfect, but it shows that the module of the inhomogeneous voltages was again lesser than the homogeneous ones. This confirmed that the system acquired correct values when the experiment involved conductive object. Images in the second row of the figure representing spatial distributions of the conductivity were reconstructed with proper object size and position. The reconstruction showed that the conductor, represented again with blue area, was well localized at the center of the tank with minimum light-blue colored edge artifacts coherently with the simulation. The positive results of the experiment brought me trying different objects in order to obtain images from different conditions.

In the second and third experiment I used a brass coin placed not only at the center of the tank, but also displaced as shown figure 3.2 a and 3.2b.

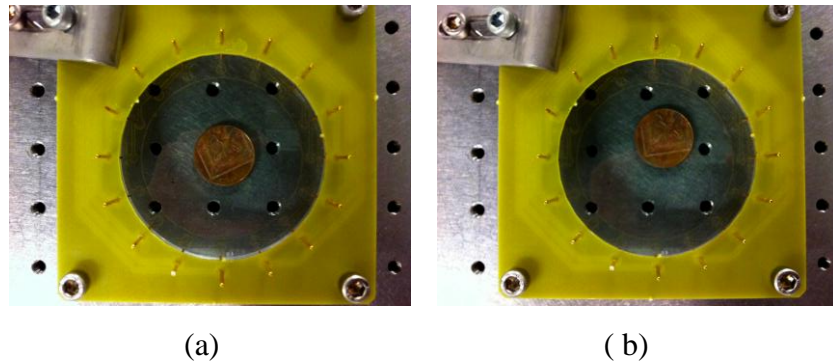


Figure 3.2: Two photographs of the measurement setup for the 2nd (a) and the 3rd experiment (b). The metal conductor 2.5 cm in diameter was a coin differently placed inside the tank.

The acquired data in the first row of figure 3.3 a and 3.3 b were consistent with the previous experiment and with the simulation. The level of noise this time seems to be decreased, but still

present. The reconstructions could well localize the object in the right position in both of the cases, but with more artifacts, as shown by slightly “yellow” (high-conductance) areas.

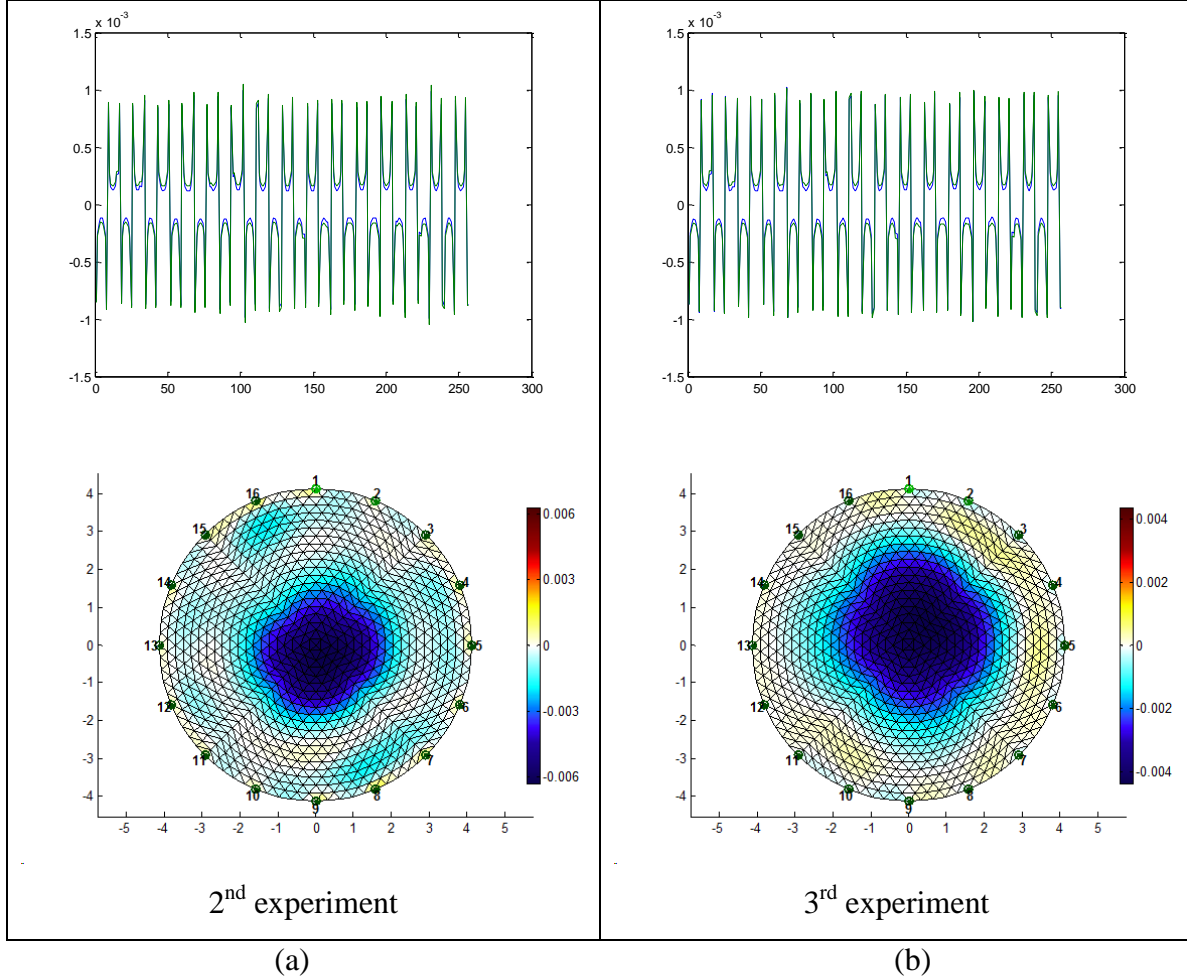


Figure 3.3: Boundary voltages and reconstructions results of the 2nd and the 3rd experiment. a) 2nd experiment results: in the top row is shown the plot of 256 acquired data. vh , is the green line, vi the blue one. In the bottom row is illustrated the reconstructed image using acquired data and *hyperparameter* value 0.001. b) 3rd experiment results: in the top row is shown the plot of 256 acquired data. vh , is the green line, vi the blue one. In the bottom row is illustrated the reconstructed image using acquired data and *hyperparameter* value 0.007.

The images showed that the system was effective in treating different conductive object and I decided to try two metal objects as inclusions in the 4th, 5th and 6th experiments. I decided to use

objects with the same conductivity in each experiment and not so big to create a short circuit inside the tank as it can be noticed in the following photos.

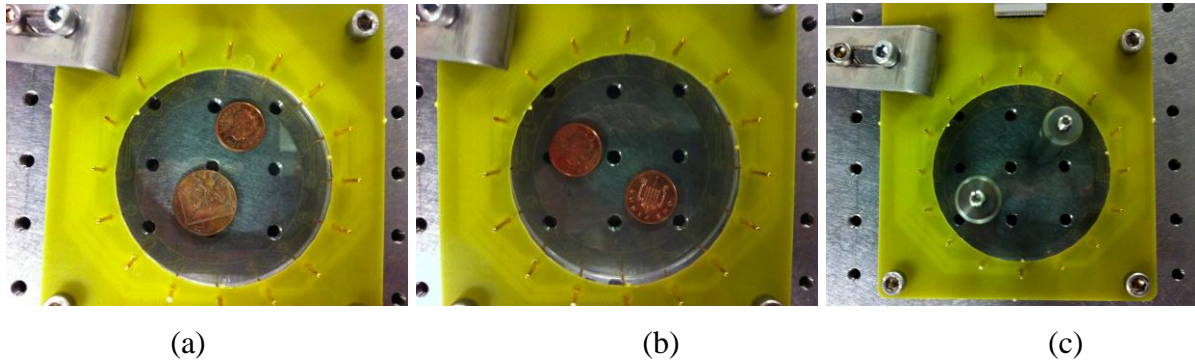


Figure 3.4: three photographs of the measurement setup for the 4th (a), 5th (b) and 6th (c) experiment. Test profile with 2 coin with cm 2.5 and cm 2 in diameter, 2 coins with 2 cm of diameter, and 2 metal objects with 1.6 cm of diameter.

The acquired voltages kept the pattern for the acquisition modality even using 2 objects, and the noise was present. I could notice that the difference between the blue (background) and green (inclusion) line in experiments with different conductive object depends on the conductivity value of the object and on the distance with the saline conductivity. It was possible obtain a correct reconstruction of the experiment with the images. They could visualize the object oriented in the right way and defined with blue areas. No many artifacts were visualized, but the shape of the objects inside the biggest convex boundary (the “close sides”), was not reconstructed. An explanation of the phenomenon can involve the low value of the electric current with respect the conductivity of the object. The current probably could not get in easily the space between the objects and create a detectable distribution of the electric field, sufficiently higher than the noise floor. These results were comparable with those images in the literature obtained by EIT system using EIDORS for solving the inverse problem.

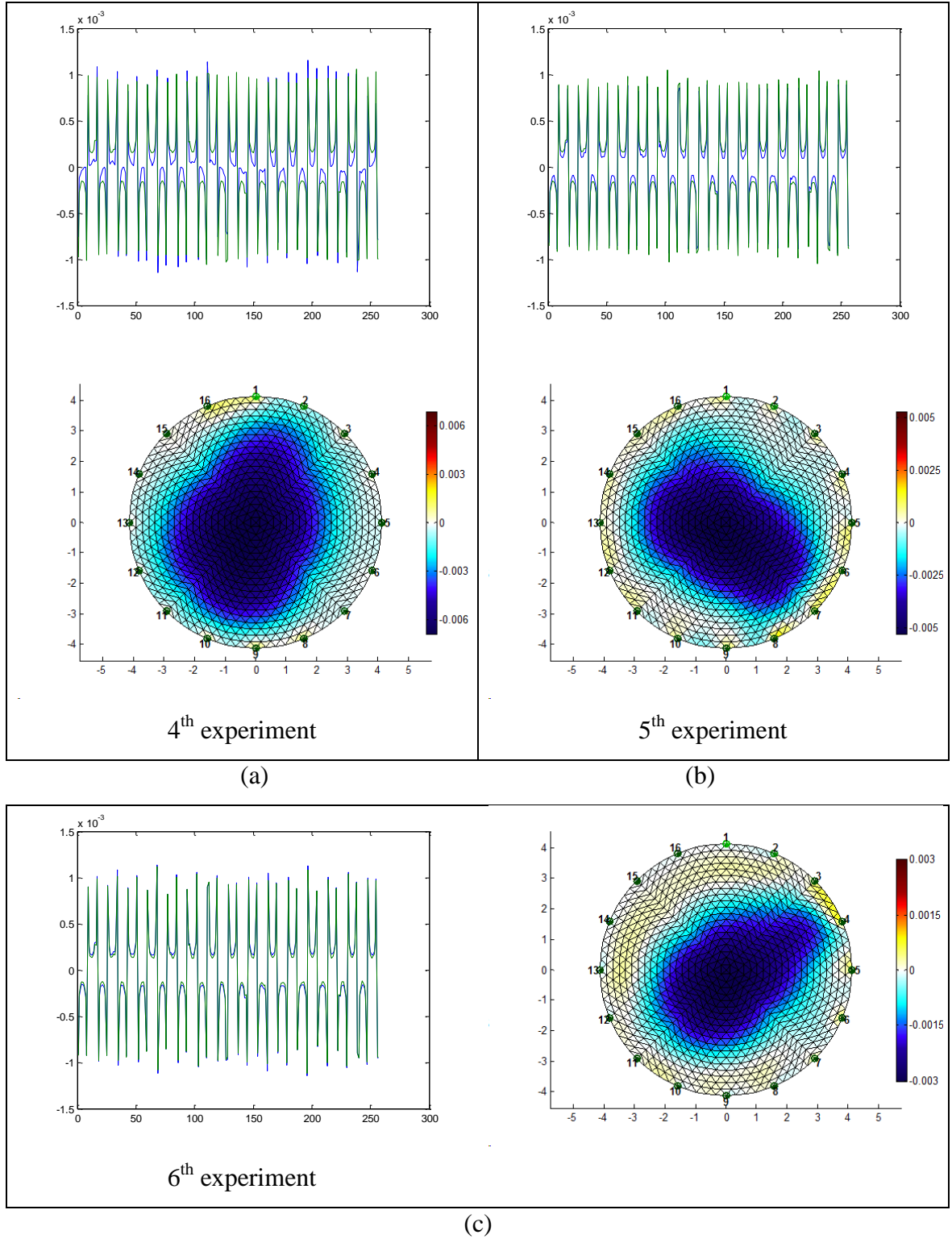


Figure 3.5: Boundary voltages and reconstructions results of the 4th, 5th and 6th experiment. a) 4th experiment results: in the top row is shown the plot of 256 acquired data. v_h is the green line, v_i the blue one. In the bottom row is illustrated the reconstructed image using acquired data and *hyperparameter value* 0.05. b) 5th experiment results: in the top row is shown the plot of 256 acquired data. v_h is the green line, v_i the blue one. In the bottom row is

illustrated the reconstructed image using acquired data and *hyperparameter value* 0.01. c) 6th experiment results: in the first column is shown the plot of 256 acquired data. v_h , is the green line, v_i the blue one. In the second column is illustrated the reconstructed image using acquired data and *hyperparameter value* 0.008.

After using conductive object I analyzed the case of insulators, proceeding in the same way, with the comparison between results and simulation.

The simulation was the same implemented for the conductive inclusion of the appendix C.1.2, by setting the object conductivity at lower value than the background. In this case the forward solutions were inverted in the plot in the first row of figure 3.7 b. The blue line that represents again inhomogeneous voltages obtained with the presence of the inclusion was bigger in module than the homogeneous ones. The image in the second row of the figure could visualize the different electric property inside the tank, illustrating the object with red color corresponding to the positive value of the difference in conductivity. The results were coherent with the treated case and were again present artifacts in the reconstruction of the same magnitude.

For the 7th and 8th experiments I used as inclusion a plastic tank of diameter 3.48 cm. I changed the location inside the tank from the center to one side of that (figure 3.6 a 3.6 b)

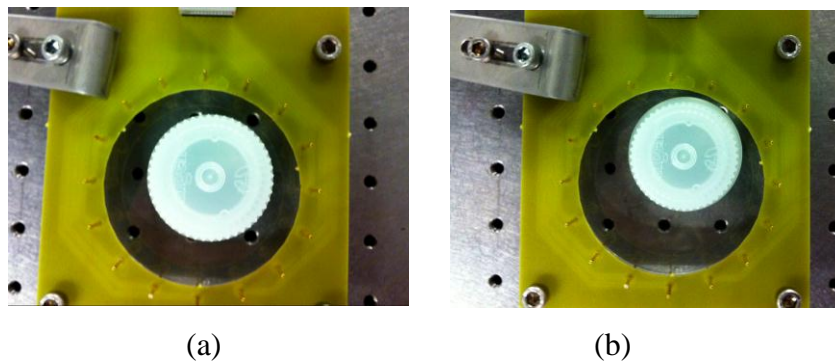


Figure 3.6: A photograph of the measurement setup for the 7th (a) and the 8th (b) experiment. Test profile plastic object of 3.48 cm in diameter.

The reconstructed images were obtained with the same accuracy and the object was red colored. The position of the object was correctly visualized even if edge artifacts around the object influenced the correct visualization of the shape.

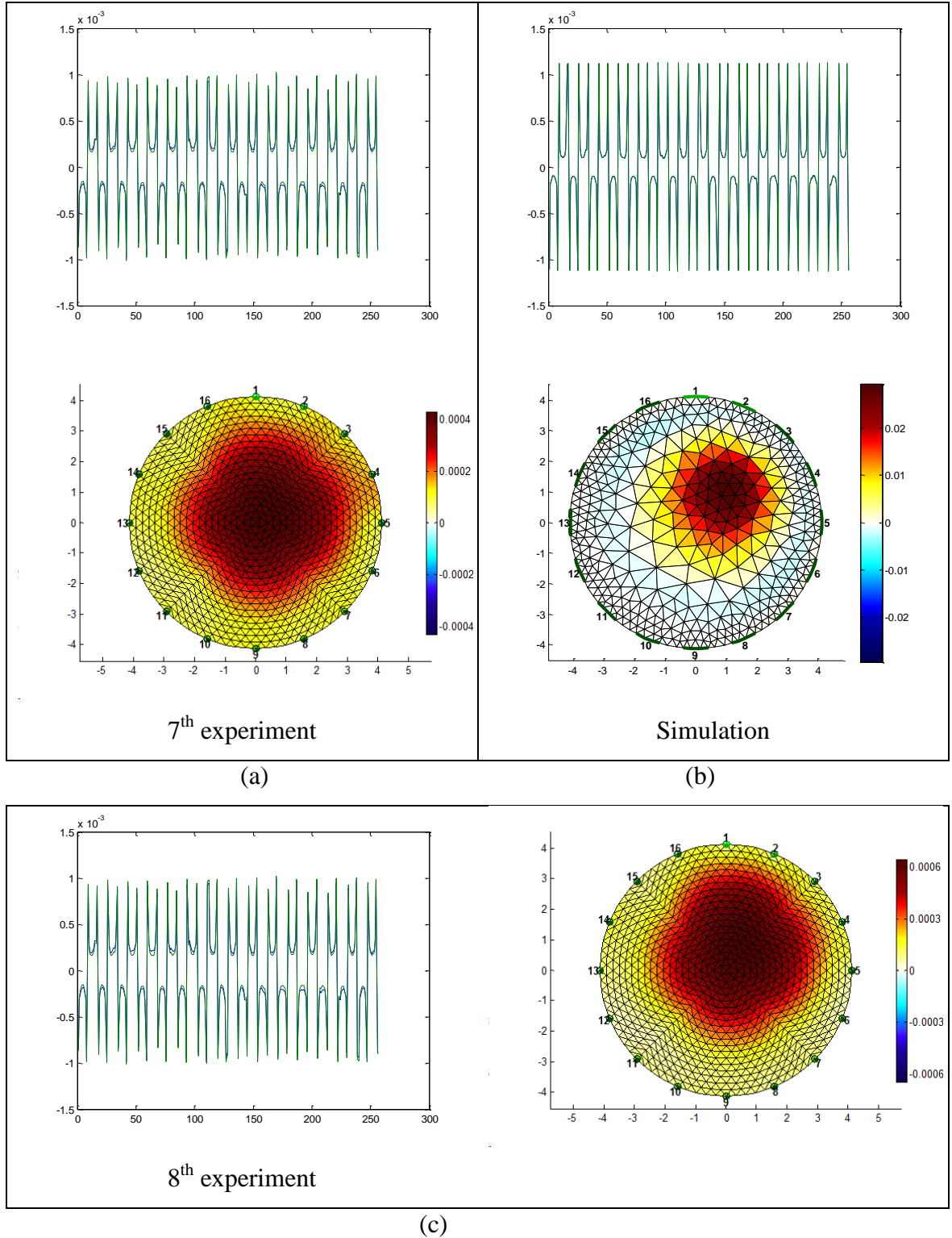


Figure 3.7: Comparing boundary voltages and reconstructions results between the 7th, 8th experiment and the simulation. a,c) Real experiment results: plot of 256 acquired data. v_h is the green line, v_i the blue one. In the bottom row is illustrated the reconstructed image using acquired data and *hyperparameter values* 0.00465 and 0.08.

b) Simulation results: in the top row, plot of 256 simulated data. V_{simh} is the green line, v_{siminh} is the blue one. In the bottom row, reconstructed image using simulated data and *hyperparameter value* 0.03.

In the experiments 9th and 10th I used another insulating object, this time smaller than the first used again changing its location (figure 3.8 a and 3.8 b), just to see if the results could be obtained again.

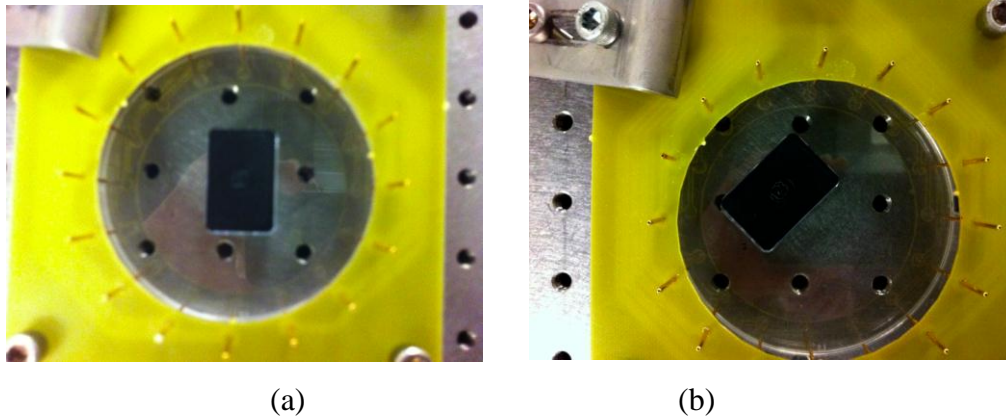


Figure 3.8: A photograph of the measurement setup for the 9th (a) and the 10th (b) experiment. It was used a different plastic object wide 1.8x2.8 cm.

All the results were comparable with the previous ones obtained, but the reconstruction this time suffered from considerable artifacts evidenced by inconsistent differences in conductivity (blue area in the tank) involving also the electrodes. Despite of this, the red area corresponded to the location of the object (figure 3.9).

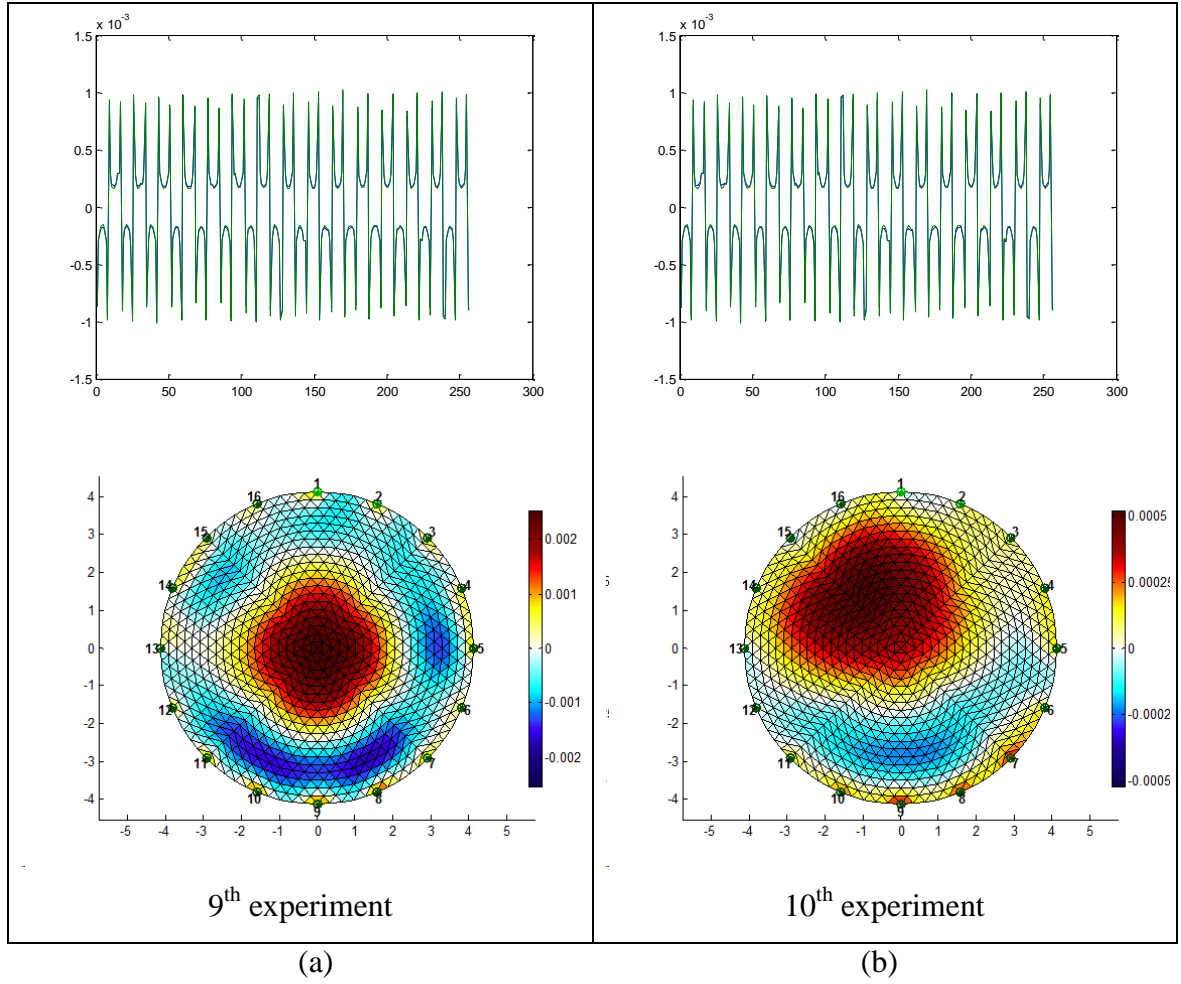


Figure 3.9: Boundary voltages and reconstructions results of the 9th and the 10th experiment. a) 9th experiment results: in the top row is shown the plot of 256 acquired data. vh , is the green line, vi the blue one. In the bottom row is illustrated the reconstructed image using acquired data and *hyperparameter value* 0.005. b) 10th experiment results: in the top row is shown the plot of 256 acquired data. vh , is the green line, vi the blue one. In the bottom row is illustrated the reconstructed image using acquired data and *hyperparameter value* 0.046.

I finally tried the case of two different plastic objects with different size (figure 3.10 a, 11th experiment). For the acquired voltages and reconstruction the same considerations of experiments with one plastic object are valid. As the case of 2 metal objects the reconstruction had some difficulty in reproducing the faces on the side of the objects close to each other.

The most interesting case was the combination of insulating and conductive objects together as the case of 12th and 13th experiments. This case was very significant, because I wanted assure that the system could work in presence of objects with very different electrical properties. The reconstructions in figure 3.11 a and 3.11 c were made with the same features than the others: the conductive object was represented as blue (high conductance) and the insulating one as red (low conductance), visualized in both cases in the right location. The results underlined the fact that the system worked well in each case, but there were again the problem of artifacts and difficulty in reproducing the shape. This problem was again probably due to the ill-posedness of the reconstruction.

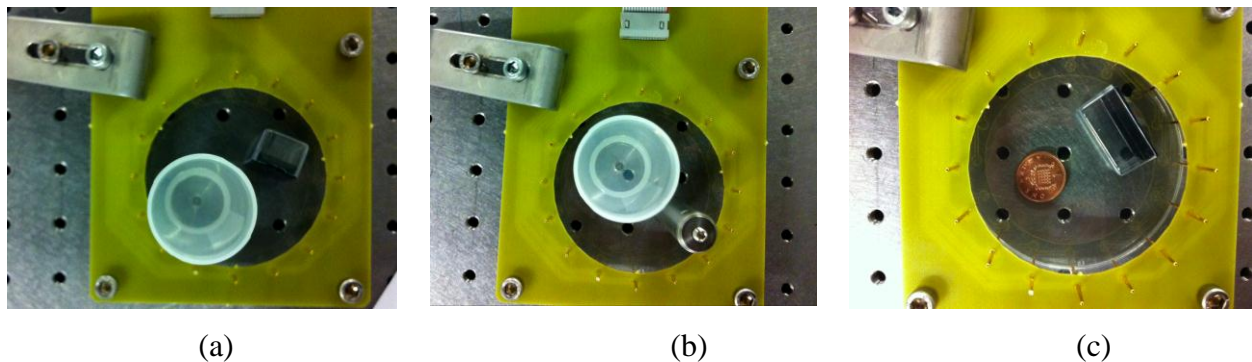


Figure 3.10: A photograph of the measurement setup for the 11th, 12th and 13th experiment.

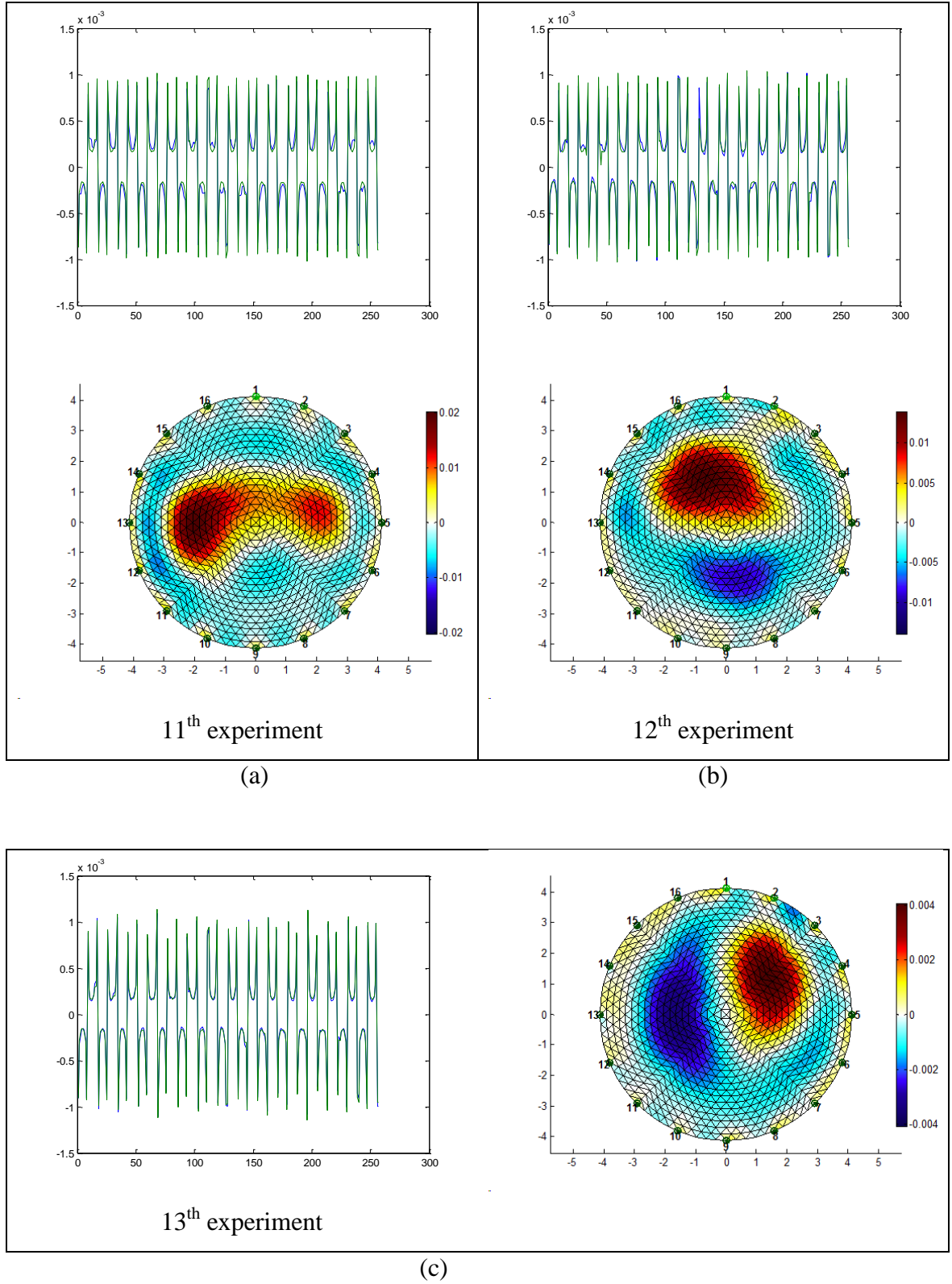


Figure 3.11: Boundary voltages and reconstructions results of the 11th, 12th and 13th experiment. a) 11th experiment results: in the top row is shown the plot of 256 acquired data. v_h is the green line, v_i the blue one. In the bottom row

is illustrated the reconstructed image using acquired data and *hyperparameter value* 0.001. b) 12th experiment results: in the top row is shown the plot of 256 acquired data. v_h , is the green line, v_i the blue one. In the bottom row is illustrated the reconstructed image using acquired data and *hyperparameter value* 0.003 c) 13th experiment results: in the first column is shown the plot of 256 acquired data. v_h , is the green line, v_i the blue one. In the second column is illustrated the reconstructed image using acquired data and *hyperparameter value* 0.0046.

3.2 Results

This first series of 13 experiments was a solid method of evaluation of the EIT system performance in terms of implemented hardware and software.

The hardware component was stable in acquiring boundary voltages coherently with the type of object used as inclusion. In each experiment the system always recorded zero quadrature component of the voltages and measurable *in phase* component. The comparison with the data and the simulations showed that the correct pattern of measurement was always obtained and underlined the presence of noise in acquired voltages. Even though additive errors, such as due to the channel crosstalk and noise, these data were processed for obtaining successful images. To evaluate the performance of the software and mainly of the implemented algorithm for solving the inverse problem, firstly two numerical simulations were made to test the stability of the chosen imaging method in making isotropic conductivity reconstructions. They obtained good reconstruction results useful as term of comparison with images reconstructed from the experiments. The simulation indicated the strength of the NOSER algorithm in discriminating inhomogeneity in conductivity reconstruction.

All the reconstructed images in difference modality visualized conductive objects (with blue areas) and insulating objects (with red areas) even if the objects were inserted in the tank together. The algorithm associated the difference conductivity value with each element of the mesh, as higher or lower than the saline conductivity value. As it could be observed, with this system it was possible to detect objects inside the tank, and the cross sectional images (two-dimensional reconstruction of the conductivity map) matched the position of the object. The sizes and the proportion between different object were always respected.

The system was not sensitive to those shapes whose dimensions were under the distance of the electrodes. There were considerable edge artifacts around the object and they were visualized non-smoothed due to the ill-posedness of the problem.

These considerations clearly indicated that: Despite the NOSER algorithm was simply a one-step regularization process, it was able to solve the inverse inhomogeneous problem in as little as 3 seconds; the EIT system without rejecting of systematic errors and noise could obtain two-dimensional images of the tank with the objects with comparable performance of a known EIT system of the Maltronint Group (www.maltronint.com) and of each other EIT implementation in the literature to my knowledge [76]; The usage of in-phase component, i.e. the real part of the impedance, produced resistive images of good contrast.

Chapter 4

4. Biological Sample Imaging

4.1 The Complex Admittivity Case

The electrical properties of biological tissues have been of interest for over a century for many reasons. They determine the pathways of current flow through the body and, thus, are very important in a wide range of biomedical applications. Evaluating the electrical properties of tissues is complex, because they can depend on the tissue orientation relatively to the applied field (directional anisotropy), the frequency of the applied field (the tissue is neither a perfect dielectric nor a perfect conductor), or they can be time-and space-dependent. Other several factors can make the measurement of tissue dielectric properties elusive, such as tissue inhomogeneity, the physiological state of the tissue, and electrode polarization. This is why there are many discrepancies in the reported values of the electrical properties of biological material. Therefore, caution must be used in the design of the measurement procedure. To analyze the response of a tissue to electric stimulation, one needs data on the specific conductivities and relative permittivities of the tissues. In this framework, I chose a tissue section as a biological sample, to be used in order to obtain both two components of the impedance. I wanted evaluate the possibility of recoding both of them to test the EIT system behavior in the real case of an actual biological sample and to try to do actual image reconstruction.

First of all I decided to understand what impedance (or admittivity) value had great relevance in a real tissue experiment. I wanted evaluate if these values were detected by the EIT system in AC conditions and if they could produce images. For this preliminary experiment I chose a palm of the hands as sample since it was sufficiently large to be suitable for the circular electrodes array. As body parts with homogeneous properties do not exist, the acquisition procedure (Matlab file code in appendix B.4) was used just once for acquiring only inhomogeneous voltages v_i ,

corresponding to the entire sample. The acquisition did not show quadrature components of the voltages, probably because the electrodes were not kept in depth of the palm but they applied only current superficially on the first layer of the skin that is known to be insulating. Then impedance of the skin was therefore strongly resistive.

In figure 4 one can note the distinctive behavior of v_i under 100 mV of excitation and 10 KHz of frequency: the concave part of the graphic, noticed on the measurements with various objects in the previous chapter, was not reproduced completely. The level of noise was not identifiable since the sample was a real tissue with non-ideal behavior, but it is highly likely that systematic errors were present.

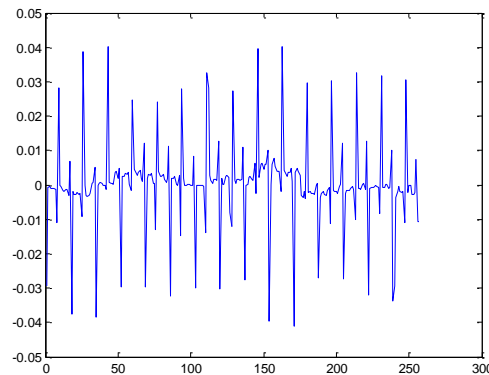


Figure 4: Preliminary experiment : Acquisition on a palm of hand.
Plot of acquired inhomogeneous Voltages v_i .

The data processing file was the same of the 13 previous experiments (file EIDORS code in appendix C.2.1). It loaded only the acquired data and a matrix of zeros as homogeneous data to subtract in difference imaging modality.

The reconstructed image in figure 4.1 visualized a uniform blue colored central area representing the internal part of the hand, red region on the left top side where the electrodes did not adhere to the palm and a yellow region on the right bottom side where they just sideways adhered to the

hand. In the image the difference between zero matrix and v_i gave a difference conductivity value minor on red regions and major on the blue ones. Reasonably red regions corresponded to electrodes not touching the hand air and blue regions to the skin. Moreover the blue region was elongated in the direction of the actual hand placement.

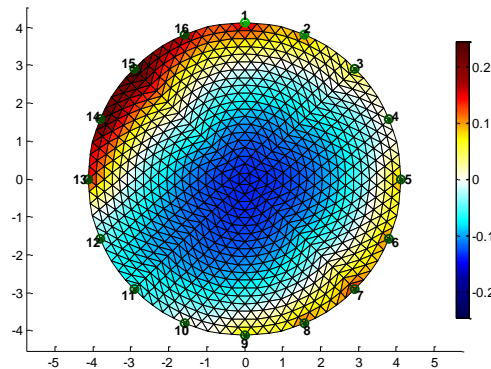


Figure 4.1: Reconstruction of the palm of the hand.

Result of the EIDORS code in appendix C.2.1 with acquired data and *hyperparameter* value 0.03.

4.2 Biological Sample: Tissue Section

For the case I chose a bovine muscle-and-tendon cross-section (Ribeye steak, figure 4.2) with of the tendon exhibiting different electrical properties than the bulk muscle, yielding an anisotropic conductivity reconstruction case. Two experiments with rotated position of the tissue were made (figures 4.4 a and 4.5 a). The tissue was 1.6 cm tall and it was cut in a circular shape to fit the circular array of electrodes pressed in the depth of the tissue. The corresponding mesh with 8044 elements is shown in figure 2.27 of chapter 2. Considering deep location of the electrode array in the tissue, I tried, for the first time in this thesis, a three-dimensional reconstruction mainly because most objects of medical interest are three-dimensional. Electric current in three-dimensional objects cannot be confined to a plane but flows above and below the plane defined

by the electrodes and, inside the anisotropic medium, the admittivity changes along its height. This calls for image reconstruction as a fully three-dimensional problem. The reconstruction file (appendix C.2.3) associates directly the three-dimensional mesh of the tissue to the forward field of the inverse model.



Figure 4.2: Photograph of choso tissue section.

As the case of the hand, the acquisition strategy regarded only one data set which was processed alongside with the matrix of zeros [128].

In both the experiments, performed below 100 mV of excitation voltage at a 10 KHz frequency, the acquisition system recorded V_{nodeA} and $V_{adjacent}$ as not in phase, with a difference in phase angle of -1.5 to -2 degrees, which called for pre-processing the data (please refer to 2.2 for the procedure). The acquisition was performed also for the quadrature component, which is generally due to the electric capacitance membranes. As in the literature I found [60] that these are considerable at 1 MHz of frequency, the outcome of a reconstruction from such quadrature components was unclear. Surely, however, the *in-phase* and quadrature component of the voltages represented conductivity and permittivity of the impedance.

The figure 4.3 shows the acquired data plot in both the experiments.

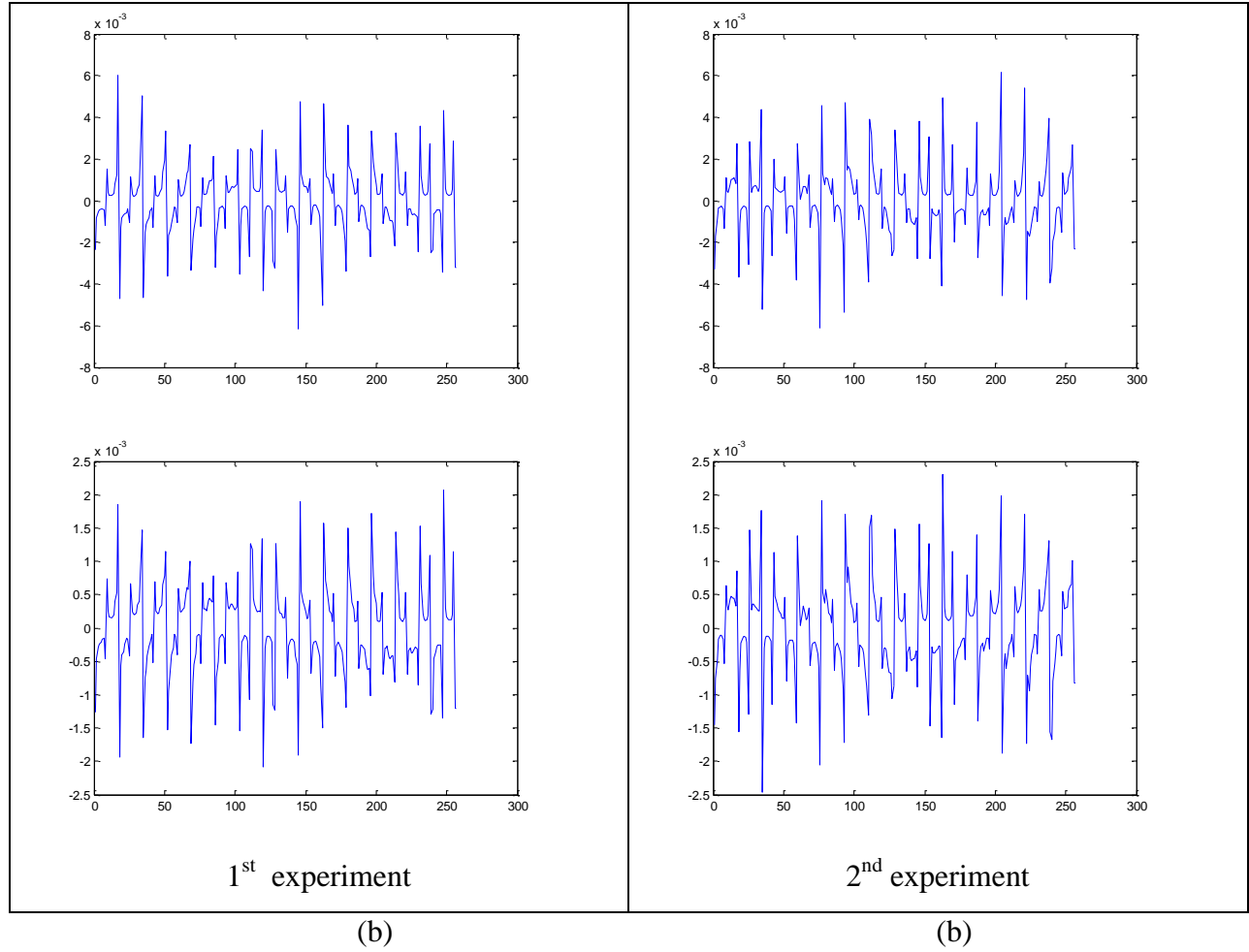


Figure 4.3: Acquired data sets from the 1st and 2nd experiments.

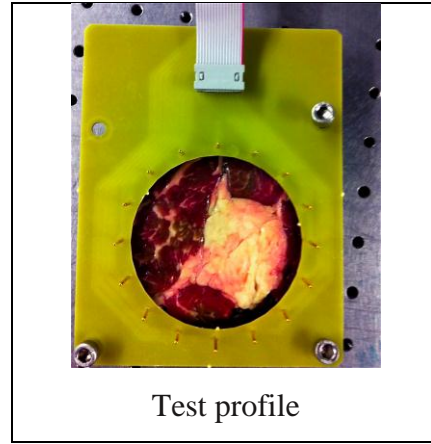
(b) First Experiment Results. First row: the *in phase* component V_X . Second row: quadrature component V_Y .

(b) Second Experiment Results. First row: the *in phase* component V_X . Second row: quadrature component V_Y .

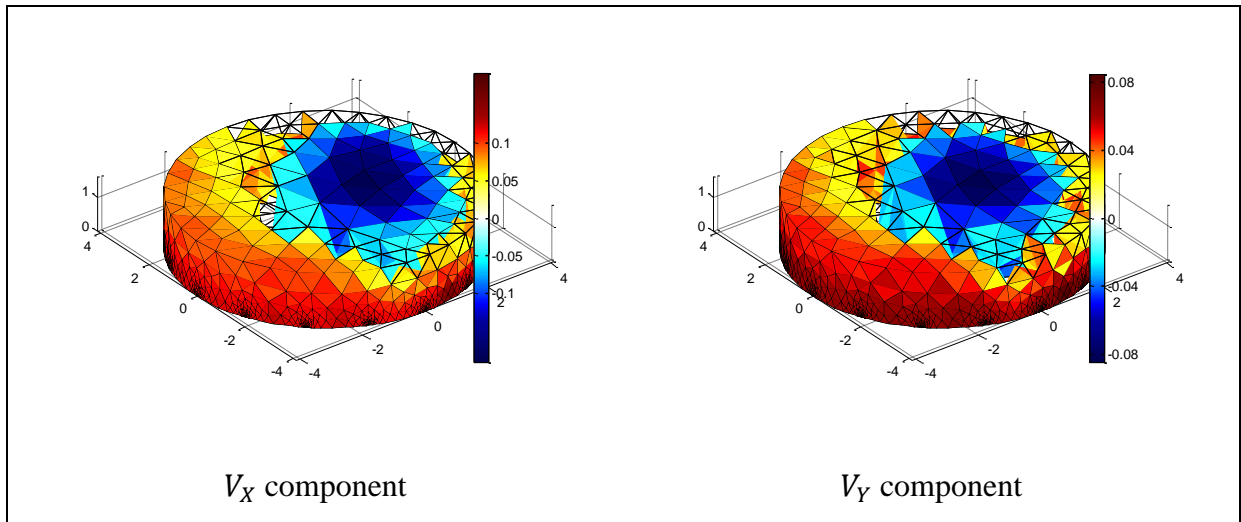
The same considerations as for the preliminary experiment were done, as acquisitions from real tissues. I found a strong correlation with the theory of impedance in the literature [27] since the quadrature components were always lower than *in phase* components.

The processing of data produced the three-dimensional reconstructions in figure 4.4 b (first experiment) and figure 4.5 b (second experiment) coming from *in phase* component processing. Quite similar reconstruction derived from quadrature component, as shown in the images in

figure 4.4 c (first experiment) and figure 4.5 c (second experiment). All the reconstructions are conductivity average images.



(a)



(b)

(c)

Figure 4.4: Reconstructions for the 1st experiment.

- (a) 3D reconstruction coming from *in phase* component V_X (c) 3D reconstruction coming from *quadrature* component V_Y .

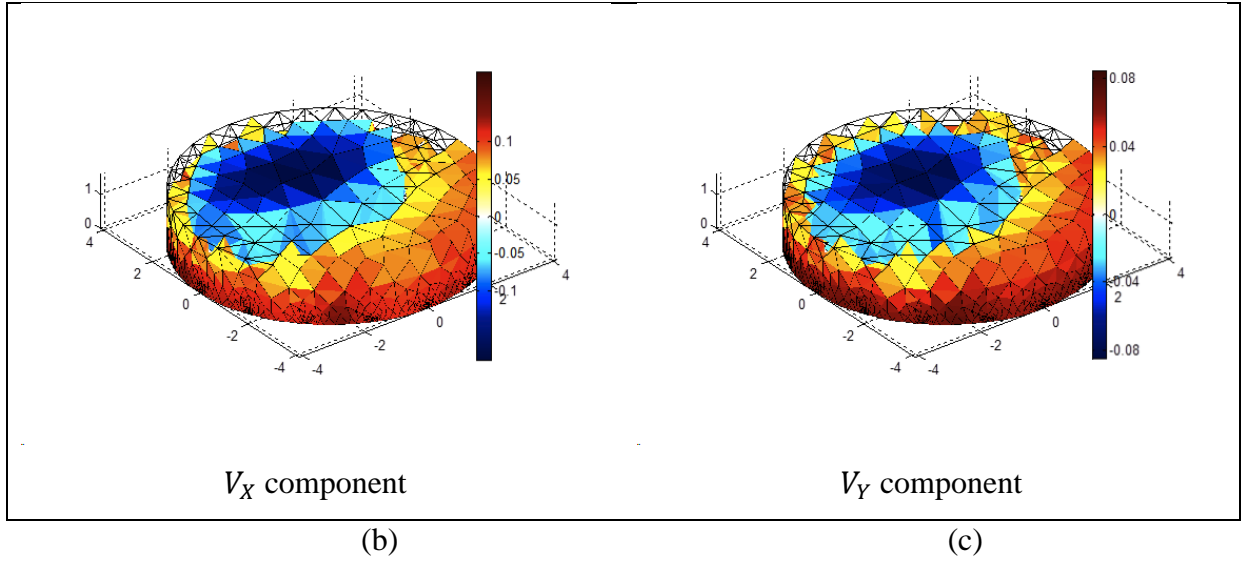
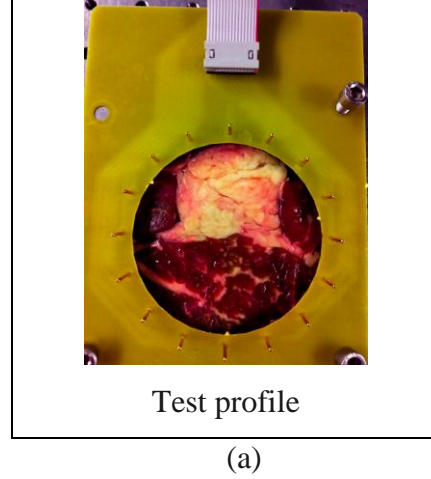


Figure 4.5: Reconstructions for the 2nd experiment.

(b) 3D reconstruction coming from *in phase* component V_X (c) 3D reconstruction coming from *quadrature* component V_Y .

It was clearly noticed that in each experiment, correlated resistive and capacitive images have been derived from the same sample. All the images visualized the white part of the tissue with blue areas and lower average conductivity and permittivity, and the rest of the tissue with areas at higher average conductivity or permittivity (red colored areas). The white part of the tissue was well defined and the images had a good contrast. Moreover I found a considerable

consistency of the values of the average map conductivity and permittivity, despite the noise and the errors in the acquired data sets. In fact in resistive images the values distribution was comprised in 0.1 mS/cm interval and in capacitive images it was comprised in 0.08 mS/cm interval.

The three-dimensional distribution of conductivity and permittivity of both the experiments is presented in figure 4.6-4.7 and 4.8-4.9 as a set of four two-dimensional cross-sectional images with increasing depth. The cross-section planes are parallel to the electrode array.

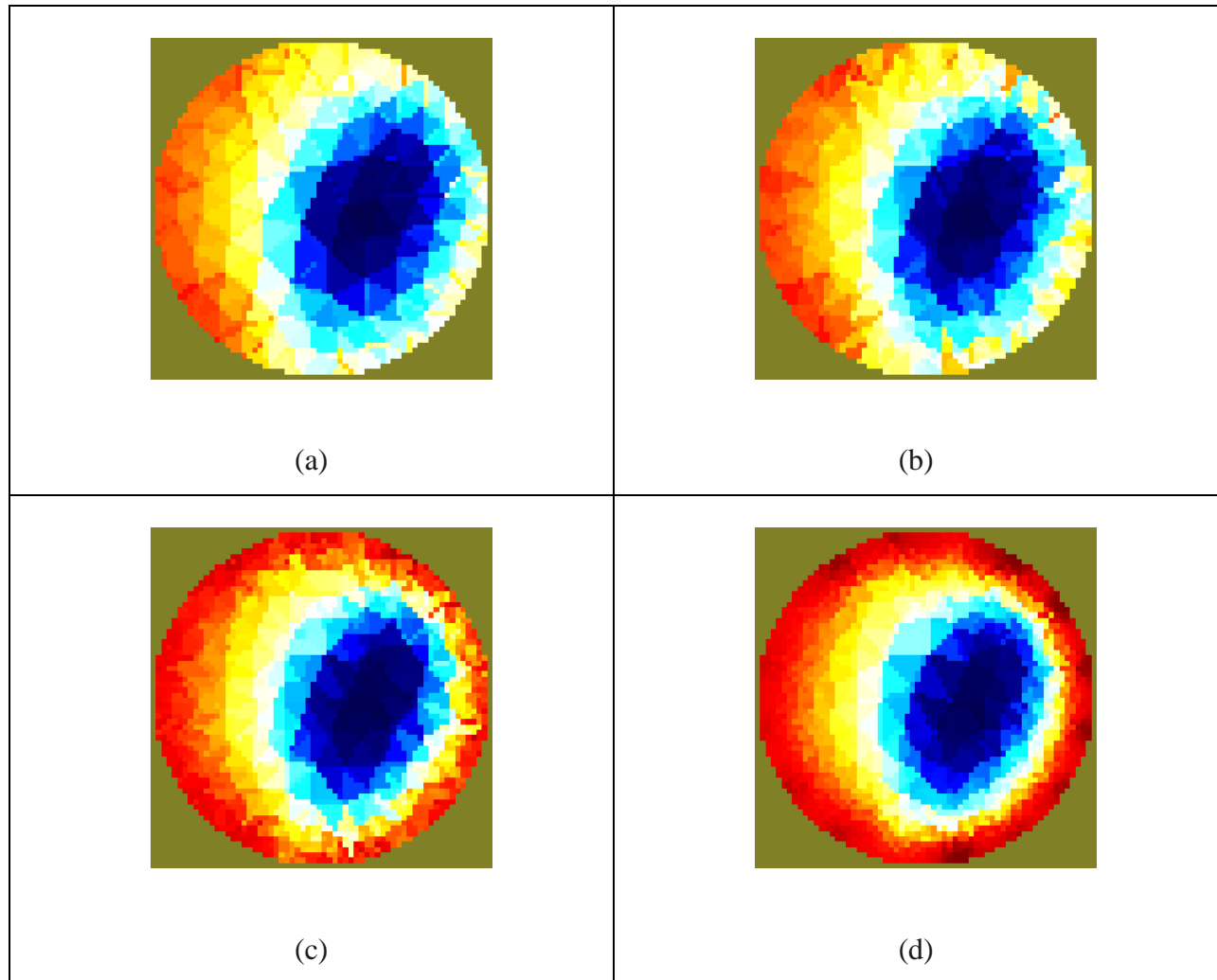


Figure 4.6: Reconstructed slices from the 1st experiment and *in phase* component V_x . Four cross-sections parallel to the electrode array plane in depth 0.2 cm (a), 0.6 cm (b), 1.2 cm (c) and 1.6 cm (d) from the top of the sample.

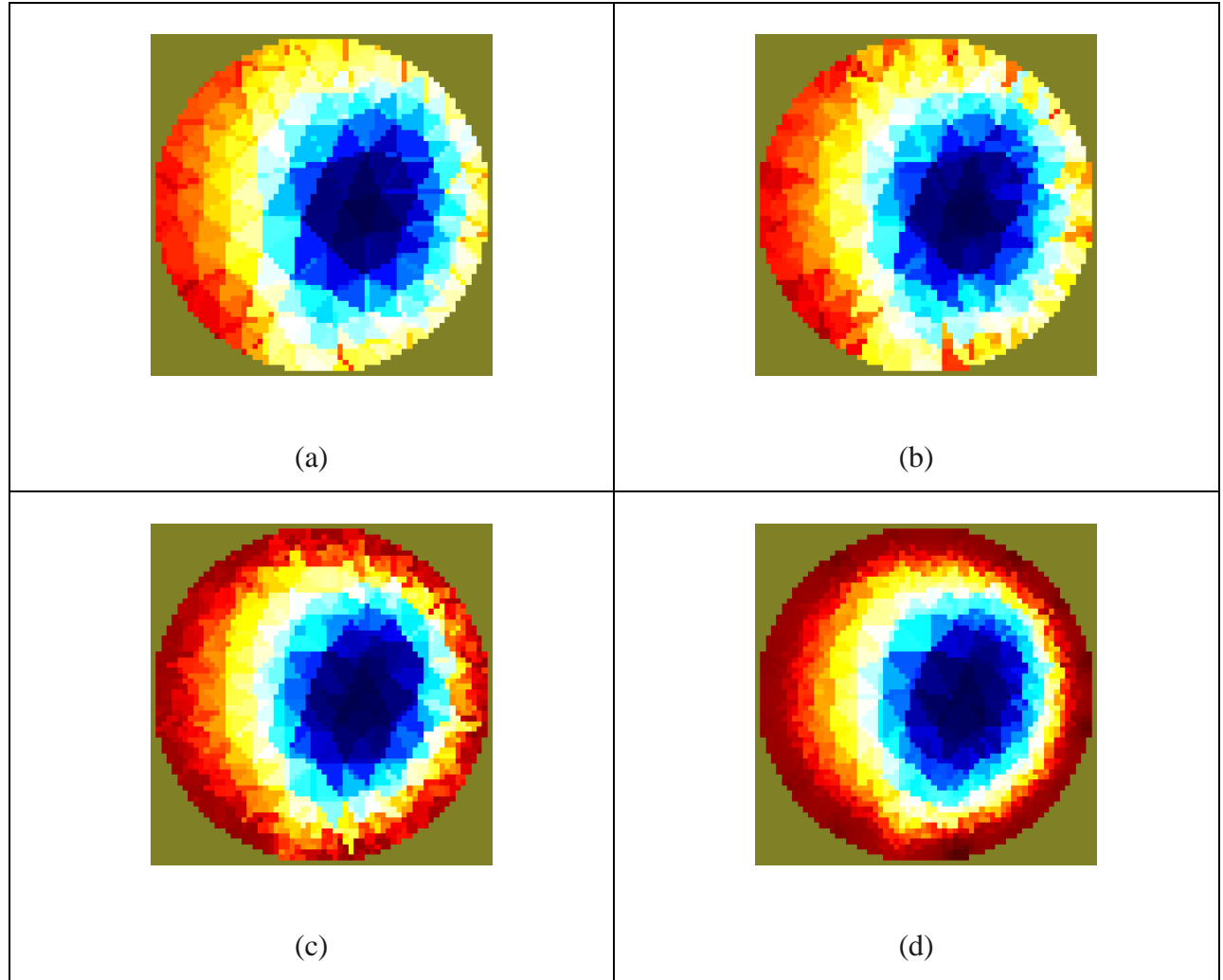


Figure 4.7: Reconstructed slices from the 1st experiment and *quadrature* component V_γ . Four cross-sections parallel to the electrode array plane in depth 0.2 cm (a), 0.6 cm (b), 1.2 cm (c) and 1.6 cm (d) from the top of the sample.

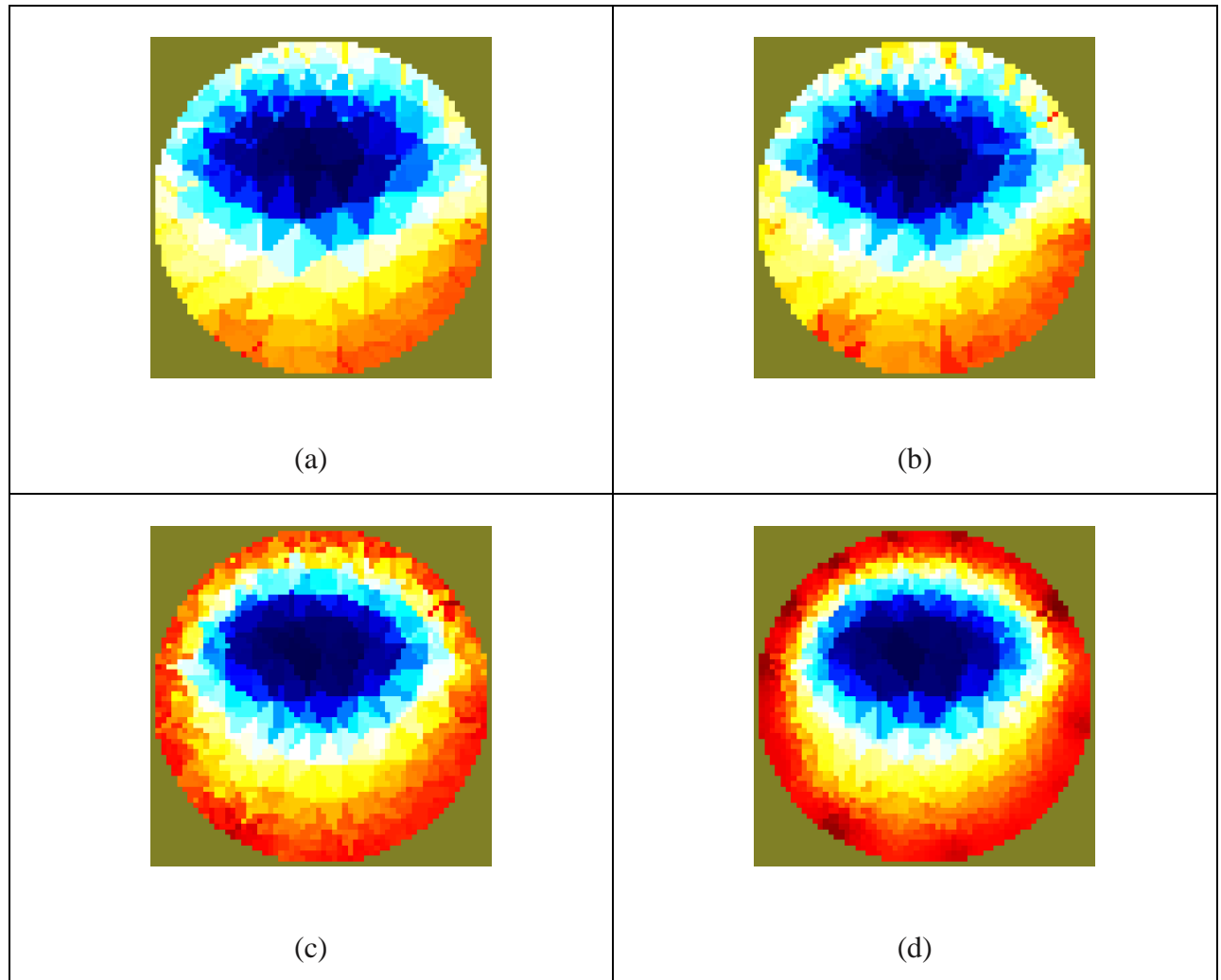


Figure 4.8: Reconstructed slices from the 2nd experiment and *in phase* component V_x . Four cross-sections parallel to the electrode array plane in depth 0.2 cm (a), 0.6 cm (b), 1.2 cm (c) and 1.6 cm (d) from the top of the sample.

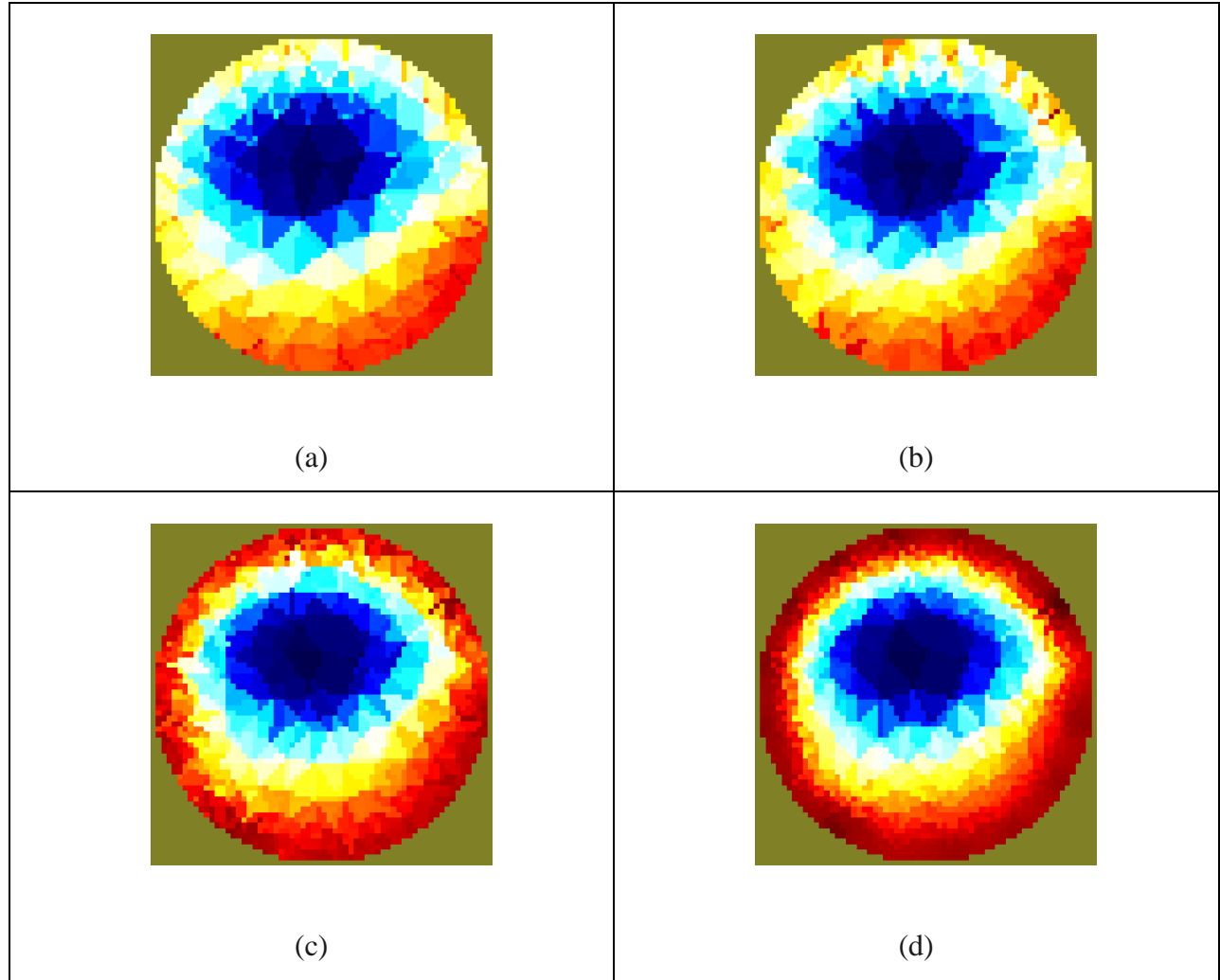


Figure 4.9: Reconstructed slices from the 2nd experiment and *quadrature* component V_q . Four cross-sections parallel to the electrode array plane in depth 0.2 cm (a), 0.6 cm (b), 1.2 cm (c) and 1.6 cm (d) from the top of the sample.

The white part of the tissue was present in each slides and changed sizes proceeding in depth realistically. These results underlined that: the EIT system was able to measure not only resistive component of the impedance, but also the capacitive ones; the NOSER algorithm was good even in solving three-dimensional case, with an excellent reconstruction time of 11 sec for 8044 elements of the spatially discretized FEM domain; the resistive and capacitive images visualized electrical properties of biological tissues with good contrast.

4.3 Human Sample: Skin

After validating the effectiveness of the EIT system as imaging modality with different conductivity objects and with in vitro tissue section experiments, I wanted to test it for producing *in vivo* images.

Connection of electrodes completely round the object to be measured is not always convenient for in vivo applications. In fact other configurations which do not completely surround the object may also be capable of giving useful images. One potential useful configuration is that of a linear array of electrodes, such as the probes I presented in figure 2.6 b in the chapter 2. In the literature I found that a planar electrode array geometry for measuring system is more convenient in use for certain applications than round electrode arrays. These could be mounted for example in an hand-held probe which could be placed against the body surface. Clinical application experience of electrical impedance tomography system [118] with 2D flat electrode system for 3D visualization has demonstrated the practical possibility to collect a meaningful data set.

As sample I chose the skin mainly because each parts of the body under study is protected by various layers of the skin and than because it has the potential to be visualized by EIT. Skin is a very interesting tissue because of its highly inhomogeneous structure, which thus leads to inhomogeneous dielectric properties. Generally, skin has three different layers: the epidermis, dermis, and subcutaneous tissue. The epidermis is the outer layer of skin. The thickness of the epidermis varies in different types of skin. It is the thinnest on the eyelids at 0.05 mm and the thickest on the palms and soles at 1.5 mm [119]. The epidermis contains different layers, but the one that defines its dielectric properties the most is the outermost layer, the stratum corneum. That layer is composed of dead, flat skin cells that shed about every two weeks. Although it is very thin (typically around 20 μm), it contributes a great deal to the dielectric properties of the skin. Its high resistivity makes skin one of the most resistive tissues in the human body. Its main function is protection of the body from the external environmental factors. The lower-lying layers, hence the rest of the epidermis (important in the immune response), the dermis (which gives firmness and elasticity), and the subcutaneous tissue (fat, connective tissue, larger blood vessels, and nerves), all have much lower resistivity.

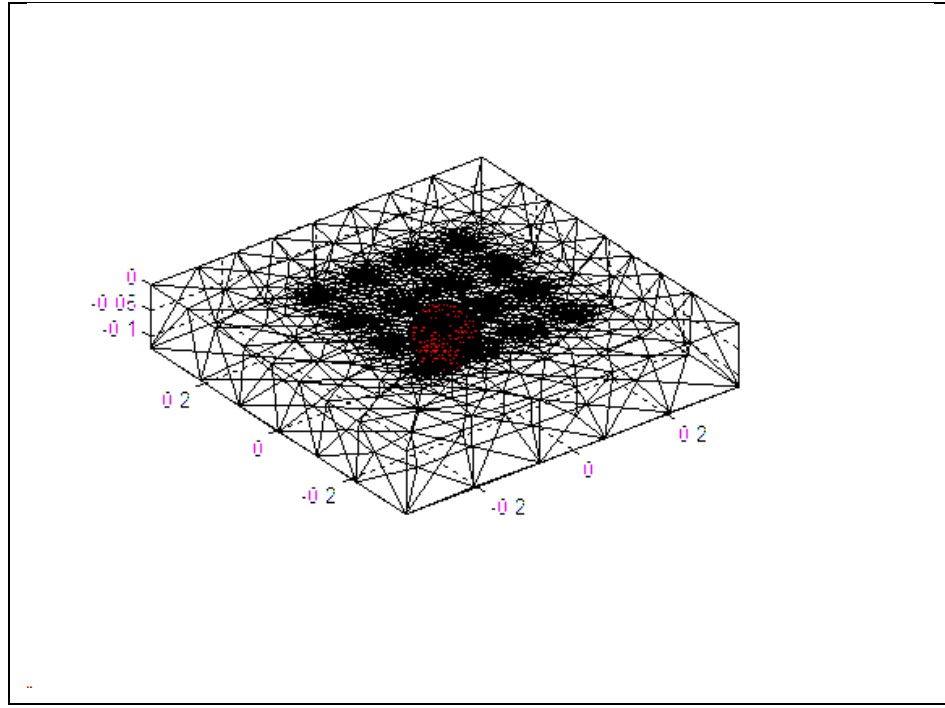
The objective of the following and last experiment was produce three-dimensional reconstruction of different layers of the skin based on its electrical properties. I expected to visualize different conductivity and permittivity layers. In this direction the usage of the planar array was fundamental in order to improve the resolution to at least $100\text{ }\mu\text{m}$, required as the results on imaging with the circular array showed very low resolution.

Simulation and experiment were performed to visualize reconstructed cross-sections until 1.2 mm from the flat surface of the electrode array. In the skin this distance comprehends stratum corneum and half the thickness of the epidermis.

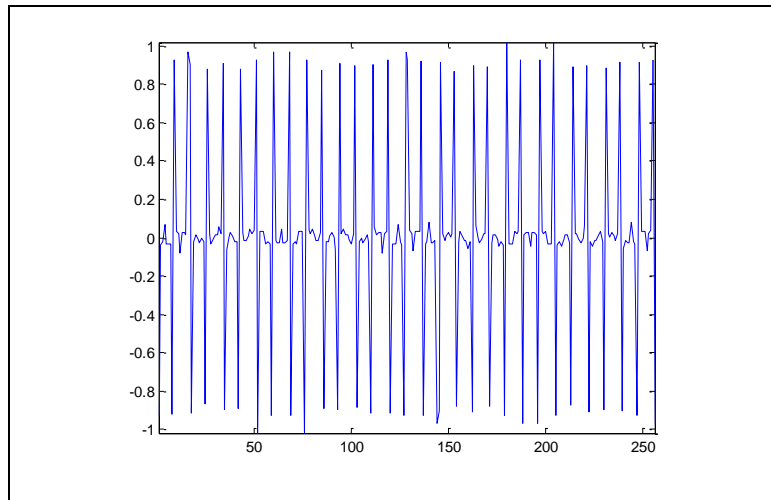
4.3.1 3D Imaging with Planar Electrode Array: Numerical Simulation

In this paragraph I present the first results of numerical simulation of the EIT system with a planar array of electrodes, which allows 3D visualization of the subsurface electric properties distribution. The goal was understand if the EIT system with the planar electrode array could yield three-dimensional images.

The simulation code used (appendix C.1.3) was similar to that of the tissue section experiment. It builds a three-dimensional parallelepiped mesh of the volume with 16 contacting electrodes on its surface, organized in 2D flat array, which was directly associated to the forward field of the inverse model. The 3D rectangular model was discretized into 8044 elements (figure 2.28, chapter 2) and the conductivity at each element was assumed isotropic and constant at 1 mS/cm . This mesh was used to solve the homogeneous voltages. For solving the inhomogeneous ones, I created the same model with a spherical inclusion of radius 0.6 mm and 1.5 mS/cm conductivity (figure 4.10 a). In a clinical perspective this different region of high conductivity could simulate, for example, cancerous tissue, that is reported to have higher conductivity than normal tissue [120, 121]. Naturally, the assumptions that the medium is both homogeneous and finite are very restrictive and unlikely to apply *in vivo*.



(a)



(b)

Figure 4.10: Simulation for testing the planar electrode array.

(a) 3D mesh with a sphere as a higher conductivity inclusion. (b) Inhomogeneous simulated voltages.

As one can notice the plot is coherent with the chosen stimulation and measurement method. This would be the scan in ideal case, without noise and errors.

A 3D image was successfully reconstructed from simulated data sets, and as one could notice in figure 4.11 the image represents a 3D spatial distribution of electrical properties with proper object size and position (central brown colored areas). The light-blue area on the surface of the electrode has dubious significance. The red and yellow parts outside the array correspond to the external elements of the domain.

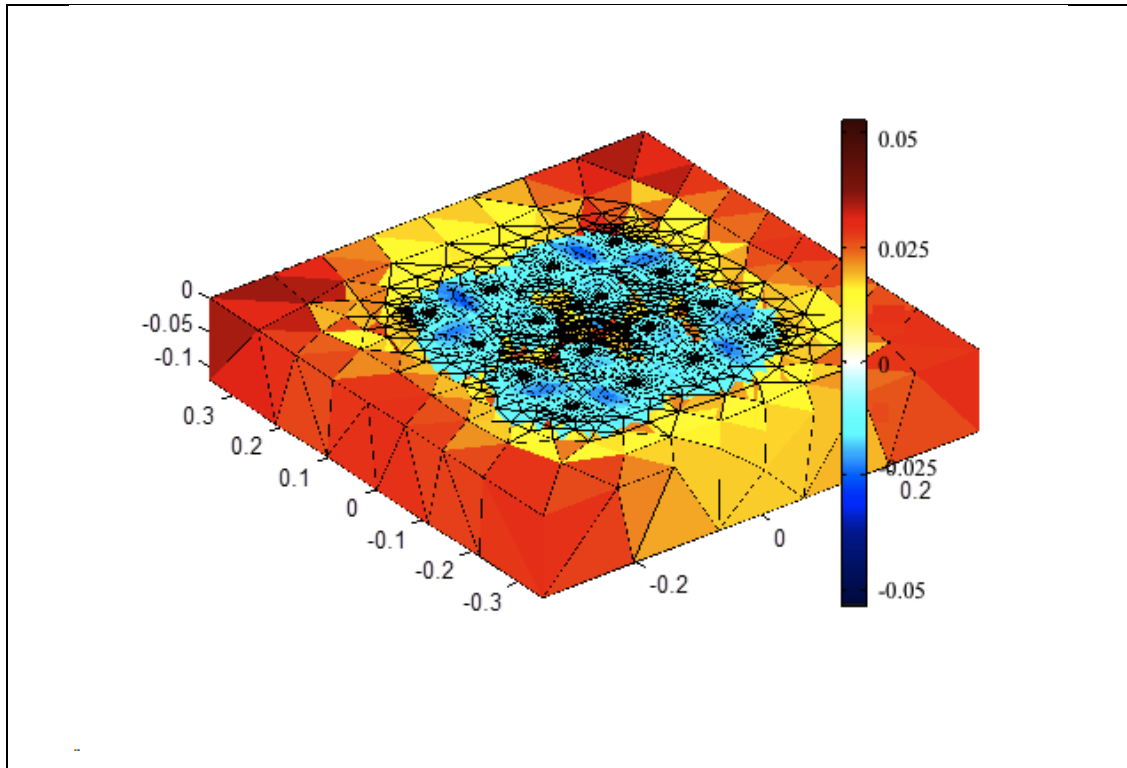


Figure 4.11: 3D image of the simulation code in appendix C.1.3, settling the *hyperparameter* value at 0.17.

The 3D distribution of conductivity is presented as a set of four 2D cross-sectional images with increasing depth. These resulting images are presented on figure 4.12.

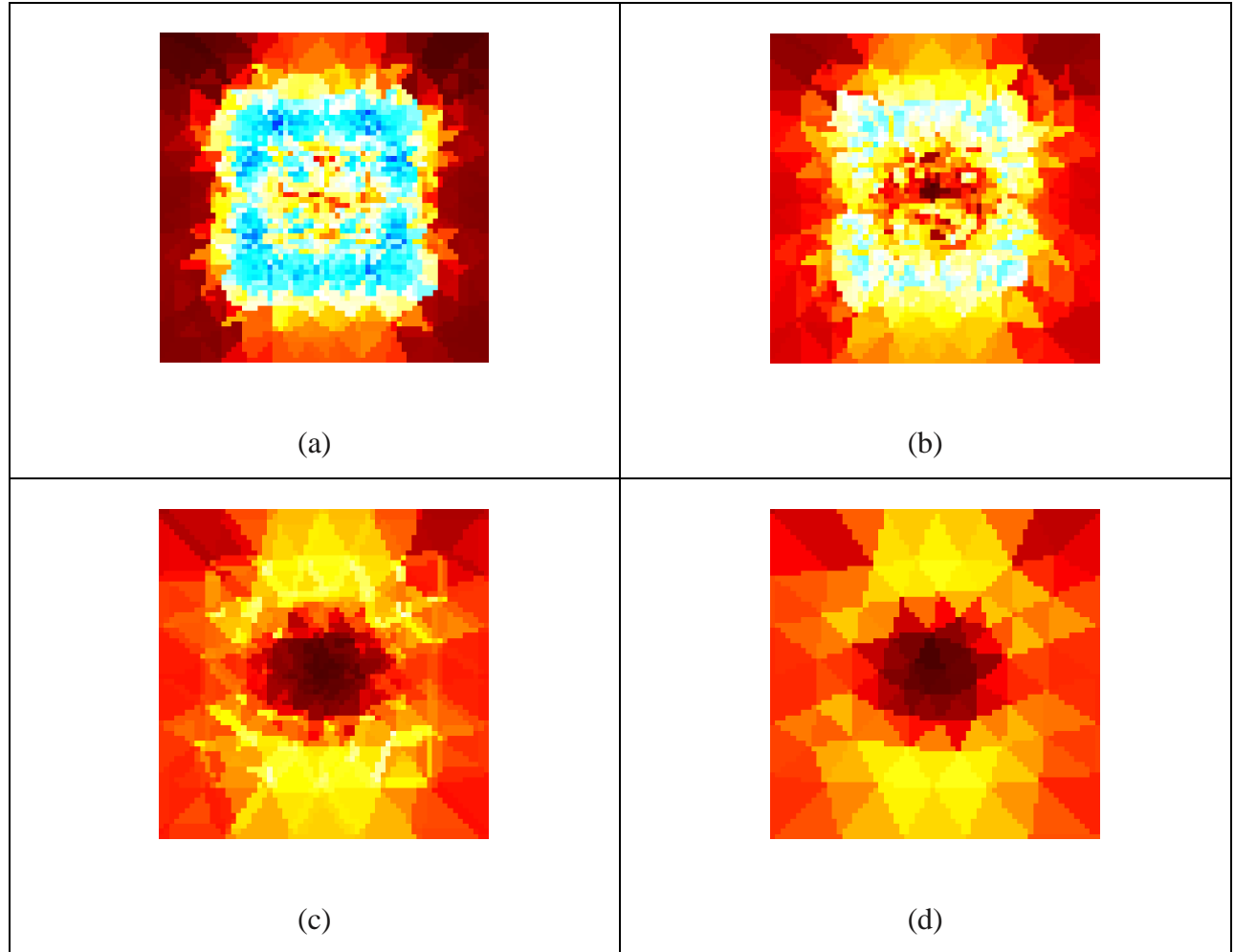


Figure 4.12: Reconstructed slices from the Simulation with planar electrode array. Four cross-sections parallel to the electrode array plane in depth $400\ \mu\text{m}$ (a), $600\ \mu\text{m}$ (b), $1\ \text{mm}$ (c) and $1.2\ \text{mm}$ (d) from the top of the phantom.

The sphere is identifiable on the images as red regions and it was visualized with different sizes along the deep, but light-blue colored lower conductivity regions are present in reconstruction until $600\ \mu\text{m}$ of depth.

Also in treating of 3D case with planar array, the NOSER algorithm managed to work and reconstruct the simulation, but specifically observing a vertical cross-section passing through the center of the phantom (figure 4.13) I concluded that the reconstruction was not accurate, because it did not reproduce well the sphere geometry and the light-blue areas over it were artifacts coming from the inverse solution with this planar configuration. From the literature I found some

comparisons between EIT systems with different electrodes organization [122]. It was shown that systems with round electrode organization provide images suitable for visual analysis, but system with planar electrodes organization reconstructs image with worse quality, sufficiently only for detection purposes. My results are consistent with this observation.

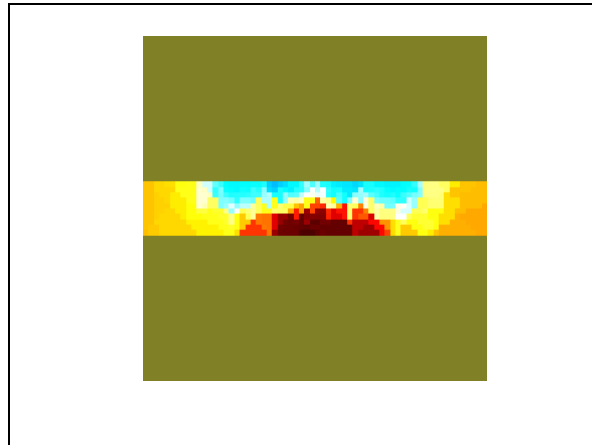


Figure 4.13: Reconstructed vertical slice.

From *in vivo* experiment on the skin, at best I could expect reconstructions with performance comparable with these results.

4.3.2 Skin Imaging

In vivo imaging of the skin was performed as the last experiment in this thesis. I preferred a peripheral part of the body, such as a finger. The planar electrode array was fixed and pressed against the finger, so it could well adhere to the skin (see figure 4.14). The experiment was performed twice on fingers of two different volunteers.

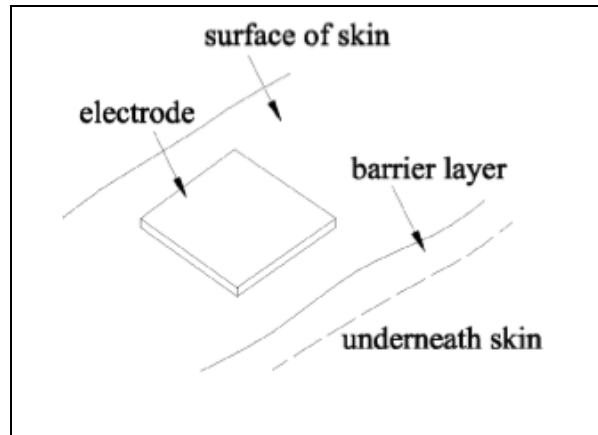


Figure 4.14: Planar electrode array on the skin.

As for the *in vitro* experiment of a tissue section, the acquisition code (appendix B.4) recorded only the inhomogeneous voltages, and for solving the inverse problem a zero matrix was used as the homogeneous background to perform the difference reconstruction. Even though I was treating biological samples, unexpectedly the system recorded only significant *in phase* components of the boundary voltages, so that purely resistive images were obtained.

The reconstruction code in appendix C.2.4 was substantially the same as the simulation code (appendix C.1.3), differing in experimental data loading protocol only. The reconstructed conductivity map was imaged as average of the calculated conductivity.

Figures 4.15 a and b, c and d show the acquired data plot and the 3D reconstruction calculated with data from both the experiments.

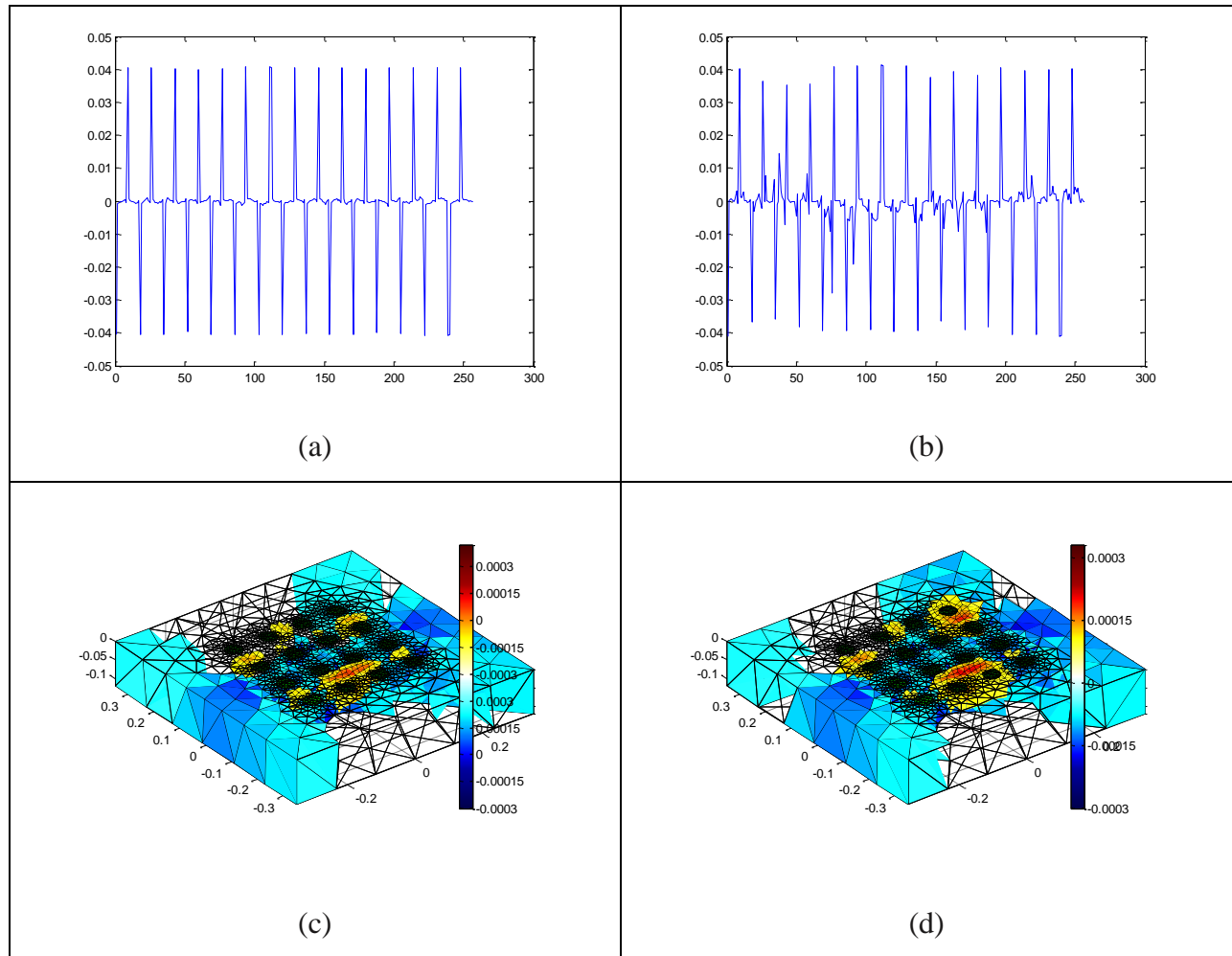
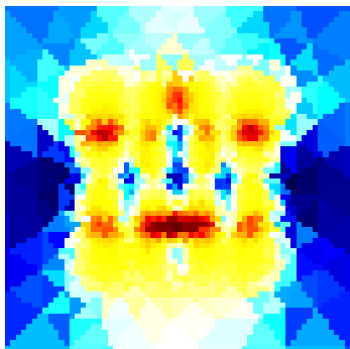


Figure 4.15: Acquired inhomogeneous data set and 3D reconstructions of the skin with excitation 100 mV at 10 KHz: (a, c) Results of the first experiment settling the *hyperparameter* value at 13, (b, d) results of the second experiment settling the *hyperparameter* value at 13. For both the experiments the reconstruction time was 11 seconds.

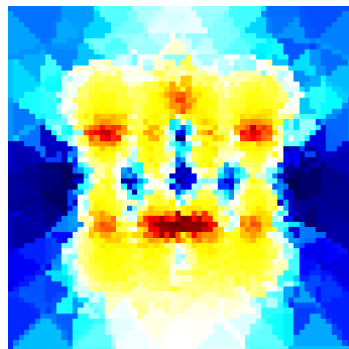
It could be easily noticed that data coming from the first experiment were less accurate, with much smaller signals.

The reconstructed images presented the same features as from the simulation: a superficial yellow area was present, time corresponding to a lower conductivity.

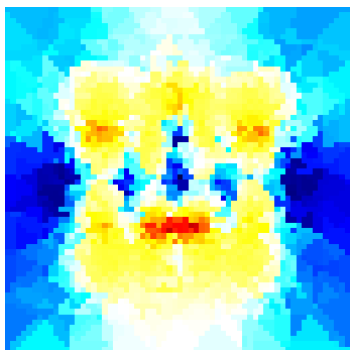
Ten cross-sections, illustrated in figure 4.16 and 4.17, represent the obtained conductivity map.



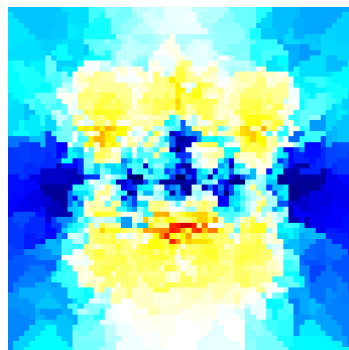
(a)



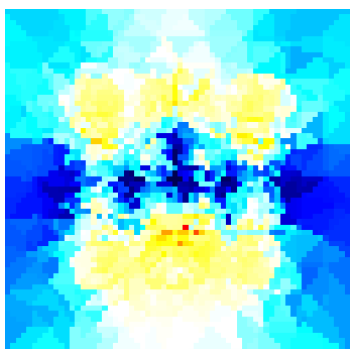
(b)



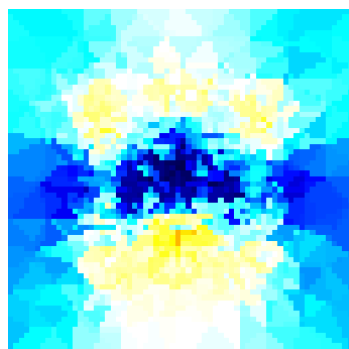
(c)



(d)



(e)



(f)

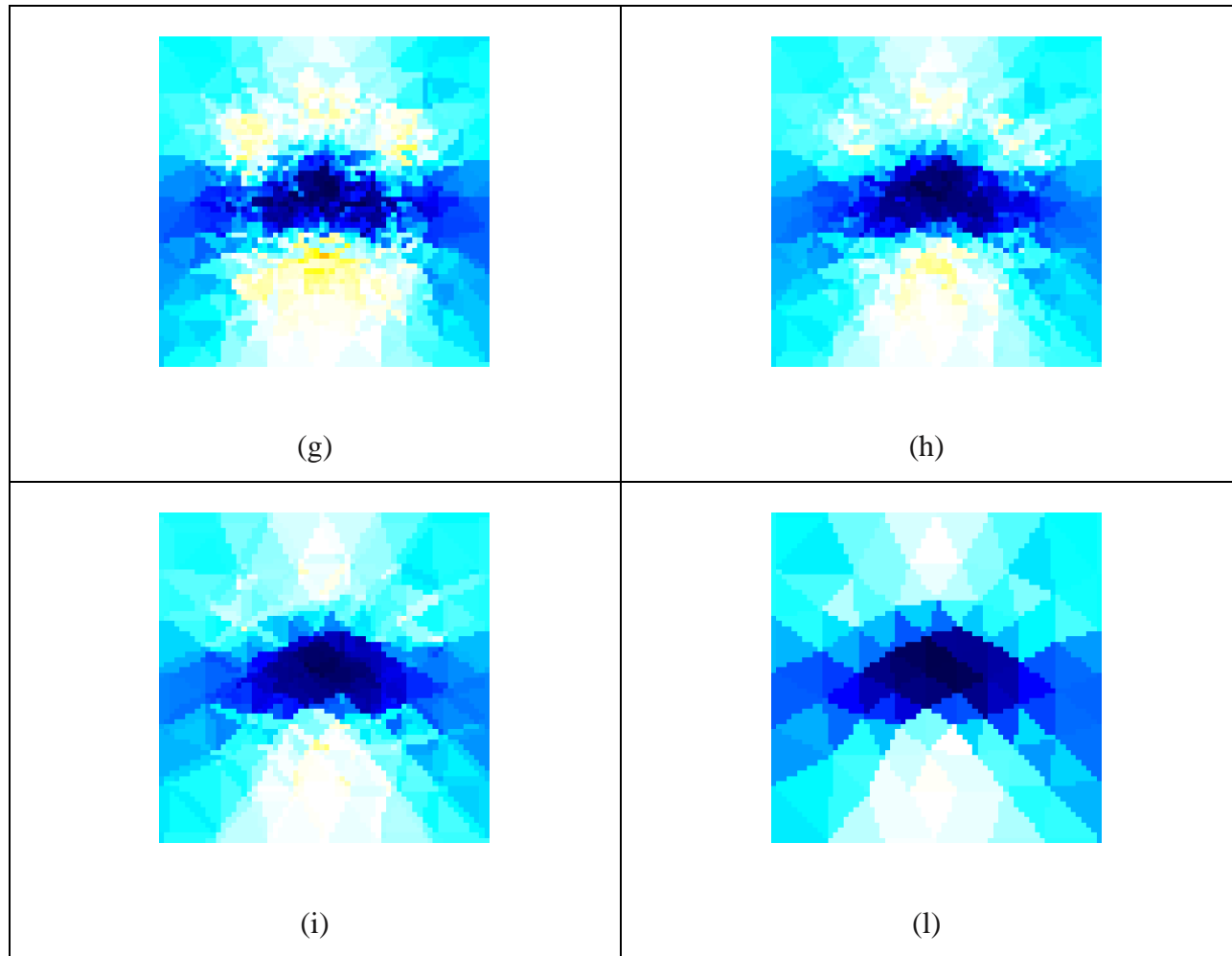
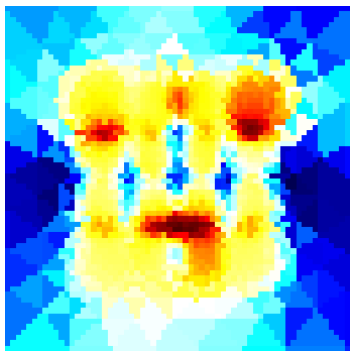
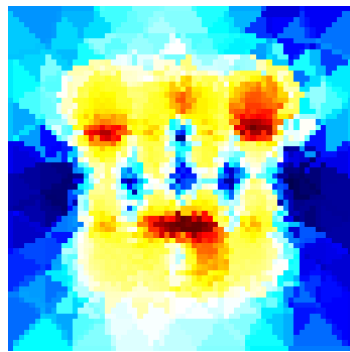


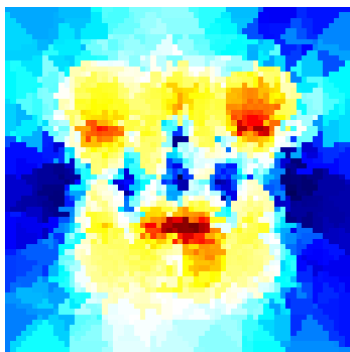
Figure 4.16: Reconstructed slices from in vivo 1st experiment on the skin. Ten cross-sections parallel to the electrode array plane on the surface (a) and in depth 100 μm (b), 200 μm (c), 300 μm (d), 400 μm (e) 500 μm (f), 600 μm (g), 800 μm (h), 1 mm (i) and 1.2 mm (l) from the top of the skin.



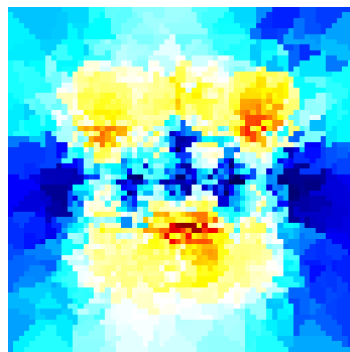
(a)



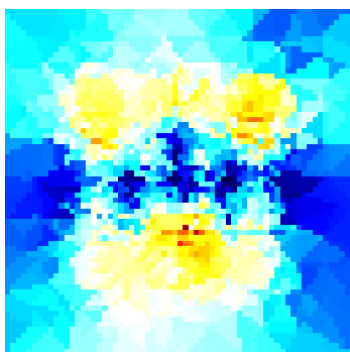
(b)



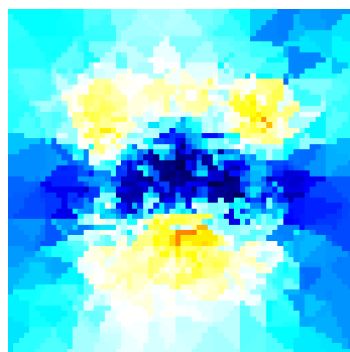
(c)



(d)



(e)



(f)

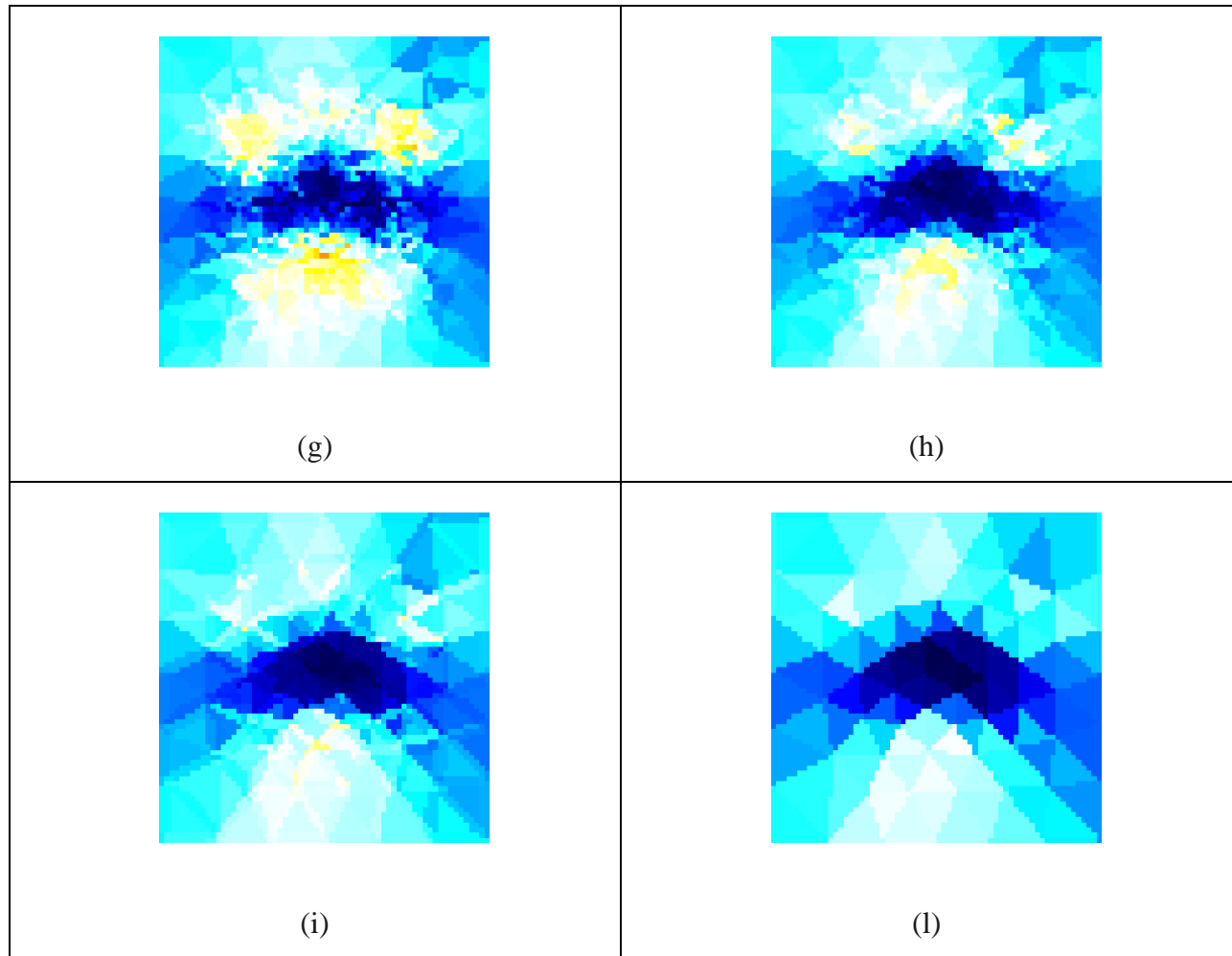


Figure 4.17: Reconstructed slices from in vivo 2nd experiment on the skin. Ten cross-sections parallel to the electrode array plane on the surface (a) and in depth 100 μm (b), 200 μm (c), 300 μm (d), 400 μm (e) 500 μm (f), 600 μm (g), 800 μm (h), 1 mm (i) and 1.2 mm (l) from the top of the skin.

As one could notice the blue regions became more consistent increasing the depth, where, instead, the yellow regions rapidly disappeared. That meant on the whole that, at a 500-600 [km] depth the conductivity incremented, as it was expected from signals coming from deeper layers of the skin.

On a vertical cross-section (fig. 4.18 a and b) the superficial areas were less conductive than the underlying regions, as expected.

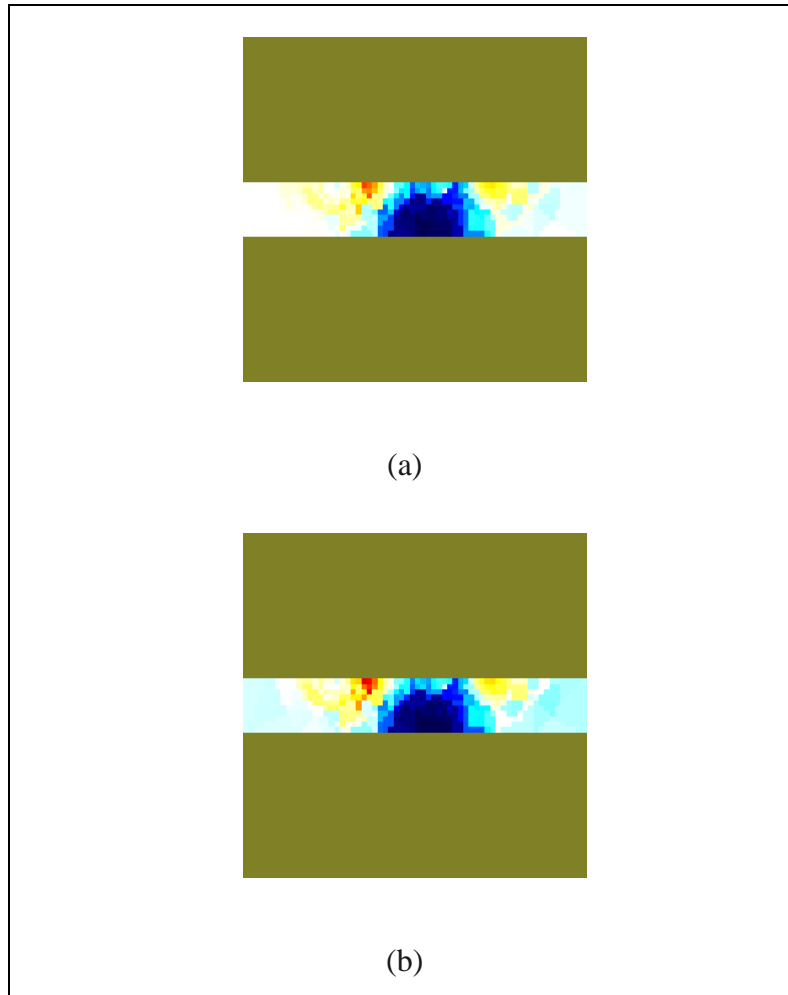


Figure 4.13: Reconstructed vertical slice for the 1st experiment (a) and the 2nd experiment (b).

The fact that in-vivo data with the planar array yielded images of good contrast is encouraging. However in these images, the various layers of the skin were not identifiable. They only visualized less conductive area on the surface of the phantom and a conductive region under that. I concluded that the inverse solver was not accurate for the inverse solution of the planar array configuration.

These results, I found, could be related with others works in the literature [123]: in fact it known that especially in the low-frequency range (under and around 10 kHz), the impedance of skin is dominated by the stratum corneum even though this layer is very thin. Studies show that, for frequencies of 10 kHz, the share of stratum corneum in the total impedance of skin is around 50% [123], but at 100 kHz drops to around 10% [124]. Human skin has high impedance problems associated with stratum corneum, which lead to measurement uncertainty.

Another common difficulty in medical EIT is due to inaccurately known electrode-skin contact impedances. The electrode-skin contact impedances are due to an electrochemical effect at the electrode-skin interface and they cause a drop to the measured voltage at each electrode. The contact impedances depend on the thickness and properties of the skin and may be different for each electrode-skin interface. The systematic reconstruction errors that are caused by inaccurately modeled contact impedances have been studied with simulations and experiments in [125] and [126], and the errors are found to be severe. These reconstruction errors can partially be avoided by considering the contact impedances as unknown parameters in the image reconstruction.

With the planar electrode array there are many remaining problem, particularly those arising from the difficulties of making consistent electrode contacts to the skin and the image-reconstruction problems associated with spatial nonlinearities and the utilization of three-dimensional data.

Chapter 5

Conclusions

This Thesis project has achieved the goal of developing both of the hardware and the software of an Electric Impedance tomography (EIT) system, and to test its performance on phantoms and on biological model systems.

The EIT hardware performance was analyzed as for the effects of systematic errors, with particular reference to stray capacitance, typical of analog multiplexed sensors. By relying on a high-end Lock-in Amplifier, high accuracy in discriminating *in-phase* and quadrature components of the voltages has been achieved. At the frequency of 10 KHz, employed in the measurements after preliminary testing, parasitic capacitance, electrode polarization effects were found to be minor, and systematic errors due to channel crosstalk have been shown not to interfere with image interpretation

EIT imaging has been implemented using the EIDORS software platform, to solve the image reconstruction problem (intrinsically mathematically ill-posed) successfully in a time range from 3 to 11 seconds on an ordinary PC, with accurate positional rendering of impedance inhomogeneity in the samples. In particular:

- 1) The regularization method applied (NOSER) was able to obtain 2D resistivity distributions when treating the isotropic case of objects with extreme electrical properties, even with the addition of numerical noise and errors. Though images artifacts, attributed to the ill-posedness of the problem, have been observed, they did not interfere with the visualization of the object under study.
- 2) The resistive and capacitive 3D images of actual tissue sections imaged with circular electrode arrays clearly reflected the anisotropic property of the samples.
- 3) The *in vivo* images of the skin, imaged with a planar electrode array, reconstructed areas with low conductivity and deeper areas of high conductivity, coherently with the property of

the layers of the skin. The image resolution was shown, with the electrode configuration employed, to be insufficient for the visualization of skin stratifications.

In conclusion, the EIT system has been shown to be a very promising non-invasive method for biomedical applications, and even a simple yet performant system, such as implemented, was able to accurately measure the properties of the model domains subject to the study.

Chapter 6

Future Works

Today, impedance measurements provide an important method for the noninvasive investigation of the tissue structure and properties for some very useful applications based on the measurements of the differences in the specific conductivity or permittivity.

EIT systems suitable for *in vivo* imaging are complex systems requiring several closely interacting hardware and software parts for obtaining a *real-time* technology. Many modifications have to be made to any part of the system: if very much more rapid data collection is required, then parallel data collection of the potentials must be used and more information may be obtained recording the response at multiple frequencies. To save time, different frequencies may be injected simultaneously through any one electrode injection pair according with the frequency-division multiplexing method, where orthogonal frequencies are injected simultaneously to speed up measurement time. The Lock-in amplifiers working in frequency need to be redesigned in order to receive several channels simultaneously

The described EIT system, with due changes both in the hardware and in the software, has potential applications to localized tissue imaging and imaging of organs. The quality of the contrast in the images strongly suggests that EIT may provide a low-cost, portable, safe imaging system in the near future. It is possible that the mapping of electrical properties of tissue may be used in conjunction with other imaging modalities to achieve high specificity for accurate characterization.

In planning future work, we estimated that the system can be used in intensive *in vivo* experiments of parts of the human body. The objective could be the tissue characterization by simultaneous analysis of the conductivity and permittivity values, considering the total impedance parameter. In this direction the reconstruction software must be rewritten in a more useful code that works directly with the impedance value. An essential next step is perfecting the 3D reconstruction and improving the planar electrode array, since its geometry emerges as a

recommended strategy for clinical use. In further research more electrodes in the system should be used to obtain images with higher quality. Since the electrical information given by EIT is distorted by the thin highly resistive layer of the skin (the stratum corneum), a low-contact-impedance approach must be defined, e.g., by using micromachined needle electrodes that can be studied to decrease measuring uncertainty. Microneedles could be designed to penetrate into the skin through the stratum corneum to the epidermis. At these depths (20-100 μm) the insertion would be painless because the needles will not reach the upper nerve cells, and minimally invasive and traumatic to skin because the dimension of microneedles would be small enough not to allow significant continuity disruption.

In another direction, the object of tomography can be extended to micro tissue, such as a cell, to realize micro imaging. Since even small errors in the electrode-sample contact impedance can cause large systematic artifacts in the reconstructed images besides the presence of systematic errors due to the crosstalks, which are the major problem for the applicability and robustness of EIT, a novel image reconstruction method should be proposed, taking into account both systematic errors. Were these corrections to be implemented, we expect that the probe and the method can significantly improve the applicability and robustness of EIT.

References

- [1] D.C. Barber and B.H. Brown, *Applied potential tomography*, J. Phys. E. Sci. Instrum., vol.17, pp.723-733, 1984.
- [2] Lionheart, W. R. B., *EIT and Diffuse Optical Tomography Reconstruction Software (EIDORS)*, 2002.
- [3] Margaret Chenevy, David Isaacson, Jonathan C. Newelly, *Electrical Impedance Tomography*, SIAM Review, vol. 41, n.1, pp.85, 1999.
- [4] W. D. Hou et al., *Increasing image resolution in electrical impedance tomography*, *Electronics Letters*, Vol.38, pp.701-702, 2002.
- [5] Cherepenin, V.A. et al., *Three-dimensional EIT Imaging of Breast Tissue: System Design and clinical Testing*. IEEE Transactions on Medical Imaging (2002), n. 21, 662-667.
- [6] W. R. B. Lionheart, *EIT reconstruction algorithms: pitfalls challenges and recent developments*, *Physiol. Meas.*, 2004, Vol. 25, pp. 125-142.
- [7] Fricke H., Morse S., *The electric capacity of tumors of the breast*. *Cancer Research* 1926, 16, 340-376.
- [8] Nyboer J., *Electrical impedance plethysmography: a physical and physiologic approach to peripheral vascular study*. 1950, 2:811-821.
- [9] Henderson, R. P. and Webster, J.G., *An Impedance Camera for Spatially Specific Measurements of the Thorax*. IEEE Transactions on Biomedical Engineering (1987), 25, 240-254.
- [10] King, W. , *Electricity in Medicine and Surgery*. New York; Boericke and Runyon; 1901.
- [11] Barber, C.C. and Brown, B.H., *Imaging Spatial Distribution of Resistivity using Applied Potential Tomography*. *Electronics Letters* (1983), 19, 933-935.
- [12] Brown, B.H., *Electrical Impedance Tomography (EIT): A Review*. *Journal of Medical Engineering and Technology* (2003), 27, 97-108.
- [13] R.A. Williams and M.S.Beck, *Process tomography: principles, techniques and applications*, Butterworth-Heinemann, Oxford, 1995.
- [14] *Reconstruction algorithms for permittivity and conductivity imaging*, Proceedings of the 2nd congress on industrial process tomography (2001), 4-11.

- [15] O.Dorn, E.Miller, and C.Rappaport, *A shape reconstruction method for electromagnetic tomography using adjoint fields and level sets*, Inverse Problems (1999), n.6, 1523-1558.
- [16] M.Betrero and P.Boccacci, *Introduction to inverse problems in imaging*, IoP, Bristol, 1998.
- [17] H.X. Wang and Z. Cao, *An investigation of nonlinearity of 'soft' field in electrical impedance tomography system, based on statistical methods*, Instrumentation and Measurement technology Conference 2005, Ottawa, Canada, pp. 713-717.
- [18] W.Q. Yang, *Editorial*, Meas. Sci. Techno., 2001, Vol.12.
- [19] G.J.Saulnier, R. S. Blue, J. C. Newell, D. Isaacson , and P. M. Edic, *Electrical impedance tomography*, IEEE Signal Process. Mag., 2001, Vol. 18, n.6, pp. 31-43.
- [20] L. A. Geddes and L. E. Baker, *The specific resistance of biological material – a compendium of data for the biomedical engineer and physiologist*, Med. and biol. Eng., vol. 5, pp. 271–293, 1967.
- [21] A. J. Surowiec, S. S. Stuchly, and et al., *Dielectric properties of breast carcinoma and the surrounding tissues*, IEEE Transactions on Biomedical Engineering, vol. 35, pp. 257–263, 1988.
- [22] Y. Zou and Z. Guo, *A review of electrical impedance techniques for breast cancer detection*, Medical Engineering and Physics, vol. 25, no. 2, pp. 19–90, 2003.
- [23] A. Adler and R. Guardo, *Electrical impedance tomography: Regularized imaging and contrast detection*. IEEE Trans Med Imaging, vol. 15, pp. 170–179, 1996.
- [24] A. Adler, R. Guardo, and Y. Berthiaume, *Impedance imaging of lung ventilation: Do we need to account for chest expansion?*, IEEE Trans. Biomed. Eng., vol. 43, no. 4, pp. 414-420, 1996.
- [26] R. J. Sadleir and R. A. Fox, *Detection and quantification of intraperitoneal fluid using electrical impedance tomography*, IEEE Trans Biomed Eng., vol. 48, no. 4, pp. 484–491, 2001.
- [27] B. Blad and B. Baldetorp, *Impedance spectra of tumor tissue in comparison with normal tissue; a possible clinical application for electrical impedance tomography*, Physiological Measurements, vol. 17 (Suppl A), pp. A105–A115, 1996.
- [28] A. Hartov, P. LePivert, N. Soni, and K. Paulsen, *Using multiple-electrode impedance measurements to monitor cryosurgery*, Medical Physics, vol.19, n.12, pp. 2806-2814, 2002.
- [29] D. M. Otten, G. Onik, and B. Rubinsky, *Distributed network imaging and electrical impedance tomography of minimally invasive surgery*, Technolog in Cancer Research & Treatment, vol. 3, no. 2, pp. 125–134, April 2004.

- [30] M.T. Clay and T. C. Ferree, *Weighted regularization in electrical impedance tomography with applications to acute cerebral stroke*, IEEE Trans. Med. Imag., vol 21, n.6, pp.629-637, 2002.
- [31] S. Zolchiver, M. M. Radai, M. Rosenfeld, and S. Abboud, *Induced current impedance technique for monitoring brain cryosurgery in a two-dimensional model of the head*, Annals of Biomedical Engineering, vol. 30, no. 9, pp. 1172– 1180, 2002.
- [32] R. A. Erol, P. Cherian, R. H. Smallwood, B. H. Brown, and K. D. Bardhan, *Can electrical impedance tomography be used to detect gastro-oesophageal reflux?*, Physiological Measurements, vol. 17, pp. A141–A147, 1996.
- [33] S. Meeson, A. L. T. Killingback, and B. H. Blott, *The dependence of EIT images on the assumed initial conductivity distribution: a study of pelvic imaging*, Physics in Medicine and Biology, vol. 40, pp. 643–657, 1995.
- [34] C. Mitchell, J. Rose, B. FAMILONI, S. Winters, and F. Ling, *The use of multi- frequency bioelectrical impedance analysis to estimate fluid volume changes as a function of the menstrual cycle*, Basic Life Sci., vol. 60, pp. 189–191, 1993.
- [35] R. Brini, A. Brusco, M. Massari, and C. Pallotti, *The electrical resistance and impedance of mammalian muscles during the first days after slaughtering. II: femoral biceps of swine*, Boll Soc Ital Biol Sper, vol. 56, no. 15, pp. 1580–4, 1980.
- [36] T. C. Ferree, K. J. Eriksen, and D. M. Tucker, *Regional head tissue conductivity estimation for improved EEG analysis*, IEEE Transactions on Biomedical Engineering, vol. 47, no. 12, pp. 1584–1592, December 2000.
- [37] S. Gonçalves, J. C. de Munck, J. P. A. Verbunt, F. Bijma, R. M. Heethaar, and F. L. Da Silva, *In vivo measurement of the brain and skull resistivities using an EIT-based method and realistic models for the head*, IEEE Transactions on Biomedical Engineering, vol. 50, pp. 754–767, June 2003.
- [38] C. G. Xie, S. M. Huang, B. S. Hoyle, and M. S. Beck, *Tomographic imaging of industrial process equipment development of system model and image reconstruction algorithm for capacitive tomography*, in Sensors & their Applications, vol. V, no. 203-208, Edinburgh, September 1991.
- [39] R. A. Williams and M. S. Beck, *Process Tomography: Principles, Techniques and Applications*. Oxford: Butterworth-Heinemann, 1995.
- [40] K. A. Dines and R. J. Lytle, *Analysis of electrical conductivity imaging*, Geophysics, vol. 46, pp. 1205–1036, 1981.
- [41] L. Parker, *The inverse problem of resistivity sounding*, Geophysics, vol.42, pp. 2143-2158, 1984.

- [42] A. Ramirez, W. Daily, D. LaBrecque, E. Owen, and D. Chesnut, *Monitoring an underground steam injection process using electrical resistance tomography*, Water Resources Research, vol. 29, pp. 73–87, 1993.
- [43] A. Ramirez, W. Daily, A. Binley, D. LaBrecque, and D. Roelant, *Detection of leaks in underground storage tanks using electrical resistance methods*, Environmental and Engineering Geophysics, vol. 1, pp. 189–203, 1996.
- [44] W. Daily and A. Ramirez, *Electrical resistance tomography during in-situ trichloroethylene remediation at the savannah river site*, Applied Geophysics, vol. 33, pp. 239–249, 1995.
- [45] M. R. Eggleston, R. J. Schwabe, D. Isaacson, and L. F. Coffin, *The application of electric current computed tomography to defect imaging in metals*, in Progress in Quantitative NDE, D. Thompson and D. Chimenti, Eds., Plenum, New York, 1989.
- [46] K. R. Backe, O. B. Lile, and S. K. Lyomov, *Characterizing curing cement slurries by electrical conductivity*, in SPE 68th Annual Western Regional Meeting, Bakersfield, CA, USA, May 1998.
- [47] David M. Otten, Ph.D. Gary Onik, *Distributed Network Imaging and Electrical Impedance Tomography Of Minimally Invasive Surgery*, Technology in Cancer Research & Treatment, ISSN , Vol.3 n.2, 2004.
- [48] B. H. Brown, D. C. Barber , and A.D. Seagar, *Applied potential tomography: possible clinical applications*, Clin. Phys. Physiol. Meas., 6, pp. 109–121, 1985.
- [49] H. Ross, B. J. W. Chow, A. Adler, *EIT measurement of heart and lung perfusion*. Oxford, Ottawa, Ontario, 2003.
- [50] Li Z., Xu L., W. J., L.X. , G.Y., *Modeling The Electrical Characteristics of the Stomach and Reconstruction Image*, Intern. Conf. on Comp. Applic. and System Modeling, 2010.
- [51] Y. Z. Ider and O. Birgul, *Use of the magnetic field generated by the internal distribution of injected currents for electrical impedance tomography (mr-eit)*, ELEKTRIK, vol. 6, no. 3, pp. 215–225, 1998.
- [52] O. Kwon, E. J. Woo, J. R. Yoon, and J. K. Seo, *Magnetic resonance electrical impedance tomography (mreit): Simulation study of the j-substitution algorithm*, IEEE Transactions on Biomedical Engineering, vol. 49, pp. 160–167, 2002.
- [53] Nuo Gao and Bin He, *Noninvasive imaging of Bioimpedance Distribution by Means of Current Reconstruction Magnetic Resonance Electrical Impedance Tomography*, IEEE, Trans. on Biomedical Engineering, vol.55, n. 5, may 2008.

- [54] K.Okazaki, A.Tangoku, T. Morimoto, R. Kotani, *Basic study of a diagnostic modality employing a new electrical impedance system (EIT) method for noninvasive measurement in localized tissues*, *The Journal of Medical Investigation*, vol.57, 2010.
- [55] M. Dolgin and P. D. Einziger, *WKB Quasistatic Reconstruction of Layered Biological Tissues*, Proceedings of the 26th Annual International Conference of the IEEE EMBS, San Francisco, CA, USA, September 2004.
- [56] Manuel Gasulla and Ramon Pallas-Areny, *Noniterative Algorithms for Electrical Resistivity Imaging Applied to Subsurface Local Anomalies*, IEEE Sensors Journal, vol.5, n.6, 2005.
- [57] Ran Liu, Jing Liu, Guangzhi Wang, Hui Ding, *Minimally Invasive Electrical Impedance Tomography- Promising Way to Decrease Diagnostics Uncertainty*, Proceedings of the 1st IEEE International Conference on Nano/Micro Engineered and Molecular System, Zhuhai, China, pp.18-21, 2006.
- [58] Liston AD, *Models and image reconstruction in electrical impedance tomography of human brain function*, PhD Thesis, Middlesex University, London 2004.
- [59] U. Pliquet and J. C. Weaver, *Electroporation of human skin: simultaneous measurement of changes in the transport of two fluorescent molecules and in the passive electrical properties*. Bioelectrochem. Bioenerget. 1996; 39:1–12.
- [60] PhD Thesis, Nicholas Polydorides, *Image reconstruction algorithms for soft-field Tomography*, University of Manchester, United Kingdom, September 2002.
- [61] U.Pliquet and J. C. Weaver, *Electroporation of human skin: simultaneous measurement of changes in the transport of two fluorescent molecules and in the passive electrical properties*, Bioelectrochem. Bioenergt., 1996, vol.39, pp.1-12.
- [62] H. C. Burgher, R. van Dongen, *Specific electric resistance of body tissue*, Phis.Med. Biol., 1960, n.5, 431-447.
- [63] Molinari, M., 2003, *High Fidelity Imaging in Electrical Impedance Tomography*, Ph.D. dissertation, University of Southampton, Southampton, United Kingdom.
- [64] P. Hua, J. G. Webster, and W. J. Tompkins, *A regularised electrical impedance tomography reconstruction algorithm*, Clin. Phys. Physiol. Meas., vol. 9, pp. 137–141, 1988.
- [65] PhD. Thesis, *3-D Electrical Impedance Tomography for Domains with a Piecewise Constant Conductivity*, Northeastern University, Boston, Massachusetts, January 2006.
- [66] A. Allers and F. Santosa, *Stability and resolution analysis of a linearized problem in electrical impedance tomography*, Inverse Problem 7, 1991, pp. 515-535.

- [67] D.C. Barber and B.H. Brown, *Errors in reconstruction of resistivity images using a linear reconstruction technique*, Clinical Physics and Physiological Measurement **9**, 1998, pp.101-104.
- [68] R.S. Blue, *A real time three-dimensional linearized reconstruction algorithm generalized for multiple planes of electrodes*, PhD. Thesis, Rensselaer Polytechnic Institute, Troy, 1997.
- [69] A. Calderón, *On an inverse boundary value problem*, in Seminar on Numerical Analysis and its Applications To Continuum Physics, Soc. Brasileira de Matematica, Rio de Janeiro, 1980, pp. 65-73.
- [70] M. Cheney, D. Isaacson, J.C. Newell, *Electrical impedance tomography*, SIAM Review **41**, 1999, n.1, pp. 85-101.
- [71] J. C. Goble, D. G. Gisser, D. Isaacson, and J. Newell, *Electrical impedance tomography in three dimensions*, Proceedings of the Biomedical engineering Society conference (1990).
- [72] M. Cheney, D. Isaacson, J.C. Newell, S. Simske, and J. Goble, *NOSER: An algorithm for solving the inverse conductivity problem*, International Journal of Imaging Systems and Technology **2**, 1990, pp. 87-102.
- [73] D. G. Gisser, D. Isaacson, and J.C. Newell Current topics in impedance imaging, Clinical Physics and Physiological Measurement **8**, 1987, pp. 39-46.
- [74] O.Dorn, H. Bertete-Aguirre, J. C. Berryman, and G. C. Papanicolau, *Sensitivity analysis of a nonlinear inversion method for 3D electromagnetic imaging in anisotropic media*, Inverse Problems **18**, 2002, n.2, pp. 285-317.
- [75] J.G. Webster, *Electrical impedance tomography*, Adam Hilger, Bristol, 1990.
- [76] A.Wexler, *Electrical impedance imaging in two and three dimensions*, Clinical Physics and Physiological Measurement **9**, 1988, pp. 29-33.
- [77] N.Polydorides, W.R.B.Lionheart, and H. Maccann, *Krylov subspace iterative techniques: On the detection of brain activity with electrical impedance tomography*, IEEE Transactions on Medical Imaging **21**, 2002. n.6, pp. 596-603.
- [78] M. Vauhkonen, D. Vadasz, P.A. Karjalainen, E. Somarsalo, and J.P. Kaipio, *Tikhonov regularization and prior information in electrical impedance tomography*, IEEE Transactions on Medical Imaging **17**, 1998, n. 2, pp. 285-293.
- [79] A.Borsic, W.R.B. Lionheart, and C.N. McLeod, *Generation of anisotropic smoothness regularization filters for EIT*, IEEE Transactions on Medical Imaging **21**, 2002. n.6, pp. 579-587.
- [80] S.R. Arridge, *Topical review: Optical tomography in medical imaging*, Inverse problems **15**, 1999, R41-R49.

- [81] J.P. Kaipio, V. Kolehmainen, E. Somersalo, and M. Vauhkonen, *Statistical inversion in Monte Carlo sampling methods in electrical impedance tomography*, Inverse Problems **16**, 2000, pp. 1487-1522.
- [82] R.A. Williams and M.S Beck, *Process tomography: principles, techniques and applications*, Butterworth- Heinemann, Oxford, 1995.
- [83] M. Vauhkonen, *Electrical impedance tomography and prior information*, PhD. Thesis, Kuopio University, Kuopio, 1997.
- [84] V. Kolehmainen, M. Vauhkonen, P.A. Karjalainen, and J. P. Kaipio, *Assessment of errors in statical electrical impedance tomography with adjacent and trigonometric current patterns*, Physiological Measurement **18**, 1997, pp. 289-303.
- [85] A. N. Tikhonov and V.Y. Arsenin, *Solutions of ill-posed problems*, Winston, Washington DC, 1997.
- [86] M. Cheney, D. Isaacson, J. Newell, J. Goble, and S. Simske, *NOSER: An algorithm for solving the inverse conductivity problem*, Internat. J. Imaging Systems and Technology **2** (1990), pp. 66–75.
- [87] L.F. Fuks, M. Cheney, D. Isaacson, D.G. Gisser, and J.C. Newell, *Detection and imaging of electric conductivity and permittivity at low frequency*, IEEE Trans. Biomed. Engr. **3** (1991), pp. 1106–1110.
- [88] S. Simske, *An Adaptive Current Determination and a One-Step Reconstruction Technique for a Current Tomography System*, Master's Thesis, Rensselaer Polytechnic Institute, Troy, NY, 1987.
- [89] M.Hanke, *Coniugate gradient type methods for ill-posed problems*, Scientific & Technical, Longman, Essex, 1995.
- [90] W. Lionearth, *EIT reconstruction algorithms: Pitfalls, challenges and recent development*, Physiol. Meas., vol. 25, pp.125-142, 2004.
- [91] D.G. Gisser, D. Isaacson, and J. C. Newell, *Electric current computed tomography and enginvalues*, SIAM J.Appl. Math., vol.50, n.6, pp.1623-1634, Dec.1990.
- [92] D. G. Gisser, D. Isaacson, and J.C.Neewell, *Current topics in impedance imaging*, Clinical Physics and Physiological Measurements, Vol.8,pp. 39-46, 1987.
- [93] E. Somersalo, M.Cheney, and D.Isaacson, *Existence and uniqueness for electrode models for electric current computed tomography*, SIAM J. Appl. Math., vol.52, pp. 1023-1040, 1992.

- [94] M. Vauhkonen, W. R.B. Lionheart, L.M. Heikkinen, *A MATLAB toolkit for the EIDORS project to reconstruct two-dimensional EIT images*, 2001 *Physiol. Meas.* **22**, 107.
- [95] P.P. Sylvester and R.L. Ferrari, *Finite elements for electrical engineers*, Cambridge University Press, Cambridge, 2001.
- [96] P.C. Hansen, *Rank deficient and discrete ill-posed problems. Numerical aspect of linear inversion*, SIAM, Philadelphia, 1997.
- [97] G.H.Golub and C.F. Van Loan, *Matrix computations*, third ed., Johns Hopkins, n.1.,185-194.
- [98] s.g. nASH, R. Polyak, and A. Sofer, *A numerical comparison barrier and modified-barrier methods for large-scale bound-constrained optimization*, Large Scale Optimization: State of the Art 1, 1994, pp. 319-338.
- [99] N.L. Trefethen and D.Bau III, *Numerical linear algebra*, SIAM, Philadelphia, 1994.
- [100] C.R. Vogel, *Computational methods for inverse problems*, SIAM, Philadelphia, 2002.
- [101] W.R. Breckon, *Image reconstruction in Electrical Impedance Tomography*, PhD. Thesis, Oxford Polytechnic, Oxford, 1990.
- [102] B.Graham, Andy Adler, *Objective Selection of Hyperparameter for EIT*, School of Information Technology and Engineering (SITE), University of Ottawa,Canada, 2005.
- [103] M. Cheney, D. Isaacson, and J. C. Goble, *Electrical Impedance Tomography in three dimensions*, Applied Computational Electromagnetics Soc. Journal, 7, 128-147 (1992).
- [104] Camille Gómez-Laberge, Andy Adler, *Imaging of electrode movement and conductivity change in electrical impedance tomography*, 2005.
- [105] Data Sheet, F58511B105G200 Spring Contact Probe, Farnell, U.K.
- [106] Manual, *About Lock-in Amplifiers*, Stanford Research systems.
- [107] Data Sheet, HCF4067B Analog Single 16 channel multiplexer, STMicroelectronics.
- [108] M. Cheney and D. Isaacson, *NOSER: An algorithm for solving the Inverse Conductivity Problem*, International Journal of Imaging Systems and Technology, vol. 2, pp.66-75, 1990.
- [109] Data Sheet, Vinculum - V2DIP1-64, FDTI.
- [110] Data Sheet, BNC connector 5-1634556-0, Tyco.
- [111] Data Sheet, connector 3416-0000S/EC DIL Plug, Farnell, U.K.

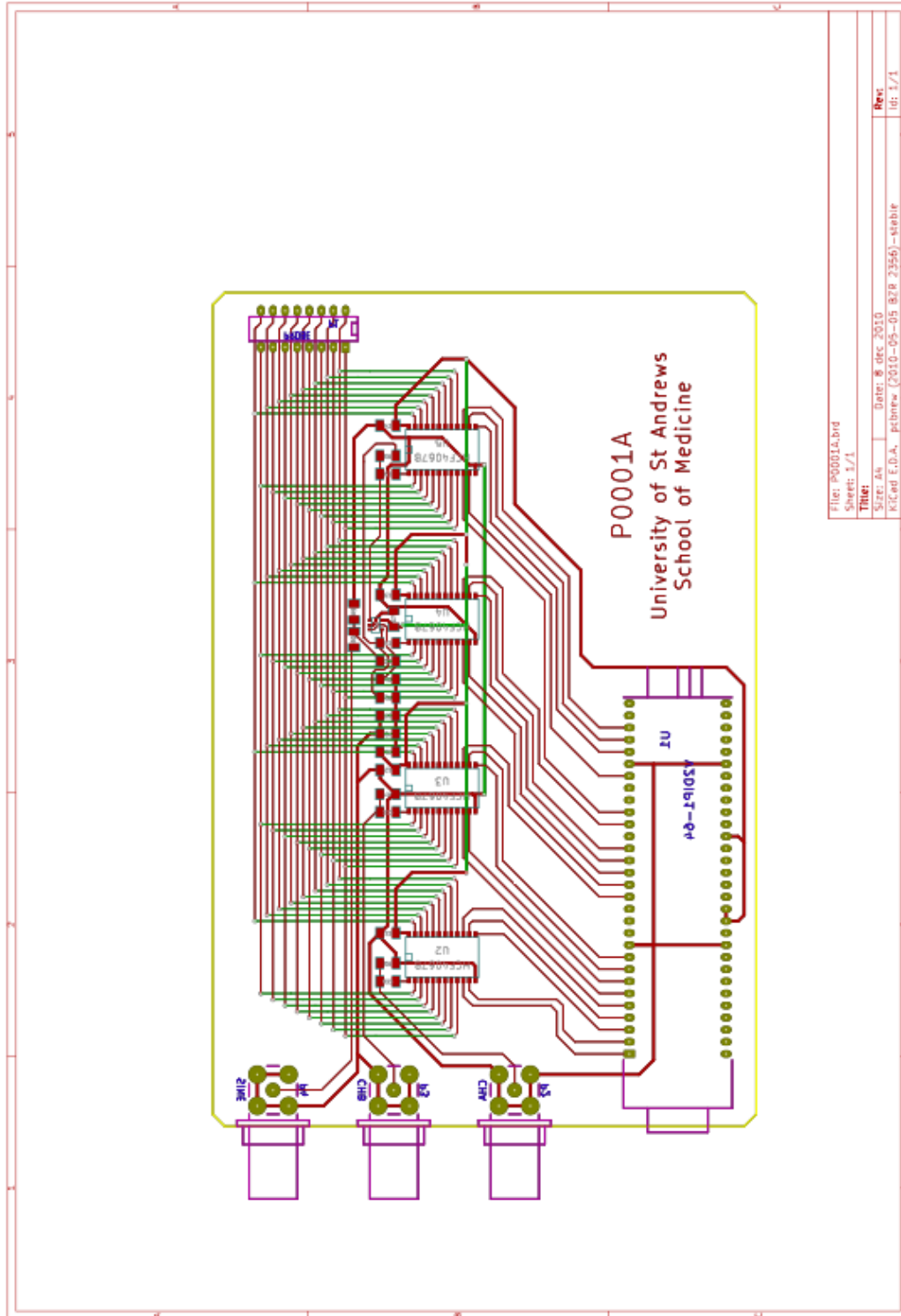
- [112] Data Sheet, SR810 Lock-In Amplifier, Stanford Research Systems, California.
- [113] Data Sheet, hard brass alloy wire, Heckscher LTD., London, U.K.
- [114] Andy Adler and William R B Lionheart, *Uses and abuses of EIDORS: an extensible software base for EIT*, *Physiol. Meas.* 27 (2006) S25–S42.
- [115] K. J. Bathe, *Finite Element Procedures*. Englewood Cliffs, NJ: Prentice-Hall, 1996.
- [116] M. Hanke and M. Bruhl, *Recent progress in electrical impedance tomography*, *Inverse Problems*, vol. 19, pp. S65–S90, 2003.
- [117] T. Tuykin and A. Korjanevsky, *3D EIT imaging with planar electrode array: numerical simulation*, *Physiol. Meas.* **26** S101
- [118] Cherepenin V., Karpov A., Kornienko V., Kultiasov Y., Ovchepkin M., Trochanova O. and Meister D., *Three-dimensional EIT imaging of breast tissue: system design and clinical testing*, *IEEE Trans. Medical Imaging*, 21 662, 2002.
- [119] K. R. Foster and H. P. Schwan, *Dielectric properties of tissues and biological materials: a critical review*. *Crit. Rev. Biomed. Eng.* 1989; 17:25–104.
- [120] A. J. Surowiec, S. S. Stuchly, J. R. Barr, and A. Swarup, *Dielectric properties of breast carcinoma and the surrounding tissues*, *IEEE Trans. Biomed. Eng.*, vol. 35, no. 4, pp. 257–263, Apr. 1988.
- [121] J. E. Silva, J. P. Marques, and J. Jossinet, *Classification of breast tissue by electrical impedance spectroscopy*, *Med. Biol. Eng. Comput.*, vol. 38, pp. 26–30, 2000.
- [122] Korjanevsky A.V. and Tuykin T.S., *Phase measurement for electric field tomography*, *Physiol. Meas.*, 29 S151, 2008.
- [123] Y. Yamamoto, T. Yamamoto, and T. Ozawa, *Characteristics of skin admittance for dry electrodes and the measurement of skin moisturisation*. *Med. Biol. Eng. Comput.* 1986; 24:71–77.
- [124] O. G. Martinsen, S. Grimnes, and E. Haug, *Measuring depth depends on frequency in electrical skin impedance measurements*. *Skin Res. Technol.* 1999; 5:179–181.
- [125] L. M. Heikkinen, T. Vilhunen, R. M. West, and M. Vauhkonen, *Simultaneous reconstruction of electrode contact impedances and internal electrical properties: 2. Laboratory experiments*, *Meas. Sci. Tech.*, vol. 13, pp. 1855–1861, 2002.

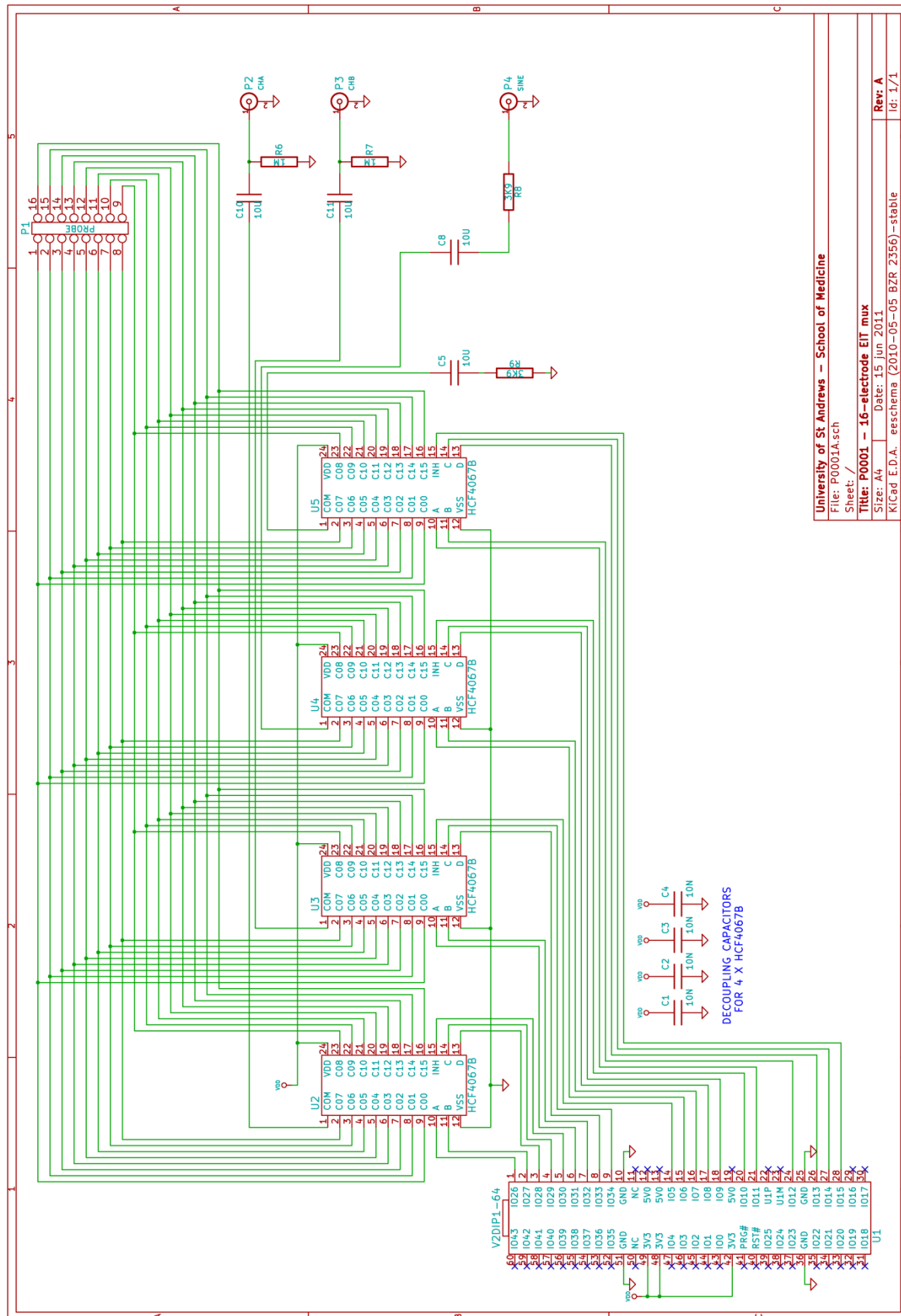
- [126] V. Kolehmainen, M. Vauhkonen, P. A. Karjalainen, and J. P. Kaipio, *Assessment of errors in static electrical impedance tomography with adjacent and trigonometric current patterns*, *Physiological Meas.*, vol. 18, pp. 289–303, 1997.
- [127] Nick Polydorides¹ and William R. B. Lionheart, *A Matlab toolkit for three-dimensional electrical impedance tomography: a contribution to the Electrical Impedance and Diffuse Optical Reconstruction Software project*, Institute of Physics Publishing, *Meas. Sci. Technol.* 13 (2002) 1871–1883.
- [128] Netgen Users Manual available on <http://www.cfd-online.com/Forums/openfoam-meshing-netgen/73965-netgen-user-manual.html>.

APPENDIX:

A. Printed Components

A.1. EIT System Components





University of St Andrews – School of Medicine
 File: P0001A.sch
 Sheet: /
Title: P0001 – 16-electrode EIT mux
 Size: A4 Date: 15 Jun 2011
 KiCad E.D.A. eschema (2010-05-05 BZR 2356) –stable
 Rev: A
 Id: 1/1

```

/*
** IOMux.c
**
** C Source file for Vinculum II IOMux Configuration
**
** Author: FTDI IOMux Configuration Application
** Project:
** Module:
** Requires: VOS
** Comments: Automatically Generated File
**
** History:
** 1 Initial version
**
*/
#include "vos.h"
void SetupIOMUX()
{
    unsigned char packageType;

    packageType = vos_get_package_type();

    //*****
    //Initialise the IOMUX parameters
    //*****

    if(packageType == VINCULUM_II_64_PIN)
    {
        // GPIO Port E 1 to pin 16 as Output.
        vos_iomux_define_output(16, IOMUX_OUT_GPIO_PORT_E_1);
        // GPIO Port C 2 to pin 17 as Output.
        vos_iomux_define_output(17, IOMUX_OUT_GPIO_PORT_C_2);
        // GPIO Port C 3 to pin 18 as Output.
        vos_iomux_define_output(18, IOMUX_OUT_GPIO_PORT_C_3);
        // GPIO Port C 4 to pin 19 as Output.
        vos_iomux_define_output(19, IOMUX_OUT_GPIO_PORT_C_4);
        // GPIO Port C 5 to pin 20 as Output.
        vos_iomux_define_output(20, IOMUX_OUT_GPIO_PORT_C_5);
        // GPIO Port E 2 to pin 22 as Output.
        vos_iomux_define_output(22, IOMUX_OUT_GPIO_PORT_E_2);
        // GPIO Port D 3 to pin 23 as Output.
        vos_iomux_define_output(23, IOMUX_OUT_GPIO_PORT_D_3);
        // GPIO Port D 4 to pin 24 as Output.
        vos_iomux_define_output(24, IOMUX_OUT_GPIO_PORT_D_4);
        // GPIO Port D 5 to pin 25 as Output.
        vos_iomux_define_output(25, IOMUX_OUT_GPIO_PORT_D_5);
    }
}

```



```

// GPIO Port D 6 to pin 26 as Output.
vos_iomux_define_output(26, IOMUX_OUT_GPIO_PORT_D_6);
// GPIO Port E 3 to pin 27 as Output.
vos_iomux_define_output(27, IOMUX_OUT_GPIO_PORT_E_3);
// GPIO Port A 2 to pin 45 as Output.
vos_iomux_define_output(45, IOMUX_OUT_GPIO_PORT_A_2);
// GPIO Port A 3 to pin 46 as Output.
vos_iomux_define_output(46, IOMUX_OUT_GPIO_PORT_A_3);
// GPIO Port A 4 to pin 47 as Output.
vos_iomux_define_output(47, IOMUX_OUT_GPIO_PORT_A_4);
// GPIO Port A 5 to pin 48 as Output.
vos_iomux_define_output(48, IOMUX_OUT_GPIO_PORT_A_5);
// GPIO Port E 6 to pin 49 as Output.
vos_iomux_define_output(49, IOMUX_OUT_GPIO_PORT_E_6);
// GPIO Port B 3 to pin 50 as Output.
vos_iomux_define_output(50, IOMUX_OUT_GPIO_PORT_B_3);
// GPIO Port B 4 to pin 51 as Output.
vos_iomux_define_output(51, IOMUX_OUT_GPIO_PORT_B_4);
// GPIO Port B 5 to pin 52 as Output.
vos_iomux_define_output(52, IOMUX_OUT_GPIO_PORT_B_5);
// GPIO Port B 6 to pin 55 as Output.
vos_iomux_define_output(55, IOMUX_OUT_GPIO_PORT_B_6);
    }
}

```

```

#include "vos.h"
#include "GPIO.h"
#include "USBSlave.h"
#include "ioctl.h"
#include "USBSlaveFT232.h"
#include "USBSlaveFT232App.h"

vos_tcb_t *tcbLoopback;

VOS_HANDLE hB;
VOS_HANDLE hFT232;

gpio_ioctl_cb_t gpio_iocbA, gpio_iocbB, gpio_iocbC, gpio_iocbD, gpio_iocbE;
gpio_context_t gpioCtxA, gpioCtxB, gpioCtxC, gpioCtxD, gpioCtxE;
VOS_HANDLE ioA, ioB, ioC, ioD, ioE;

void loopback(VOS_HANDLE h);
void SetupIOMUX();

void init_devices(void)
{
    unsigned char portData;
    unsigned short num_written;

    usbslave_init(USBSLAVE_PORT_B, USBSB);
    usbslaveft232_init(USBSFT232);
    SetupIOMUX();

    gpioCtxE.port_identifier = GPIO_PORT_E;
    gpio_init(VOS_DEV_GPIO_E, &gpioCtxE);
    ioE = vos_dev_open(VOS_DEV_GPIO_E);
    gpio_iocbE.ioctl_code = VOS_IOCTL_GPIO_SET_MASK;
    gpio_iocbE.value = 0xFF;
    vos_dev_ioctl(ioE, &gpio_iocbE);

    portData = 0; //inhibit all mux channels
    vos_dev_write(ioE, &portData, 1, &num_written);

    gpioCtxA.port_identifier = GPIO_PORT_A;
    gpio_init(VOS_DEV_GPIO_A, &gpioCtxA);
    ioA = vos_dev_open(VOS_DEV_GPIO_A);
    gpio_iocbA.ioctl_code = VOS_IOCTL_GPIO_SET_MASK;
    gpio_iocbA.value = 0xFF;
    vos_dev_ioctl(ioA, &gpio_iocbA);

```

```

gpioCtxB.port_identifier = GPIO_PORT_B;
gpio_init(VOS_DEV_GPIO_B, &gpioCtxB);
ioB = vos_dev_open(VOS_DEV_GPIO_B);
gpio_iocbB.ioctl_code = VOS_IOCTL_GPIO_SET_MASK;
gpio_iocbB.value = 0xFF;
vos_dev_ioctl(ioB, &gpio_iocbB);

gpioCtxC.port_identifier = GPIO_PORT_C;
gpio_init(VOS_DEV_GPIO_C, &gpioCtxC);
ioC = vos_dev_open(VOS_DEV_GPIO_C);
gpio_iocbC.ioctl_code = VOS_IOCTL_GPIO_SET_MASK;
gpio_iocbC.value = 0xFF;
vos_dev_ioctl(ioC, &gpio_iocbC);

gpioCtxD.port_identifier = GPIO_PORT_D;
gpio_init(VOS_DEV_GPIO_D, &gpioCtxD);
ioD = vos_dev_open(VOS_DEV_GPIO_D);
gpio_iocbD.ioctl_code = VOS_IOCTL_GPIO_SET_MASK;
gpio_iocbD.value = 0xFF;
vos_dev_ioctl(ioD, &gpio_iocbD);
}

void main(void)
{
    common_ioctl_cb_t ft232Attach;

    vos_init(VOS_QUANTUM, VOS_TICK_INTERVAL, NUMBER_OF_DEVICES);

    vos_set_clock_frequency(VOS_48MHZ_CLOCK_FREQUENCY);

    init_devices();

    // open USB Slave port
    hB = vos_dev_open(USBSB);

    // open FT232BM
    hFT232 = vos_dev_open(USBSFT232);

    // attach FT232BM to USB Slave port A
    ft232Attach.ioctl_code = VOS_IOCTL_USBSLAVEFT232_ATTACH;
    ft232Attach.set.data = hB;
    vos_dev_ioctl(hFT232, &ft232Attach);

    tcbLoopback = vos_create_thread(31, TCB_SIZE, loopback, 2, hFT232);

```

```

    vos_start_scheduler();

main_loop:

    goto main_loop;
}

unsigned char readbuf[128];

void loopback(VOS_HANDLE h)
{
    common_ioctl_cb_t iocb;
    unsigned short qs;
    unsigned short bytesTransferred;
    char c1, c2, c3, c4; //shift register
    unsigned char DataA, DataB, DataC, DataD, DataE;
    unsigned short num_written;

    c1='X';
    c2='X';
    c3='X';
    c4='X';

    iocb.ioctl_code = VOS_IOCTL_COMMON_GET_RX_QUEUE_STATUS;
    iocb.get.queue_stat = 0;

    while (1)
    {
        vos_dev_ioctl(h,&iocb);
        qs = iocb.get.queue_stat;
        if (qs == 0)
        {
            vos_delay_msecs(10);
            continue;
        }

        //echo
        //vos_dev_read(h,readbuf,qs,&bytesTransferred);
        //vos_dev_write(h,readbuf,qs,&bytesTransferred);

        vos_dev_read(h,readbuf,1,&bytesTransferred);

        //check for terminator

```

```

if (readbuf[0] != '#')
{

    //insert in shift register

    c4 = c3;
    c3 = c2;
    c2 = c1;
    c1 = readbuf[0];
}
else
{

    //terminator found: parse
    DataA = 0;
    DataB = 0;
    DataC = 0;
    DataD = 0;
    DataE = 0b11111111;
    switch (c4)
    {
        case '0':
            DataA = 0b00000000;
            DataE = DataE & 0b10111111;
            break;
        case '1':
            DataA = 0b00000100;
            DataE = DataE & 0b10111111;
            break;
        case '2':
            DataA = 0b00001000;
            DataE = DataE & 0b10111111;
            break;
        case '3':
            DataA = 0b00001100;
            DataE = DataE & 0b10111111;
            break;
        case '4':
            DataA = 0b00100000;
            DataE = DataE & 0b10111111;
            break;
        case '5':
            DataA = 0b00100100;
            DataE = DataE & 0b10111111;
            break;
        case '6':

```

```

        DataA = 0b00101000;
        DataE = DataE & 0b10111111;
        break;
    case '7':
        DataA = 0b00101100;
        DataE = DataE & 0b10111111;
        break;
    case '8':
        DataA = 0b00010000;
        DataE = DataE & 0b10111111;
        break;
    case '9':
        DataA = 0b00010100;
        DataE = DataE & 0b10111111;
        break;
    case 'A':
        DataA = 0b00011000;
        DataE = DataE & 0b10111111;
        break;
    case 'B':
        DataA = 0b00011100;
        DataE = DataE & 0b10111111;
        break;
    case 'C':
        DataA = 0b00110000;
        DataE = DataE & 0b10111111;
        break;
    case 'D':
        DataA = 0b00110100;
        DataE = DataE & 0b10111111;
        break;
    case 'E':
        DataA = 0b00111000;
        DataE = DataE & 0b10111111;
        break;
    case 'F':
        DataA = 0b00111100;
        DataE = DataE & 0b10111111;
        break;
    default:
        break;
} // end switch (c4)

switch (c3)
{
    case '0':

```

```

    DataB = 0b00000000;
    DataE = DataE & 0b11111101;
    break;
case '1':
    DataB = 0b00001000;
    DataE = DataE & 0b11111101;
    break;
case '2':
    DataB = 0b00010000;
    DataE = DataE & 0b11111101;
    break;
case '3':
    DataB = 0b00011000;
    DataE = DataE & 0b11111101;
    break;
case '4':
    DataB = 0b01000000;
    DataE = DataE & 0b11111101;
    break;
case '5':
    DataB = 0b01001000;
    DataE = DataE & 0b11111101;
    break;
case '6':
    DataB = 0b01010000;
    DataE = DataE & 0b11111101;
    break;
case '7':
    DataB = 0b01011000;
    DataE = DataE & 0b11111101;
    break;
case '8':
    DataB = 0b00100000;
    DataE = DataE & 0b11111101;
    break;
case '9':
    DataB = 0b00101000;
    DataE = DataE & 0b11111101;
    break;
case 'A':
    DataB = 0b00110000;
    DataE = DataE & 0b11111101;
    break;
case 'B':
    DataB = 0b00111000;
    DataE = DataE & 0b11111101;

```

```

        break;
    case 'C':
        DataB = 0b01100000;
        DataE = DataE & 0b11111101;
        break;
    case 'D':
        DataB = 0b01101000;
        DataE = DataE & 0b11111101;
        break;
    case 'E':
        DataB = 0b01110000;
        DataE = DataE & 0b11111101;
        break;
    case 'F':
        DataB = 0b01111000;
        DataE = DataE & 0b11111101;
        break;
    default:
        break;
} // end switch (c3)

switch (c2)
{
    case '0':
        DataC = 0b00000000;
        DataE = DataE & 0b11111011;
        break;
    case '1':
        DataC = 0b00000100;
        DataE = DataE & 0b11111011;
        break;
    case '2':
        DataC = 0b00001000;
        DataE = DataE & 0b11111011;
        break;
    case '3':
        DataC = 0b00001100;
        DataE = DataE & 0b11111011;
        break;
    case '4':
        DataC = 0b00100000;
        DataE = DataE & 0b11111011;
        break;
    case '5':
        DataC = 0b00100100;
        DataE = DataE & 0b11111011;

```



```

        break;
    case '6':
        DataC = 0b00101000;
        DataE = DataE & 0b11111011;
        break;
    case '7':
        DataC = 0b00101100;
        DataE = DataE & 0b11111011;
        break;
    case '8':
        DataC = 0b00010000;
        DataE = DataE & 0b11111011;
        break;
    case '9':
        DataC = 0b00010100;
        DataE = DataE & 0b11111011;
        break;
    case 'A':
        DataC = 0b00011000;
        DataE = DataE & 0b11111011;
        break;
    case 'B':
        DataC = 0b00011100;
        DataE = DataE & 0b11111011;
        break;
    case 'C':
        DataC = 0b00110000;
        DataE = DataE & 0b11111011;
        break;
    case 'D':
        DataC = 0b00110100;
        DataE = DataE & 0b11111011;
        break;
    case 'E':
        DataC = 0b00111000;
        DataE = DataE & 0b11111011;
        break;
    case 'F':
        DataC = 0b00111100;
        DataE = DataE & 0b11111011;
        break;
    default:
        break;
} // end switch (c2)

switch (c1)

```

```

{
case '0':
    DataD = 0b000000000;
    DataE = DataE & 0b11110111;
    break;
case '1':
    DataD = 0b00001000;
    DataE = DataE & 0b11110111;
    break;
case '2':
    DataD = 0b00010000;
    DataE = DataE & 0b11110111;
    break;
case '3':
    DataD = 0b00011000;
    DataE = DataE & 0b11110111;
    break;
case '4':
    DataD = 0b01000000;
    DataE = DataE & 0b11110111;
    break;
case '5':
    DataD = 0b01001000;
    DataE = DataE & 0b11110111;
    break;
case '6':
    DataD = 0b01010000;
    DataE = DataE & 0b11110111;
    break;
case '7':
    DataD = 0b01011000;
    DataE = DataE & 0b11110111;
    break;
case '8':
    DataD = 0b00100000;
    DataE = DataE & 0b11110111;
    break;
case '9':
    DataD = 0b00101000;
    DataE = DataE & 0b11110111;
    break;
case 'A':
    DataD = 0b00110000;
    DataE = DataE & 0b11110111;
    break;
case 'B':

```

```

        DataD = 0b00111000;
        DataE = DataE & 0b11110111;
        break;
    case 'C':
        DataD = 0b01100000;
        DataE = DataE & 0b11110111;
        break;
    case 'D':
        DataD = 0b01101000;
        DataE = DataE & 0b11110111;
        break;
    case 'E':
        DataD = 0b01110000;
        DataE = DataE & 0b11110111;
        break;
    case 'F':
        DataD = 0b01111000;
        DataE = DataE & 0b11110111;
        break;
    default:
        break;
} // end switch (c1)

vos_dev_write(ioA,&DataA,1,&num_written);
vos_dev_write(ioB,&DataB,1,&num_written);
vos_dev_write(ioC,&DataC,1,&num_written);
vos_dev_write(ioD,&DataD,1,&num_written);
vos_dev_write(ioE,&DataE,1,&num_written);

} //end if

} //end while

return;
} //end loopback

```

```
#ifndef __USBSlaveFT232_h__
#define __USBSlaveFT232_h__

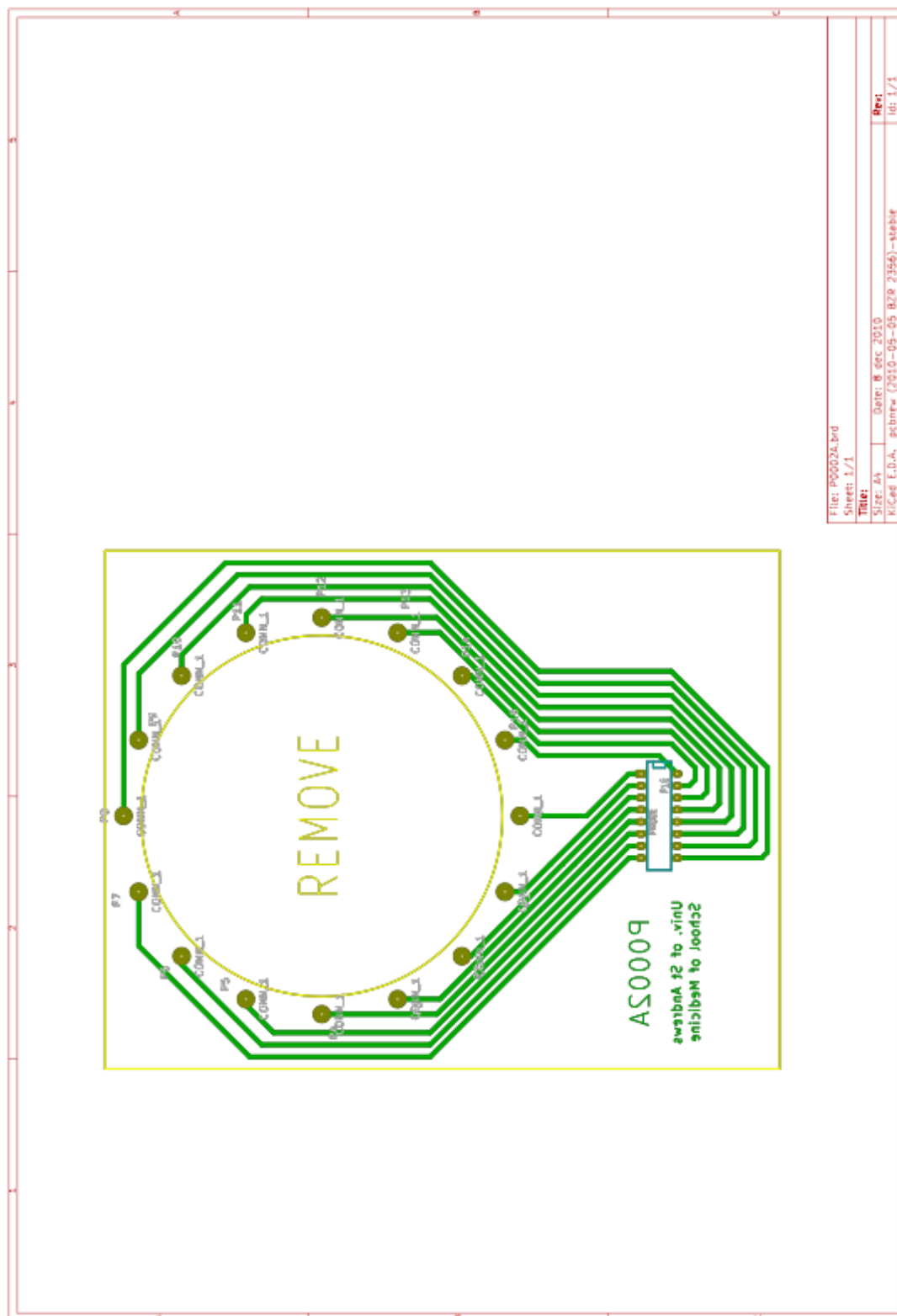
#define TCB_SIZE          512

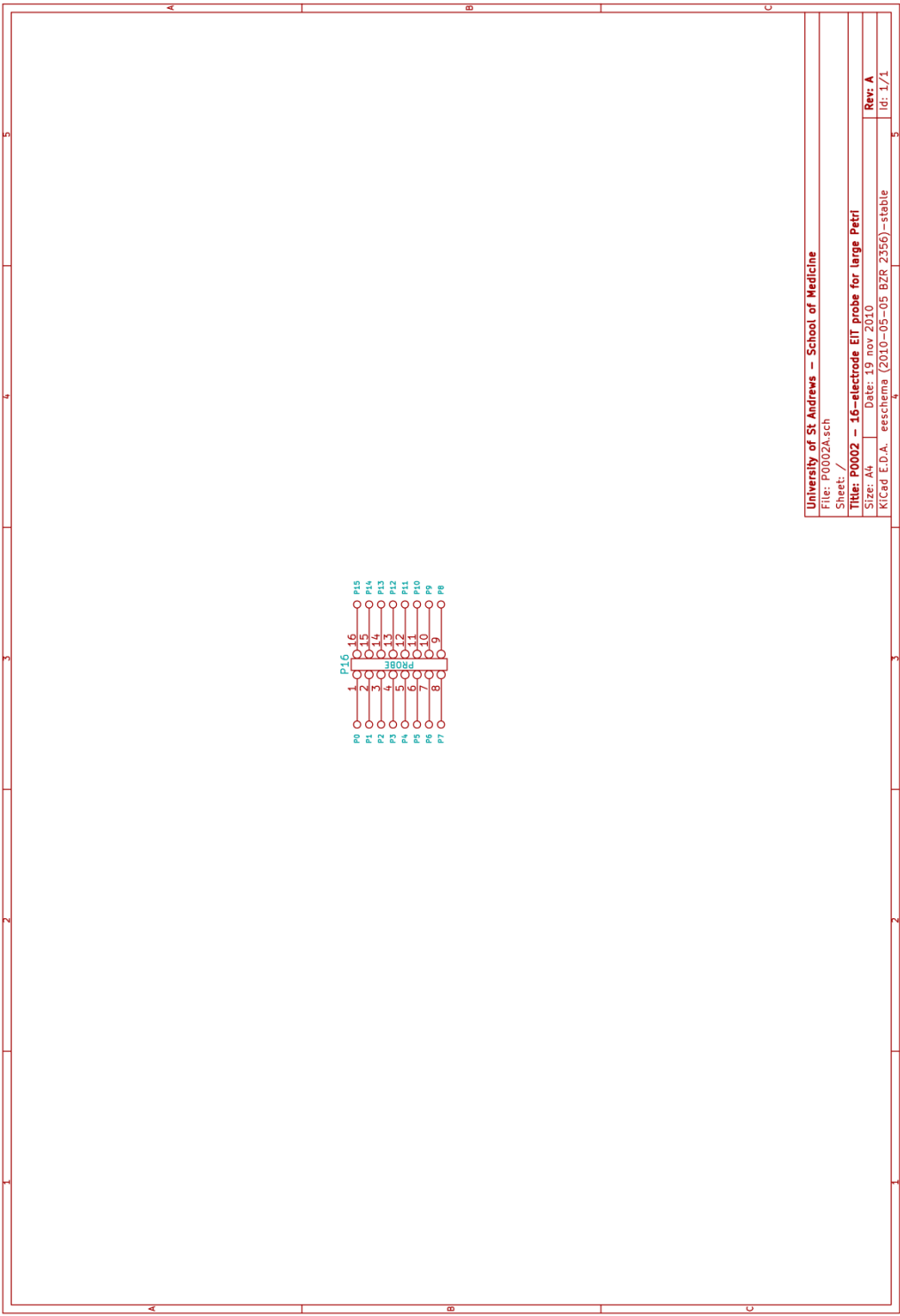
#define NUMBER_OF_DEVICES    7

#define USBSB              0
#define USBSFT232          1
#define VOS_DEV_GPIO_A     2
#define VOS_DEV_GPIO_B     3
#define VOS_DEV_GPIO_C     4
#define VOS_DEV_GPIO_D     5
#define VOS_DEV_GPIO_E     6

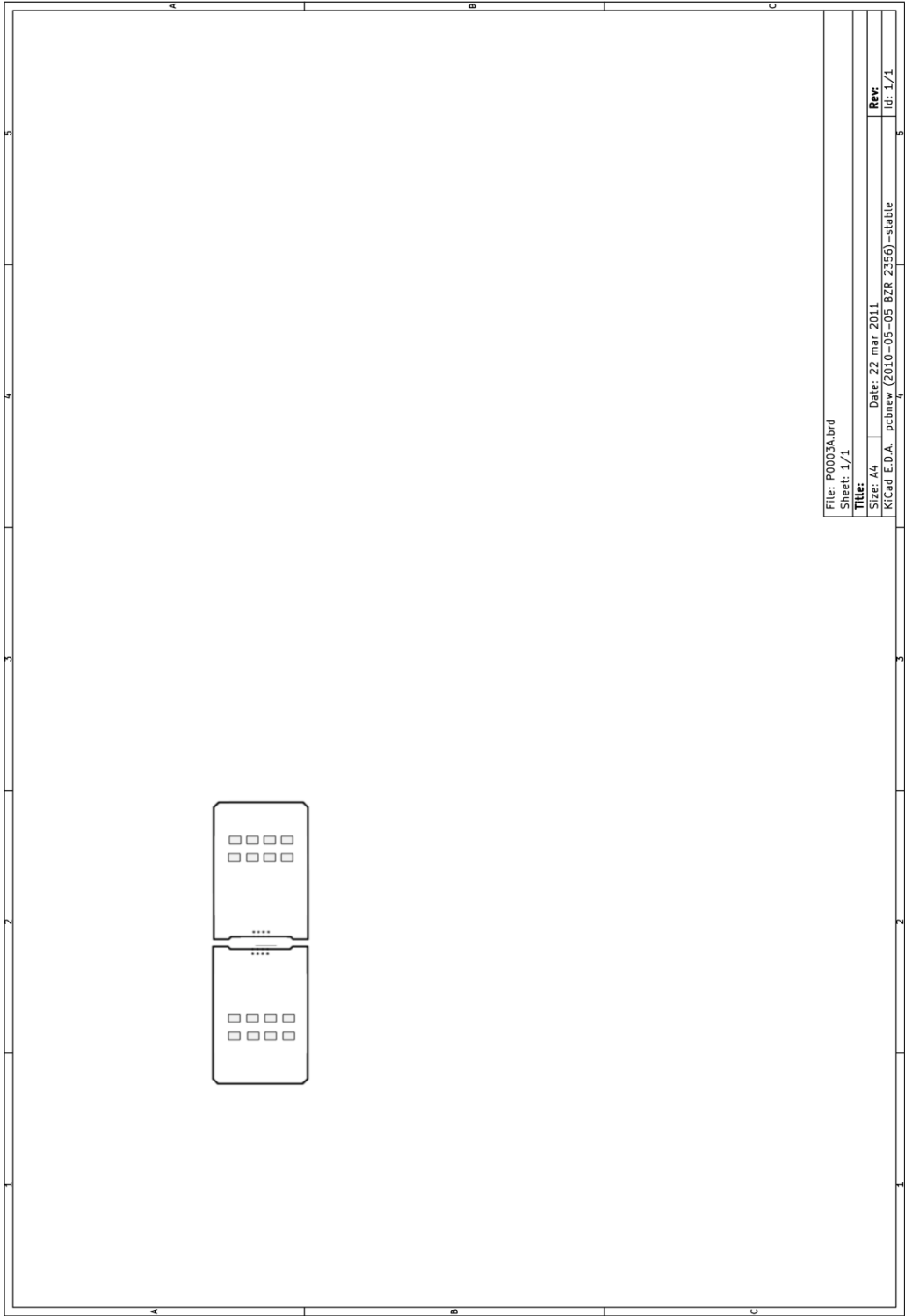
#endif
```

A.2. Circular Electrode Array





A.3. Planar Electrode Array



B. Data Acquisition Matlab Codes

B.1. Impedance Measurement Code

```
%The code at each change of frequency produces messages
%to get ready the user to move the electrode manually in order to obtain
%the measurement of Vin, VR and Vz.
%I used two opposite electrodes for stimulation and measurement.

%//initialize the connection with the Lock-in for more details check the
%Lock-in amplifier's Manual
s = serial('COM3');
s.Terminator= 'CR' ;%The Lock-in recognizes a command if CR is its terminator
s.FlowControl='hardware';
fopen(s); %start the connection with Lock-in amplifier
s.RequestToSend='on';
fprintf(s,'REST');

%%%Measurement CYCLE
start_acquisition_index=1;
t=1;%index for frequency
while start_acquisition_index>0
    if t==1
        display('1)prepare the electrodes for measuring Ving')
        pause ( 4 );
        display('freq 100KHZ')
        fprintf (s,'FREQ10E4')%set the frequency
        pause ( 1 );
    end
    if t==2
        display('2)prepare the electrodes for measuring Ving')
        pause ( 5 );
        display('freq 82KHZ')
        fprintf (s,'FREQ82E3')%set the frequency
        pause ( 1 );
    end
    if t==3
        display('3)prepare the electrodes for measuring Ving')
        pause ( 5 );
        display('freq 68KHZ')
        fprintf (s,'FREQ68E3')%set the frequency
        pause ( 1 );
    end
    if t==4
        display('4)prepare the electrodes for measuring Ving')
        pause ( 5 );
        display('freq 56KHZ')
        fprintf (s,'FREQ56E3')%set the frequency
        pause ( 1 );
    end
    if t==5
```



```

        display('5)prepare the electrodes for measuring Ving')
        pause ( 5 );
        display('freq 47KHZ')
        fprintf (s,'FREQ47E3')%set the frequency
        pause ( 1 );
    end
    if t==6
        display('6)prepare the electrodes for measuring Ving')
        pause ( 5 );
        display('freq 39KHZ')
        fprintf (s,'FREQ39E3')%set the frequency
        pause ( 1 );
    end
    if t==7
        display('4)prepare the electrodes for measuring Ving')
        pause ( 5 );
        display('freq 33KHZ')
        fprintf (s,'FREQ33E3')%set the frequency
        pause ( 1 );
    end
    if t==8
        display('4)prepare the electrodes for measuring Ving')
        pause ( 5 );
        display('freq 27KHZ')
        fprintf (s,'FREQ27E3')%set the frequency
        pause ( 1 );
    end
    if t==9
        display('9)prepare the electrodes for measuring Ving')
        pause ( 5 );
        display('freq 22KHZ')
        fprintf (s,'FREQ22E3')%set the frequency
        pause ( 1 );
    end
    if t==10
        display('10)prepare the electrodes for measuring Ving')
        pause ( 5 );
        display('freq 18KHZ')
        fprintf (s,'FREQ18E3')%set the frequency
        pause ( 1 );
    end
    if t==11
        display('11)prepare the electrodes for measuring Ving')
        pause ( 5 );
        display('freq 15KHZ')
        fprintf (s,'FREQ15E3')%set the frequency
        pause ( 1 );
    end
    if t==12
        display('12)prepare the electrodes for measuring Ving')
        pause ( 5 );
        display('freq 12KHZ')
        fprintf (s,'FREQ12E3')%set the frequency
        pause ( 1 );
    end
    if t==13
        display('13)prepare the electrodes for measuring Ving')

```

```

        pause ( 5 );
        display('freq 10KHZ')
        fprintf (s,'FREQ10E3')%set the frequency
        pause ( 1 );
    end
    if t==14
        display('14)prepare the electrodes for measuring Ving')
        pause ( 5 );
        display('freq 1KHZ')
        fprintf (s,'FREQ1E3')%set the frequency
        pause ( 1 );
    end
    if t==15
        display('15)prepare the electrodes for measuring Ving')
        pause ( 5 );
        display('freq 100HZ')
        fprintf (s,'FREQ100E1')%set the frequency
        pause ( 1 );
    end
    if t==16
        display('16)prepare the electrodes for measuring Ving')
        pause ( 5 );
        display('freq 10HZ')
        fprintf (s,'FREQ10E1')%set the frequency
        pause ( 1 );
    end
    end

%//-->> ACQUISITIONS from the Lock-in:
% Measure Ving
fprintf(s,'APHS');% i make sure the signal is in phase with the reference
pause( 1 );%wait
fprintf(s,'APHS');
pause (0.5 ); %wait for a stable measurement 5Tau (=100ms*5=0.5 sec)
fprintf(s,'OUTP?1');Ving_Vi_Vz_X_Y_PHASE_R(n,1)=fscanf (s,'%f');
                                %acquire the in phase component
fprintf(s,'OUTP?2');Ving_Vi_Vz_X_Y_PHASE_R(n,2)=fscanf (s,'%f');
                                %acquire the quadrature component
fprintf (s,'OUTP?4');Ving_Vi_Vz_X_Y_PHASE_R(n,3)=fscanf (s,'%f');
                                %acquire the phase angle
fprintf (s,'OUTP?3');Ving_Vi_Vz_X_Y_PHASE_R(n,4)=fscanf (s,'%f')
                                %acquire the module
display('END')
    pause ( 2 );

% NOW Measure Vi
display('prepare electrodes for measuring Vi ') % at the same frequency
pause ( 15 );
fprintf (s,'OUTP?1');Ving_Vi_Vz_X_Y_PHASE_R(n,5)=fscanf (s,'%f');
                                %acquire the in phase component
fprintf (s,'OUTP?2'); Ving_Vi_Vz_X_Y_PHASE_R(n,6)=fscanf (s,'%f');
                                %acquire the quadrature component
fprintf (s,'OUTP?4'); Ving_Vi_Vz_X_Y_PHASE_R(n,7)=fscanf (s,'%f');
                                %acquire the phase angle
fprintf (s,'OUTP?3'); Ving_Vi_Vz_X_Y_PHASE_R(n,8)=fscanf (s,'%f')

```

```

                                %acquire the module
display('END')

%Finally Measure Vz
display('prepare the electrodes for measuring Vz ') % at same frequency
pause ( 15 );
fprintf(s,'OUTP?1'); Ving_Vi_Vz_X_Y_PHASE_R(n,9)=fscanf(s,'%f');
                                %acquire the in phase component
fprintf(s,'OUTP?2'); Ving_Vi_Vz_X_Y_PHASE_R(n,10)=fscanf(s,'%f');
                                %acquire the quadrature component
fprintf(s,'OUTP?4');Ving_Vi_Vz_X_Y_PHASE_R(n,11)=fscanf (s,'%f');
                                %acquire the phase angle
fprintf(s,'OUTP?3'); Ving_Vi_Vz_X_Y_PHASE_R(n,12)=fscanf (s,'%f')
                                %acquire the module

%CYCLE: change frequency
if t<=15
    t=t+1;% change frequency condition
    else start_acquisition_index=0; % measurements done, quit
end
end

%close the connection and clear COM3
fclose(s);
delete(s);
clear s ;

%Now you can save the data matrix Ving_Vi_Vz_X_Y_PHASE_R with the line on
%the prompt:
%xlswrite('data.xls',Ving_Vi_Vz_X_Y_PHASE_R)

```

B.2. Calibration Code

```
%The code produces 16 adjacent stimulation and 16 adjacent measurements on
%the same electrodes.
% It creates the matrix R (16X1) for the module of the measurement.
% The same code it was used for the Measurement of a Resistor moved by hand
% on the electrode of stimulation and measurement (adjacent protocol).

%polarization and measurement indexes
i=0;j=1;

%initialize the connections with the Lock-in and the Vinculum (check the
%%Lock-in amplifier's Manual)
f= serial('COM4');
f.FlowControl='hardware';
fopen(f);          %start the connection with the Vinculum
f.RequestToSend='on';

s = serial('COM3');
s.Terminator= 'CR' ; %the Lock/in recognizes a command if CR is its
%terminator
s.FlowControl='hardware';
fopen(s);          %start the connection with Lock-in amplifier
s.RequestToSend='on';
fprintf(s,'REST');

    fprintf (s,'FREQ10E3');%Set the frequency at 10 KHz

%%%Measurement CYCLE
start_acquisition_index=1;
while start_acquisition_index>0

    %since i [0:15], the module16 operation is only for j
    if j>=16
        j=0;
    end

    indexes=[i j i j];
    %%set the excitation  Vg on  polarization and measurement electrodes
    fprintf (f,'%X%X%X%X#',indexes);
    %signs indexes definition: i=i-, j=i+,h=V+,k=V-
    %send to the  vinculum the sequence of pairs stimulation i,j and measurement
    %electrodes h, k.
    pause(2)% mi assicuro che il comando arrivi
```

```

%//-->> ACQUISITIONS from the Lock-in:
% Acquire the module of Vadjacent

fprintf (s,'AGAN');%We need the Autogain function in changing the turning on
%different channels.
pause (5 );%wait for a stable measurement 5Tau (=100ms*5=0.5 sec)plus wait
%that Autogain command ends
fprintf (s,'OUTP?3'); datamodulo(j)=fscanf (s, '%f')%acquire the module
display('Vadjacent Acquired')
display('change electrodes') %Useful message in the case of resistor
%measurement.You can move the resistance on the next caple of electrodes.
pause(4)%wait

%Indexes generation CYCLE
    if j<=15
        i=i+1;j=j+1;
        else start_acquisition_index=0; % 16 measurements done,quit
    end
end

%% close the connections
fclose(s); fclose(f);
%END the serial port sessions: clean up serial communications

delete(s); delete(f);
clear s ; clear f;

%Now you can save the data matrixes with the lines on the prompt:
%xlswrite('data_CALIBRATION.xls',datamodulo);
%OR
%xlswrite('data_RESISTOR.xls',datamodulo);

```

B.3. Saline Solution Measurement Code

B.3.1 Acquisition of 16 Data for the comprehension of the reliability of the Software in solving the forward problem

%Acquired data are 16 corresponding to the adjacent measurement for the
%first stimulation, according with opposite stimulation method.
%Messages are sent for change by hand the measurement electrode couples.

```
%//initialize the connection with the Lock-in for more details check the  
%%Lock-in amplifier's Manual  
s = serial('COM3');  
s.Terminator= 'CR' ; %The Lock-in recognizes a command if CR is its  
terminator  
s.FlowControl='hardware';  
fopen(s); %start the connection with Lock-in amplifier  
s.RequestToSend='on';  
fprintf(s, 'REST');  
fprintf (s, 'FREQ1E3')%set the frequency at 1KHz  
  
%%%Measurement CYCLE  
start_acquisition_index=1;  
n=1;%indexes of measurement  
while start_acquisition_index>0  
    if n==1  
  
        display('first measurement')  
        pause ( 3 ); %wait  
    end  
    if n==2  
  
        display('New measurements:Move the probes on adjacent couple of...  
...electrodes ')  
        pause ( 3 );%wait  
    end  
    if n==3  
  
        display('New measurements:Move the probes on adjacent couple of...  
...electrodes')  
        pause ( 3 );%wait  
    end  
    if n==4  
  
        display('New measurements:Move the probes on adjacent couple of...  
...electrodes')  
        pause ( 3 );%wait  
    end  
end
```

```

        if n==5

            display('New measurements:Move the probes on adjacent couple of...
...electrodes')
            pause ( 3 );%wait

        end
        if n==6

            display('New measurements:Move the probes on adjacent couple of...
...electrodes')
            pause ( 3 );%wait

        end
        if n==7

            display('New measurements:Move the probes on adjacent couple of...
...electrodes')
            pause ( 3 );%wait

        end
        if n==8

            display('New measurements:Move the probes on adjacent couple of...
...electrodes')
            pause ( 3 );%wait

        end
        if n==9

            display('New measurements:Move the probes on adjacent couple of...
...electrodes')
            pause ( 3 );%wait

        end
        if n==10

            display('New measurements:Move the probes on adjacent couple of...
...electrodes')
            pause ( 3 );%wait

        end
        if n==11

            display('New measurements:Move the probes on adjacent couple of...
...electrodes')
            pause ( 3 );%wait

        end
end

```

```

        if n==12

            display('New measurements:Move the probes on adjacent couple of...
...electrodes')
            pause ( 3 );%wait
        end
        if n==13

            display('New measurements:Move the probes on adjacent couple of...
...electrodes')
            pause ( 3 );%wait

        end
        if n==14

            display('New measurements:Move the probes on adjacent couple of...
...electrodes')
            pause ( 3 );%wait

        end
        if n==15

            display('New measurements:Move the probes on adjacent couple of...
...electrodes')
            pause ( 3 );%wait

        end
        if n==16

            display('New measurements:Move the probes on adjacent couple of...
...electrodes')
            pause ( 3 );%wait

        end

        end

        %/-->> ACQUISITION from the Lock-in:
        fprintf (s,'OUTP?1'); Vadj_X(n,1)=fscanf (s, '%f')%acquire the in phase
        component
        display('Vadjacent acquired')

    %Cycle 16 acquisitions
    if n<=15
        n=n+1;
        else start_acquisition_index=0;% 16 measurements done, quit
    end
end

%close the connection and clear COM3

```



```
fclose(s);  
delete(s);  
clear s ;
```

```
%Now you can save the data matrix Vadj_X with the line on  
%the prompt:  
%xlswrite('16data_fwdsimulation.xls',Vadj_X )
```

B.3.2 Acquisition of 256 Data for the comprehension of the reliability of the Software in recreating images

```
%The code acquire from the Lock-in the in phase component of tension,  
%according with opposite stimulation and adjacent measurement method.  
%The final matrix is a 16X16 square data set.  
  
%measurement indexes  
h=0;k=15;  
%polarization indexes  
i=0;j=8;  
  
%initialize the connections with the Lock-in and the Vinculum (check the  
%%Lock-in amplifier's Manual)  
f= serial('COM4');  
f.FlowControl='hardware';  
fopen(f); %start the connection with the Vinculum  
f.RequestToSend='on';  
  
s = serial('COM3');  
s.Terminator= 'CR' ; %the Lock/in recognizes a command if CR is its  
terminator  
s.FlowControl='hardware';  
fopen(s); %start the connection with Lock-in amplifier  
s.RequestToSend='on';  
fprintf(s, 'REST');  
  
fprintf (s, 'FREQ10E3'); %Set the frequency at 10 KHz  
  
%%%Measurement CYCLE  
misura_in_corso=1;  
while misura_in_corso>0  
    %Module16 operation for each indexes  
    if i>=16  
        i=0;  
    end  
    if j>=16  
        j=0;  
    end  
    if h>=16  
        h=0;  
    end  
    if k>=16  
        k=0;  
    end  
  
    indexes=[i j h k];  
    %%set the excitation Vg on polarization and measurement electrodes  
    fprintf (f, '%X%X%X%X#', indexes);  
    %signs indexes definition: i=i-, j=i+, h=V+, k=V-
```

```

%send to the vinculum the sequence of pairs stimulation i,j and measurement
%electrodes h, k.

    pause (2 ); %wait

    %/-->> ACQUISITIONS from the Lock-in:
    % Acquire Vadjacent
    fprintf (s,'AGAN');
    %We need the Autogain function in changing the turning on different
    %channels.

    pause (5);%wait for a stable measurement 5Tau (=100ms*5=0.5 sec)plus wait
    %that Autogain command ends
    fprintf (s,'OUTP?1'); data(i+1,h+1)=fscanf (s, '%f')
                                %acquire the in phase component

    display('Measurement ENDED')

%%%%%%%%%%%%%%%%%%%%%%%%%%%%%%%%%%%%%%%%%%%%%%%%%%%%%%%%%%%%%%%%%%%%%%%%indexes generation CYCLE%%%%%%%%%%%%%%%%%%%%%%%%%%%%%%%%%%%%%%%%%%%%%%%%%%%%%%%%%%%%%%%%%%%%%%%%
    if i>0 %condition after the first measurement cycle of 16 data.
        if h>=i
            h=h+1;k=k+1;

            elseif h<(i-1)
                h=h+1;k=k+1;

            else    i=i+1;j=j+1; h=i; k=i-1 ;

        end
    end

    if (i==0)%condition for the first measurement cycle
        if h<15
            h=h+1;k=k+1;

            else    i=i+1;j=j+1; h=i;k=i-1;

        end
    end

    if i>15
        misura_in_corso=0;
    end % 256 measurements done quit
end

```

```
%%close the connections
fclose(s); fclose(f);
%END the serial port sessions: clean up serial communications
delete(s); delete(f);
clear s ; clear f;

%Now you can save the data matrixes with the lines on the prompt:
%xlswrite('SALINE_SOLUTION.xls',data);
```

B.4. Acquisition Code

```
%The code acquires 256 voltages (Vadjacent, with all the components) with
%opposite stimulation and adjacent measurement procedures. Data can then be
%used for the image reconstruction.
%It extracts measurements ( Vopposite and Vopposite_inverse) for checking
%the crosstalks presence and VnodeA for electric current through the sample
%calculation.
%Detail: We need the Autogain function in changing the turning on different
%channels.

%measurement indexes
h=0;k=15;
%polarization indexes
i=0;j=8;

%initialize the connections with the Lock-in and the Vinculum (check the
%Lock-in amplifier's Manual)
f= serial('COM4');
f.FlowControl='hardware';
fopen(f);          %start the connection with the Vinculum
f.RequestToSend='on';

s = serial('COM3');
s.Terminator= 'CR' ;%the Lock/in recognizes a command if CR is its terminator
s.FlowControl='hardware';
fopen(s);          %start the connection with Lock-in amplifier
s.RequestToSend='on';
fprintf(s,'REST');

fprintf (s,'FREQ10E3');%Set the frequency at 10 KHz

%%%Measurement CYCLE
start_acquisition_index=1;
while start_acquisition_index>0
    %Module16 operation for each indexes
    if i>=16
        i=0;
    end
    if j>=16
        j=0;
    end
    if h>=16
        h=0;
    end
    if k>=16
        k=0;
    end

    indexes=[i j h k];
```

```

    %//set the excitation Vg on polarization and measurement electrodes
    fprintf (f,'%X%X%X%X#',indexes);
        %signs indexes definition: i=i-, j=i+,h=V+, k=V-
%send to the vinculum the sequence of pairs stimulation i,j and measurement
%electrodes h, k.
pause (2 ); %wait

%//-->> ACQUISITIONS from the Lock-in:
% Acquire Vadjacent
fprintf (s,'AGAN');%Autogain function
pause (5);%wait for a stable measurement 5Tau (=100ms*5=0.5 sec)plus wait
%that Autogain command ends
fprintf (s,'OUTP?1'); datax(i+1,h+1)=fscanf (s, '%f');
                                %acquire the in phase component
fprintf (s,'OUTP?2'); datay(i+1,h+1)=fscanf (s, '%f');
                                %acquire the quadrature component
fprintf (s,'OUTP?4'); dataphase(i+1,h+1)=fscanf (s, '%f');
                                %acquire the quadrature component
fprintf (s,'OUTP?3'); datamodule(i+1,h+1)=fscanf (s, '%f');
                                %acquire the module
display('ACQUIRED Vadjacent')

%Condition for acquiring Vopposite, VnodeA and Vopposite_inverse:
if ((i>0) && (h==(i-1))) %if both of the conditions are satisfied, then
%send to the vinculum 2 new strings
other_indexes=[i j i j];% set the opposite electrodes for measuring the
%tension
%send to the Vinculum the first new string for Vopposite
fprintf (f,'%X%X%X%X#',other_indexes);
        %signs indexes definition i=i-, j=i+, i=V+, i=V-
pause (2 ); %wait

%ACQUIRE Vopposite
fprintf (s,'AGAN');
pause (5);%wait for a stable measurement 5Tau (=100ms*5=0.5 sec)plus wait
%that Autogain command ends
fprintf (s,'OUTP?1'); Vopp_X_Y_PHASE_R(i+1,1)=fscanf (s, '%f');
                                %acquire the in phase component
fprintf (s,'OUTP?2'); Vopp_X_Y_PHASE_R(i+1,2)=fscanf (s, '%f');
                                %acquire the quadrature component
fprintf (s,'OUTP?4'); Vopp_X_Y_PHASE_R(i+1,3)=fscanf (s, '%f');
                                %acquire the quadrature component
fprintf (s,'OUTP?3'); Vopp_X_Y_PHASE_R(i+1,4)=fscanf (s, '%f');
                                %acquire the module
display('ACQUIRED Vopposite')

%Now acquire VnodeA. It's a single-ended measurement and it does not
%need sending to the Vinculum an other string.
display('TYPE single-ended A')%from the Lock-in's front panel.
pause (4); %wait
fprintf (s,'AGAN');
pause (5);%wait for a stable measurement 5Tau (=100ms*5=0.5 sec)plus wait
%that Autogain command ends
fprintf (s,'OUTP?1');

```

```

Vsingle_ended_A_X_Y_PHASE_R(i+1,1)=fscanf (s,'%f');
                                %acquire the in phase component
fprintf (s,'OUTP?2');
Vsingle_ended_A_X_Y_PHASE_R(i+1,2)=fscanf (s,'%f');
                                %acquire the quadrature component
fprintf (s,'OUTP?4');
Vsingle_ended_A_X_Y_PHASE_R(i+1,3)=fscanf (s, '%f');
                                %acquire the quadrature component
fprintf (s,'OUTP?3');
Vsingle_ended_A_X_Y_PHASE_R(i+1,4)=fscanf (s, '%f');%acquire the module
display('ACQUIRED VnodeA: type A-B')%from the Lock-in's front panel.
                                %Reset the differential mode!
pause(7)%wait

```

```

%Now acquire Vopposite_inverse
different_indexes=[i j j i];% set the opposite electrodes for measuring the
%tension in inverse direction of the excitation
%send to the Vinculum the first new string for Vopposite
fprintf (f,'%X%X%X%X#',different_indexes);
                                %signs indexes definition: i=i-% j=i+, j=V+, i=V-
pause (2 ); %wait
fprintf (s,'AGAN');
pause (5);%wait for a stable measurement 5Tau (=100ms*5=0.5 sec)plus wait
%that Autogain command ends
fprintf (s,'OUTP?1'); Vopp_inversa_X_Y_PHASE_R(i+1,1)=fscanf(s,'%f');
                                %acquire the in phase component
fprintf (s,'OUTP?2'); Vopp_inversa_X_Y_PHASE_R(i+1,2)=fscanf(s,'%f');
                                %acquire the quadrature component
fprintf (s,'OUTP?4'); Vopp_inversa_X_Y_PHASE_R(i+1,3)=fscanf(s,'%f');
                                %acquire the quadrature component
fprintf (s,'OUTP?3'); Vopp_inversa_X_Y_PHASE_R(i+1,4)=fscanf(s,'%f');
                                %acquire the module
display('ACQUIRED Vopposite_inverse')
end

```

```

if ((i==0) && (h==15)) %if both of the conditions are satisfied, then do
%the next step
other_indexes=[i j i j];%set the opposite electrodes for measuring the
%tension
%send to the Vinculum the first new string for Vopposite
fprintf (f,'%X%X%X%X#',other_indexes);
                                %signs indexes definition i=i-, j= i+, i=V+, i=V-
pause (2 ); %wait

```

```

%ACQUIRE Vopposite
fprintf (s,'AGAN');
pause (5);%wait for a stable measurement 5Tau (=100ms*5=0.5 sec)plus wait
%that Autogain command ends
fprintf (s,'OUTP?1'); Vopp_X_Y_PHASE_R(i+1,1)=fscanf (s, '%f');
                                %acquire the in phase component
fprintf (s,'OUTP?2'); Vopp_X_Y_PHASE_R(i+1,2)=fscanf (s, '%f');
                                %acquire the quadrature component
fprintf (s,'OUTP?4'); Vopp_X_Y_PHASE_R(i+1,3)=fscanf (s, '%f');

```

```

                                %acquire the quadrature component

fprintf (s,'OUTP?3'); Vopp_X_Y_PHASE_R(i+1,4)=fscanf (s, '%f');
                                %acquire the module

display('ACQUIRED Vopposite')

%Now acquire VnodeA. It's a single-ended measurment and it does not
%need sending to the Vinculum an other string.
display('TYPE  single-ended A')%from the Lock-in's front panel.
pause (4); %wait
fprintf (s,'AGAN');
pause (5);%wait for a stable measurement 5Tau (=100ms*5=0.5 sec)plus wait
%that Autogain command ends
fprintf (s,'OUTP?1');
Vsingle_ended_A_X_Y_PHASE_R(i+1,1)=fscanf(s,'%f');%acquire the in phase
%component
fprintf (s,'OUTP?2');
Vsingle_ended_A_X_Y_PHASE_R(i+1,2)=fscanf(s,'%f');%acquire the quadrature
%component
fprintf (s,'OUTP?4'); Vsingle_ended_A_X_Y_PHASE_R(i+1,3)=fscanf(s,'%f');
                                %acquire the quadrature component
fprintf (s,'OUTP?3');
Vsingle_ended_A_X_Y_PHASE_R(i+1,4)=fscanf(s,'%f');%acquire the module
display('ACQUIRED VnodeA: type A-B')%from the Lock-in's front panel.
                                %Reset the differential mode!
pause(7)%wait

%Now acquire Vopposite_inverse
different_indexes=[i j j i];
% set the opposite electrodes for measuring %the tension in inverse direction
%of the excitation
%send to the vinculum the second new string
fprintf (f,'%X%X%X%X#',different_indexes);
                                %signs indexes definition: i=i- %j=i+, j=V+, i=V-
pause (2 ); %wait
fprintf (s,'AGAN');
pause (5);%wait for a stable measurement 5Tau (=100ms*5=0.5 sec)plus wait
%that Autogain command ends
fprintf (s,'OUTP?1'); Vopp_inversa_X_Y_PHASE_R(i+1,1)=fscanf(s,'%f');
                                %acquire the in phase component
fprintf (s,'OUTP?2'); Vopp_inversa_X_Y_PHASE_R(i+1,2)=fscanf(s,'%f');
                                %acquire the quadrature component
fprintf (s,'OUTP?4'); Vopp_inversa_X_Y_PHASE_R(i+1,3)=fscanf(s,'%f');
                                %acquire the quadrature component
fprintf (s,'OUTP?3'); Vopp_inversa_X_Y_PHASE_R(i+1,4)=fscanf(s,'%f');
                                %acquire the module
display('ACQUIRED Vopposite_inverse')
end

```



```
%%%%%%%%%%%%%%%%%%%%%%%%%%%%%%%%%%%%%%%%%%%%%%%%%%%%%%%%%%%%%%%%%%%%%%%%indexes generation CYCLE%%%%%%%%%%%%%%%%%%%%%%%%%%%%%%%%%%%%%%%%%%%%%%%%%%%%%%%%%%%%%%%%%%%%%%%%
```

```

    if i>0 %condition after the first measurement cycle of 16 data.
        if h>=i
            h=h+1;k=k+1;

            elseif h<(i-1)%condition to get h to 1 hexadecimal number before i
                h=h+1;k=k+1;

            else    i=i+1;j=j+1; h=i; k=i-1 ;

        end
    end

    if (i==0)%condition for the first measurement cycle
        if h<15
            h=h+1;k=k+1;

            else    i=i+1;j=j+1; h=i;k=i-1;

        end
    end

    if i>15
        start_acquisition_index=0; % 256 measurements done quit
    end
end

```

```
%%%%%%%%%%%%%%%%%%%%%%%%%%%%%%%%%%%%%%%%%%%%%%%%%%%%%%%%%%%%%%%%%%%%%%%%Trasposition of the Vadjacent component matrixes%%%%%%%%%%%%%%%%%%%%%%%%%%%%%%%%%%%%%%%%%%%%%%%%%%%%%%%%%%%%%%%%%%%%%%%%
```

```

data_real=datax';
data_quad=datay';
data_phase=dataphase';
data_module=datamodule';

x1=data_real(:,1);y1=data_quad(:,1); p1=data_phase(:,1);m1=data_module(:,1);
x2=data_real(:,2);y2=data_quad(:,2); p2=data_phase(:,2);m2=data_module(:,2);
x3=data_real(:,3);y3=data_quad(:,3); p3=data_phase(:,3);m3=data_module(:,3);
x4=data_real(:,4);y4=data_quad(:,4); p4=data_phase(:,4);m4=data_module(:,4);
x5=data_real(:,5);y5=data_quad(:,5); p5=data_phase(:,5);m5=data_module(:,5);
x6=data_real(:,6);y6=data_quad(:,6); p6=data_phase(:,6);m6=data_module(:,6);
x7=data_real(:,7);y7=data_quad(:,7); p7=data_phase(:,7);m7=data_module(:,7);
x8=data_real(:,8);y8=data_quad(:,8); p8=data_phase(:,8);m8=data_module(:,8);
x9=data_real(:,9);y9=data_quad(:,9); p9=data_phase(:,9);m9=data_module(:,9);
x10=data_real(:,10);y10=data_quad(:,10);p10=data_phase(:,10);
m10=data_module(:,10);
x11=data_real(:,11);y11=data_quad(:,11); p11=data_phase(:,11);
m11=data_module(:,11);

```

```

x12=data_real(:,12); y12=data_quad(:,12);
p12=data_phase(:,12);m12=data_module(:,12);
x13=data_real(:,13); y13=data_quad(:,13);
p13=data_phase(:,13);m13=data_module(:,13);
x14=data_real(:,14);y14=data_quad(:,14);p14=data_phase(:,14);
m14=data_module(:,14);
x15=data_real(:,15);y15=data_quad(:,15);p15=data_phase(:,15);
m15=data_module(:,15);
x16=data_real(:,16);y16=data_quad(:,16);p16=data_phase(:,16);
m16=data_module(:,16);

%generation of 16X1 vectors of each components of Vadjacent
X= [x1; x2; x3 ;x4; x5; x6; x7; x8; x9 ;x10; x11; x12; x13; x14; x15; x16] ;
Y= [y1; y2; y3 ;y4; y5; y6; y7; y8; y9 ;y10; y11; y12; y13; y14; y15; y16] ;
PHASE=[p1; p2; p3 ;p4; p5; p6; p7; p8; p9 ;p10; p11; p12; p13; p14;p15;p16];
MODULE=[m1; m2; m3; m4; m5; m6; m7; m8; m9; m10; m11; m12; m13; m14;m15;m16];

%%close the connections
fclose(s); fclose(f);
%END the serial port sessions: clean up serial communications
delete(s); delete(f);
clear s ; clear f;

%Now you can save the data matrixes with the lines on the prompt:
%xlswrite('Vx.xls',X);xlswrite('Vy.xls',Y);xlswrite('phaseangle.xls',PHASE);
%xlswrite('module.xls',MODULE);
%xlswrite('Vopposite.xls',Vopp_X_Y_PHASE_R);
%xlswrite('Vopposite_inverse.xls', Vopp_inversa_X_Y_PHASE_R );
%xlswrite('VnodeA.xls',Vsingle_ended_A_X_Y_PHASE_R);

```

C. Electrical Impedance Tomography EIDORS Codes

C.1. Simulations

C.1.1. Forward Solving

```
%The code solves the forward problem, discretizing the medium and settling
%the conductivity value
%homogeneously, and the applied current. The solution obtains 256 simulated
%voltages.
%Then they are plotted to be compared with 16 real voltages acquired in the
%during a real experiment with saline solution 0.9% (conductivity
14.44mS/cm) and stimulation of 1.6 mA.
```

```
%Three dimensional Meshing of the tank filled with 15 ml of saline solution
%0.9%. Mesh of 8716 elements.
Nel=16; %electrodes
fmdl= ng_mk_cyl_models([0.264,4.12],[Nel,0],[0.0525,0]);
%NETGEN defines fwd_object this FEM
%we need to define each parameter for forward solution calculation
fmdl.solve='aa_fwd_solve';
fmdl.system_mat='aa_calc_system_mat';
fmdl.jacobian= 'aa_calc_jacobian';
img= eidors_obj('image','saline solution');
img.fwd_model=fmdl;
img.elem_data = fmdl.elems(:,1);
%we need to create the matrix of conductivity element (each element of the
%mesh has 1 value of conductivity)
figure;
show_fem(fmdl);
```

```
%for an accurate reproduction of the experiment we can set the impedance of
% electrodes
for i=1:Nel
    img.fwd_model.electrode(i).z_contact=0.03;%30mOhm
end
```

```
% Calculate a stimulation pattern: set the applied electric current.
%Define also the method: opposite stimulation and adjacent measurement.
%In total the code obtain 256 measurement of simulated tensions.
stim = mk_stim_patterns(16,1,'{op}','{ad}','{meas_current}',0.0016);%mA
% Solve all voltage patterns
img.fwd_model.stimulation = stim;
img.fwd_solve.get_all_meas = 1;
```

```
%SET the conductivity, creating an Homogeneous model
img.elem_data(:) = 14.4;%Homogeneous conductivity [mS/cm] of saline solution
%solve for voltage distribution V
vh = fwd_solve(img);
```

```

figure;
plot (vh.meas);%plot 256 simulated tensions
figure;
plot(vh.meas(1:16));axis([1 16 -0.02 0.02 ]);
                                %plot only the first 16 simulated tensions
vh_real=xlsread('samplehomog.xls');
                                %Load real acquisition.They are only 16!!
figure;
plot (vh_real);axis([1 16 -0.02 0.02 ]);%plot real tension

```

C.1.2. Conductive, Insulating Objects

```
%the code solves both the forward and the inverse problem. The forward
%problem is solved twice for obtaining the homogeneous voltages of the
%background and for obtaining the inhomogeneous voltages of the background
%and the inclusion. These two data set are plotted and used for solving the
%inverse problem.
%for trying different insulation object one need to change the
%img.elem_data field when indicated.

I = 0.012008;%current of 12 microampere
Nel=16;
stim=mk_stim_patterns(Nel,1,'{op}','{ad}','meas_current',I);
    %opposite excitation and adjacent measurements of 256 data
%Create a circular object in which set a different conductivity
extra={'ball','solid ball = cylinder(0.2,0.2,0;0.2,0.2,1;0.2) and
orthobrick(-1,-1,0;1,1,0.05);'};
fmdl= ng_mk_cyl_models(0,[16],[0.2,0,0.05],extra);%three dimensional mesh.
    %create the forward model with the inclusion
img= eidors_obj('image','ball'); img.fwd_model= fmdl;
ctr = interp_mesh(fmdl); ctr=(ctr(:,1)-0.2).^2 + (ctr(:,2)-0.2).^2;
img.elem_data = 1 + 0.1*(ctr < 0.2^2);
figure;
show_fem(img,1);axis off;axis equal
img.fwd_model.stimulation = stim;
% Get all voltages so we can plot it
img.fwd_solve.get_all_meas = 1;

% Homogeneous model
img.elem_data(:) = 7.7;
%set the conductivity of the background(the same of the saline solution 0.4%)
vsimh = fwd_solve(img);%simulated homogeneous voltages for the background

% Set very insulating or very high inhomogeneous conductivity
img.elem_data = 7.7 +10*(ctr < 0.2^2);%insulating inclusion case
    %for high conductive inclusion use 7.7 - 7.5*(ctr < 0.2^2)
vsiminh = fwd_solve(img);
    %simulated inhomogenous voltages with background plus inclusion
figure;
plot([vsimh.meas, vsiminh.meas]); %plot them together.
    %The first is green and the second is blue.

% basic inverse model : aa_inv_solve
imdl = mk_common_model('c2c2',16); % two dimensional mesh
imdl.fwd_model = img.fwd_model;
imdl.fwd_model.nodes= imdl.fwd_model.nodes*4.12; % change scale here
imdl.hyperparameter.value = .0003;% Change the hyperparameter value
imgr = inv_solve(imdl, vsimh, vsiminh);
figure;show_fem(imgr,[1 1]);axis equal
```

C.1.3. 3D Reconstruction of layers

```
%EIDORS code for studying the reconstructed images with planar electrode
%array configuration.
%It solves the forward problem twice for obtaining homogeneous and
%inhomogeneous voltages from the same 3D Mesh loaded firstly, without any
%inclusions, and secondly, with a sphere as a high conductivity inclusion.
```

```
Nel= 16; %Number of electrodes
Zc = .03; % Contact impedance 30mOhm
I = 0.012008; %applied current in mA (=12 microA)
%Create homogenous 3D Mesh of 8044 elements
shape_str = ['solid top      = plane(0,0,0;0,0,1);\n' ...
             'solid mainobj= top and orthobrick(-0.35,-0.35,-
0.035;0.35,0.35,0) -maxh=0.5;\n'];
%SET ELECTRODES POSITION
elec_pos = [- 0.15,- 0.15 , 0, 0, 0, 1;%ELECT_1
            - 0.15, -0.05, 0, 0, 0, 1;%ELECT_2
            - 0.15, 0.05, 0, 0, 0, 1;%ELECT_3
            -0.15, 0.15, 0, 0, 0, 1;%ELECT_4
            -0.05, - 0.15, 0, 0, 0, 1;%ELECT_5
            -0.05, -0.05, 0, 0, 0, 1;%ELECT_6
            -0.05, 0.05, 0, 0, 0, 1;%ELECT_7
            -0.05, 0.15, 0, 0, 0, 1;%ELECT_8
            0.05, 0.15, 0, 0, 0, 1;%ELECT_9
            0.05, 0.05, 0, 0, 0, 1;%ELECT_10
            0.05, -0.05, 0, 0, 0, 1;%ELECT_11
            0.05, - 0.15, 0, 0, 0, 1;%ELECT_12
            0.15, 0.15, 0, 0, 0, 1;%ELECT_13
            0.15, 0.05, 0, 0, 0, 1;%ELECT_14
            0.15, -0.05, 0, 0, 0, 1;%ELECT_15
            0.15, - 0.15, 0, 0, 0, 1;%ELECT_16];
elec_shape=[0.01];%electrode diameter:100 micron
elec_obj = 'top';
fmdl = ng_mk_gen_models(shape_str, elec_pos, elec_shape, elec_obj);
%Set stimulation and measurement methods
fmdl.stimulation= mk_stim_patterns(Nel,1,'{op}','{ad}','{meas_current}',I);
img = mk_image( fmdl, 1);%Set homogeneous conductivity
vh= fwd_solve(img);%solve inverse problem for homogeneous voltages

%3D Mesh with more conductive central sphere (radius 0.6 mm)
shape_str = ['solid top      = plane(0,0,0;0,0,1);\n' ...
             'solid ball     = sphere(0,0,-0.06;0.06); tlo ball;\n' ...
             'solid mainobj= top and orthobrick(-0.35,-0.35,-
0.12;0.35,0.35,0)and not ball -maxh=0.5;\n'];
[fmdl,mat_idx] = ng_mk_gen_models(shape_str, elec_pos, elec_shape, elec_obj);
fmdl.stimulation= mk_stim_patterns(Nel,1,'{op}','{ad}','{meas_current}',I);
imgobj = mk_image( fmdl, 1);
imgobj.elem_data(mat_idx{1}) = 1.5;
figure;
show_fem( imgobj,1 ); axis on;axis equal %Show 3D mesh with the sphere
```

```

img.fwd_solve.get_all_meas = 1;
vi= fwd_solve(imgobj);%solve inverse problem for homogeneous voltages
figure;
plot( vi.meas);
axis tight

% Create Inverse Model
inv3d= eidors_obj('inv_model', 'EIT inverse');
inv3d.reconst_type= 'difference';
inv3d.jacobian_bkgnd.value = 1;
inv3d.fwd_model= fmdl;%load directly the 3D forward model

% Reconstruction Model $Id: basic_3d_05.m 2128 2010-04-01 21:25:35Z aadler $
J = calc_jacobian( calc_jacobian_bkgnd( inv3d) );
iRtR = inv(noser_image_prior( inv3d ));
hp = 0.17;% hyperparameter value
iRN = hp^2 * speye(size(J,1));
RM = iRtR*J'/(J*iRtR*J' + iRN);
inv3d.solve = 'solve_use_matrix';
inv3d.solve_use_matrix.RM = RM;
imgr = inv_solve(inv3d, vh, vi);
imgr.calc_colours.cb_shrink_move = [0.5,0.8,0.05];
imgr.calc_colours.ref_level = 0;
figure;
show_fem(imgr,1); axis on; axis equal ;

figure;levels= [inf,inf,-0.04;];%cross-section parallel to the electrode
plane at a 400 micron depth
show_slices (imgr,levels); axis off;axis equal;

figure;levels= [inf,inf,-0.06];%cross-section at a 600 micron depth
show_slices (imgr,levels); axis off;axis equal;

figure;levels= [inf,inf,-0.1;];%cross-section at a 1 mm depth
show_slices (imgr,levels); axis off;axis equal;

figure;levels= [inf,inf,-0.12;];%cross-section at a 1.2 mm depth
show_slices (imgr,levels); axis off;axis equal;

figure;levels= [0,inf,inf];%vertical slice passing through the center of the
%phantom
show_slices (imgr,levels); axis off;axis equal;

```

C.2. Reconstructions

C.2.1. Saline Solution Reconstruction

```
% The code solves the inverse problem of the saline solution.
% In the tutorial has given the method called "Cheap static solver" for
% estimating the actual conductivity map.
% In theory the solver is static because it uses data coming from
% the saline solution. In order to obtain a differential solver i could make
% use of the forward solution and the simulated data as second dataset.

%load real data acquired from the experiment of saline solution
vh=xlsread('samplehomogX.xlsx');

%I improved the quality of the images by ensuring that all channels have a
%MEAN OF VOLTAGES OF ZERO before beginning.
media=mean(vh);

for i=1:256
    vh(i)= vh(i)-media;
end

figure;plot(vh);

%3D Meshing
Nel=16;
I=120.08;
fmdl= ng_mk_cyl_models([0.264,4.12],[Nel,0],[0.0525,0]);
img1= eidors_obj('image','FWD SOLVE');
img1.fwd_model=fmdl;
img1.elem_data = fmdl.elems(:,1);
figure;
show_fem(fmdl,[1,1]);

%Set the contact impedance of electrodes in circular array configuration
for i=1:Nel
    img1.fwd_model.electrode(i).z_contact=0.03;%30mOhm
end

% Calculate a stimulation pattern
stim = mk_stim_patterns(16,1,'{op}','{ad}', {'meas_current'},0.0012008);
    %electric current expressed in mA,(12.008 microampere)
% Solve all voltage patterns
img1.fwd_model.stimulation = stim;
img1.fwd_solve.get_all_meas = 1;

% Homogeneous model
```



```

img1.elem_data(:) = 14.4;
                %Homogeneous conductivity [mS/cm] of saline solution
vs = fwd_solve(img1); % solve for voltage distribution V
vs=vs.meas;
figure;plot(vs);

%%%%%%%%%%%%%%%%%%%%%%%%%%%%%%%%%%%%%%%%%%%%%%%%%%%%%%%%%%%%%%%%%%%%%%%%
%In order to estimate the actual conductivity values, we need to scale for
%the applied voltage, tank size and background conductivity
params= mk_common_model('e2c2',16); %2D mesh of 1600 elements
params.fwd_model = rmfield(params.fwd_model,'meas_select');
params.fwd_model.stimulation =
mk_stim_patterns(Nel,1,'{op}','{ad}','{meas_current}',I);
params.fwd_model.nodes= params.fwd_model.nodes*4.12; % 8.24 cm diameter

% Estimate the background conductivity
pf = polyfit(vh,vs,1);
params.hyperparameter.value =1;
img= inv_solve (params,vs,vh); %SOLVE INVERSE PROBLEM
img.elem_data = pf(1) + img.elem_data*2.1;
figure;
img.calc_colours.cb_shrink_move = [0.5,0.8,0.05]; % colorbar option
img.calc_colours.ref_level = 0; % colorbar option
show_fem(img,[0,1]);
axis equal;axis on

```

C.2.2. 2D Protocol: Reconstruction of Various Objects

%This is the first processing file and it wants to create images of
%contrast. The file has been used for calculating the conductivity map of
%different object as difference with the background. Simply setting the
%right hyperparameter and loading datasets of the experiments, one can
%reconstruct the images.

```
%%%%%%%%%%%%%%%%%%%%%%%%%%%%%%%%%%%%%%%%%%%%%%%%%%%%%%%%%%%%%%%%%%%%%%%%STEP1%%%%%%%%%%%%%%%%%%%%%%%%%%%%%%%%%%%%%%%%%%%%%%%%%%%%%%%%%%%%%%%%%%%%%%%%
%CREATE 16ELECTRODE 3D MODEL
%Build a good FEM of the phantom it is important to correctly model
%the size of the electrodes and their position to get absolute imaging to
work.

Nel= 16; %Number of electrodes
Zc = .03; % Contact impedance 30 m?
I = 0.012008; %applied current (12 microA) expressed in mA

params= ng_mk_cyl_models([0.541,4.12],[Nel,0],[0.0525,0]);
%three dimensional Mesh of the tank corresponding to 30 ml of saline
%solution
%Set excitation and measurement methods
params.stimulation= mk_stim_patterns(Nel,1,'{op}','{ad}','{meas_current}',I);

%Set the contact impedance to each electrode

for i=1:Nel
    params.electrode(i).z_contact= Zc;
end

%Set parameters for the foward problem field
params.solve='aa_fwd_solve';
params.system_mat='aa_calc_system_mat';
params.jacobian= 'aa_calc_jacobian';
mdl_3d=eidors_obj('fwd_model',params);
%bundle everything in a structural array called fwd_model
figure;
show_fem (mdl_3d);
axis equal

%%%%%%%%%%%%%%%%%%%%%%%%%%%%%%%%%%%%%%%%%%%%%%%%%%%%%%%%%%%%%%%%%%%%%%%%STEP2%%%%%%%%%%%%%%%%%%%%%%%%%%%%%%%%%%%%%%%%%%%%%%%%%%%%%%%%%%%%%%%%%%%%%%%%

%load real data from excel files
vi=xlsread('sampleihnomogX.xlsx');%inhomogeneity, this is the EIT scan i'm
interested in
vh=xlsread('samplehomogX.xlsx');%background, this is the scan i'm comparing
to,in type 'difference'

%improve the equality of the images by ensuring that all channels have a
%MEAN OF VOLTAGES OF ZERO before beginning.

media_data=mean(vi);
```

```

for i=1:256
    vi(i)=vi(i)-media_data ;
end

media_data1=mean(vh);

for i=1:256
    vh(i)=vh(i)-media_data1 ;
end

%plot them
figure;
plot([vh, vi]);

%%%%%%%%%%%%%%%%%%%%%%%%%%%%%%%%%%%%%%%%%%%%%%%%%%%%%%%%%%%%%%%%%%%%%%%%STEP3: actual background and inverse problem solution%%%%%%%%%%%%%%%%%%%%%%%%%%%%%%%%%%%%%%%%%%%%%%%%%%%%%%%%%%%%%%%%%%%%%%%%

% Create a simple inverse model
imdl = mk_common_model('e2c2',16);%1600 elements
imdl.fwd_model = rmfield(imdl.fwd_model,'meas_select');
imdl.fwd_model.stimulation =
mk_stim_patterns(Nel,1,'{op}','{ad}','{meas_current}',I);

%Estimating actual conductivities OF SALINE SOLUTION
%In order to estimate the actual conductivity values, we need to scale for
%the applied voltage, tank size and background conductivity
imdl.fwd_model.nodes= imdl.fwd_model.nodes*4.12; % 8.24 cm diameter
imdl.hyperparameter.value =0.005;%change hyperparameter for different objects

%solve inverse problem
img = inv_solve(imdl, vh, vi);%andyadler_inv_solve
img.calc_colours.cb_shrink_move = [0.5,0.8,0.05];%colorbar option
img.calc_colours.ref_level = 0;%colorbar option
figure;
show_fem(img,[1,1]); axis on; axis equal %image

```

C.2.3. 3D Protocol: Reconstruction of a Tissue Section

```
%The code used data coming from a tissue section for 3D Reconstructions of
%anisotropic medium.
% It processes in phase and quadrature component, for obtaining resistive
% and capacitive images.
%It visualizes different cross-section of the tissue in various depth

%%%%%%%%%%%%%%%%%%%%%%%%%%%%%%%%%%%%%%%%%%%%%%%%%%%%%%%%%%%%%%%%%%%%%%%%STEP1%%%%%%%%%%%%%%%%%%%%%%%%%%%%%%%%%%%%%%%%%%%%%%%%%%%%%%%%%%%%%%%%%%%%%%%%

%CREATE 16ELECTRODE 3D MODEL of the tissue section (height 1.6 cm, radius
4.12 cm)
Nel= 16; %Number of electrodes
Zc = .03; % Contact impedance 30mOhm
I = 0.021881754; %applied current mA (22 microA)
params= ng_mk_cyl_models([1.6,4.12],[Nel,0],[0.0525,0]);
%Set stimulation and measurements protocol
params.stimulation= mk_stim_patterns(Nel,1,'{op}','{ad}','meas_current',I);
%Set contact impedance for each electrodes
for i=1:Nel
    params.electrode(i).z_contact= Zc;
end
%Define the forward_solver parameters
params.solve='aa_fwd_solve';
params.system_mat='aa_calc_system_mat';
params.jacobian= 'aa_calc_jacobian';
mdl_3d=eidors_obj('fwd_model',params);
%bundle everything in a structural array called fwd_model
figure;
show_fem (mdl_3d);
axis equal

%%%%%%%%%%%%%%%%%%%%%%%%%%%%%%%%%%%%%%%%%%%%%%%%%%%%%%%%%%%%%%%%%%%%%%%%STEP2%%%%%%%%%%%%%%%%%%%%%%%%%%%%%%%%%%%%%%%%%%%%%%%%%%%%%%%%%%%%%%%%%%%%%%%%
%load real from experiment 1 and 2 (both the components X and Y of the
voltages)
vi=xlsread('steak_1_X.xlsx');% this is the EIT scan i'm interested in
vh=xlsread('zero.xlsx');% homogeneous zero matrix,this is the background i'm
%comparing to,in type 'difference'

%improve the equality of the images by ensuring that all channels have a
%MEAN OF VOLTAGES OF ZERO before beginning.
media_data=mean(vi);

for i=1:256
    vi(i)=vi(i)-media_data;
end

%plot acquired data set
figure;
plot( vi);
```

```

%%%%%%%%%%%%%%%%%%%%%%%%%%%%%%%%%%%%%%%%%%%%%%%%%%%%%%%%%%%%%%%%%%%%%%%%STEP3:  solve inverse problem%%%%%%%%%%%%%%%%%%%%%%%%%%%%%%%%%%%%%%%%%%%%%%%%%%%%%%%%%%%%%%%%%%%%%%%%

% Create Inverse Model
inv3d= eidors_obj('inv_model', 'EIT inverse');
inv3d.reconst_type= 'difference';
inv3d.jacobian_bkgnd.value = 1;
inv3d.fwd_model= params;% Associate the 3D forward field

% Reconstruction Model (a_adler folder in EIDORS package)
J = calc_jacobian( calc_jacobian_bkgnd( inv3d) );
iRtR = inv(noser_image_prior( inv3d ));
hp = 0.17;%change Hyperparameter here for different data sets
iRN = hp^2 * speye(size(J,1));
RM = iRtR*J'/(J*iRtR*J' + iRN);
inv3d.solve = 'solve_use_matrix';
inv3d.solve_use_matrix.RM = RM;
imgr = inv_solve(inv3d, vh, vi);
media= mean(imgr.elem_data); % calculate the average in the map
imgr.elem_data = imgr.elem_data - media; %data-average Reconstruction
imgr.calc_colours.cb_shrink_move = [0.5,0.8,0.05];
imgr.calc_colours.ref_level = 0;
figure;
show_fem(imgr,1); axis on; axis equal ;%Average Reconstruction

figure;levels= [inf,inf,0.2;];%Cross-section 0.2 cm deep, parallel to the
%electrodes plane
show_slices (imgr,levels); axis off;axis equal;

figure;levels= [inf,inf,0.4;];%Cross-section 0.4 cm deep
show_slices (imgr,levels); axis off;axis equal;

figure;levels= [inf,inf,0.6;];%Cross-section 0.6 cm deep
show_slices (imgr,levels); axis off;axis equal;

figure;levels= [inf,inf,0.8;];%Cross-section 0.8 cm deep
show_slices (imgr,levels); axis off;axis equal;

figure;levels= [inf,inf,1.2;];%Cross-section 1.2 cm deep
show_slices (imgr,levels); axis off;axis equal;

figure;levels= [inf,inf,1.4;];%Cross-section 1.4 cm deep
show_slices (imgr,levels); axis off;axis equal;

figure;levels= [inf,inf,1.5;];%Cross-section 1.5 cm deep
show_slices (imgr,levels); axis off;axis equal;

```

C.2.4 3D Protocol: Reconstruction of the Skin

```
%The code does an imaging of the skin. Data were acquired from fingers of
%two people.

Nel= 16; %Number of electrodes
Zc = .03; % Contact impedance 30mOhm
I = 0.014598857; %applied current expressed in mA (14 microA)
%3D mesh: parallelepiped 1.2 mm deep
shape_str = ['solid top      = plane(0,0,0;0,0,1);\n' ...
            'solid mainobj= top and orthobrick(-0.35,-0.35,-
0.12;0.35,0.35,0) -maxh=0.5;\n'];
%Define the electrodes position.Grid of 16 electrodes 1mm distant to each
%other.
elec_pos = [- 0.15,- 0.15 , 0, 0, 0, 1;%ELECT_1
            - 0.15, -0.05, 0, 0, 0, 1;%ELECT_2
            - 0.15, 0.05, 0, 0, 0, 1;%ELECT_3
            -0.15, 0.15, 0, 0, 0, 1;%ELECT_4
            -0.05, - 0.15, 0, 0, 0, 1;%ELECT_5
            -0.05, -0.05, 0, 0, 0, 1;%ELECT_6
            -0.05, 0.05, 0, 0, 0, 1;%ELECT_7
            -0.05, 0.15, 0, 0, 0, 1;%ELECT_8
            0.05, 0.15, 0, 0, 0, 1;%ELECT_9
            0.05, 0.05, 0, 0, 0, 1;%ELECT_10
            0.05, -0.05, 0, 0, 0, 1;%ELECT_11
            0.05, - 0.15, 0, 0, 0, 1;%ELECT_12
            0.15, 0.15, 0, 0, 0, 1;%ELECT_13
            0.15, 0.05, 0, 0, 0, 1;%ELECT_14
            0.15, -0.05, 0, 0, 0, 1;%ELECT_15
            0.15, - 0.15, 0, 0, 0, 1;];%ELECT_16
elec_shape=[0.023];%diameter 230 micron
elec_obj = 'top';
fmdl = ng_mk_gen_models(shape_str, elec_pos, elec_shape, elec_obj);
fmdl.stimulation= mk_stim_patterns(Nel,1,'{op}','{ad}','{meas_current}',I);
show_fem(fmdl);axis on ;axis equal;

%load real data and the zeros matrix
vi=xlsread('finger_X.xlsx');%this is the EIT scan i'm interested in.
%Only in phase component of boundary voltages were acquired.
vh=xlsread('zero.xlsx');% this is the scan i'm comparing to ,in type
'difference'.

%improve the equality of the images by ensuring that all channels have a
%MEAN OF VOLTAGES OF ZERO.
media_data=mean(vi);

for i=1:256
    vi(i)=vi(i)-media_data ;
end
%plot acquired data
figure;
plot(vi);
```

```

% Create Inverse Model
inv3d= eidors_obj('inv_model', 'EIT inverse');
inv3d.reconst_type= 'difference';
inv3d.jacobian_bkgnd.value = 1;
inv3d.fwd_model= fmdl;

% Reconstruction Model (a_adler_solver in the EIDORS package)
J = calc_jacobian( calc_jacobian_bkgnd( inv3d) );
iRtR = inv(noser_image_prior( inv3d ));
hp = 13;
iRN = hp^2 * speye(size(J,1));
RM = iRtR*J'/(J*iRtR*J' + iRN);
inv3d.solve = 'solve_use_matrix';
inv3d.solve_use_matrix.RM = RM;
imgr = inv_solve(inv3d, vh, vi);%solve the inverse problem
media= mean(imgr.elem_data); % calculate the average of the conductivities
imgr.elem_data = imgr.elem_data - media;%conductivity obtained - average
imgr.calc_colours.cb_shrink_move = [0.5,0.8,0.05];
imgr.calc_colours.ref_level = 0;
figure;
show_fem(imgr,1); axis on; axis equal;%average conductivity map
figure;
plot (imgr.elem_data);

figure;levels= [inf,inf,-0.00000001;];%show the top slice
show_slices (imgr,levels); axis off;axis equal;

figure;levels= [inf,inf,-0.01;];%cross-section at a 100micron depth
show_slices (imgr,levels); axis off;axis equal;

figure;levels= [inf,inf,-0.02;];%cross-section at a 200micron depth
show_slices (imgr,levels); axis off;axis equal;

figure;levels= [inf,inf,-0.03;];%cross-section at a 300micron depth
show_slices (imgr,levels); axis off;axis equal;

figure;levels= [inf,inf,-0.04;];%cross-section at a 400micron depth
show_slices (imgr,levels); axis off;axis equal;

figure;levels= [inf,inf,-0.05;];%cross-section at a 500micron depth
show_slices (imgr,levels); axis off;axis equal;

figure;levels= [inf,inf,-0.06;];%cross-section at a 600micron depth
%imgr.calc_colours.npoints= 128;
show_slices (imgr,levels); axis off;axis equal;

figure;levels= [inf,inf,-0.07;];%cross-section at a 700micron depth
%imgr.calc_colours.npoints= 128;
show_slices (imgr,levels); axis off;axis equal;

figure;levels= [inf,inf,-0.08;];%cross-section at a 800micron depth
show_slices (imgr,levels); axis off;axis equal;

figure;levels= [inf,inf,-0.09;];%cross-section at a 900micron depth
%imgr.calc_colours.npoints= 128;

```

```
show_slices (imgr,levels); axis off;axis equal;
```

```
figure;levels= [inf,inf,-0.1]; %cross-section at a 1mm depth  
show_slices (imgr,levels); axis off;axis equal;
```

```
figure;levels= [inf,inf,-0.11;]; %cross-section at a 1.1mm depth  
show_slices (imgr,levels); axis off;axis equal;
```

```
figure;levels= [inf,inf,-0.12;]; %cross-section at a 1.2mm depth  
show_slices (imgr,levels); axis off;axis equal;
```

```
figure;levels= [0,inf,inf];%vertical slice 1.2 mm deep  
show_slices (imgr,levels); axis off;axis equal;
```